

2019

# Superparamagnetic iron oxide nanoparticles for early detection of calcific aortic valve disease

---

<https://hdl.handle.net/2144/36123>

*"Downloaded from OpenBU. Boston University's institutional repository."*

BOSTON UNIVERSITY  
COLLEGE OF ENGINEERING

Dissertation

**SUPERPARAMAGNETIC IRON OXIDE NANOPARTICLES FOR EARLY  
DETECTION OF CALCIFIC AORTIC VALVE DISEASE**

by

**CARI LYNN MEISEL**

B.S.E., University of Pennsylvania, 2011  
M.S.E., Boston University, 2016

Submitted in partial fulfillment of the  
requirements for the degree of  
Doctor of Philosophy

2019



Approved by

First Reader

---

Joyce Y. Wong, Ph.D.  
Professor of Biomedical Engineering  
Professor of Materials Science and Engineering

Second Reader

---

Allison Dennis, Ph.D.  
Assistant Professor of Biomedical Engineering  
Assistant Professor of Materials Science and Engineering

Third Reader

---

Tyrone M. Porter, Ph.D.  
Associate Professor of Mechanical Engineering  
Associate Professor of Materials Science and Engineering  
Associate Professor of Biomedical Engineering

Fourth Reader

---

Dimitrios Mitsouras, Ph.D.  
Assistant Professor of Radiology  
Brigham and Women's Hospital  
Harvard Medical School

Fifth Reader

---

Frederick Schoen, M.D., Ph.D.  
Professor of Pathology and Health Sciences and Technology  
Brigham and Women's Hospital  
Harvard Medical School

## **Acknowledgements**

This work has been supported by a Biomolecular Pharmacology Training grant from the NIH/NIGMS (5T32HL007969-13), a training grant from the NIH in Inflammatory Disorders (5T32AI089673-05), and a training grant from the NIH in Cardiovascular Biology (5T32GM008541-17). This work was performed in part at the Center for Nanoscale Systems (CNS), a member of the National Nanotechnology Coordinated Infrastructure Network (NNCI), which is supported by the National Science Foundation under NSF award no. 1541959. CNS is part of Harvard University.

I would like to acknowledge contributions to this research from several lab members, mentors, collaborators, and undergraduates throughout the years.

So many undergraduates have done work with me and/or on various SPION-related projects since I started in the lab: Shivem Shah, Olivia Hale, Jordan Nustad, Nikita Patil, and Polly Bainbridge. Thank you so much for your time and hard work! And thank you to the Undergraduate Research Opportunities Program (UROP) at Boston University for their support.

To Joyce: thank you for being my advisor for the last 5 years. I have so much appreciated your insight, encouragement, and mentorship. Thank you for looking over my results and helping me make sense of them, for always knowing the right person to ask when I have a random question, and for asking me the challenging questions necessary to push me in the right direction. None of this would have

been possible without your help and guidance.

To my committee: thank you so much for all of your input and insight over the years. It has been an absolute pleasure to work with all of you, and help and feedback on my work have been invaluable.

To Jo Ann: thank you for being our Lab Mom. Thanks for sitting next to me, sharing recipes, and for all of your advice and help over the years. Thank you for proofreading everything I've written, and for your insightful feedback on every presentation I've given. I could not have done this without your help.

To all the folks who have been in the Wong lab while I've been around: my time here would not have been nearly as fun without all of you. Thanks for bringing food to lab meetings, going on long lunch breaks, and not judging me when I've taken naps at/under my desk. Thank you also for letting me bounce countless ideas off of you and show you graphs and figures and ask you "Does that make sense?" approximately one million times.

And to my family and friends: thank you for keeping me (mostly) sane while I've been doing this thing. Thanks for letting me talk to or at you about my research *ad nauseum*, for letting me practice presentations, for asking me to explain how MRIs work, and for your unshakeable support over the last five and a half years.

**SUPERPARAMAGNETIC IRON OXIDE NANOPARTICLES FOR EARLY  
DETECTION OF CALCIFIC AORTIC VALVE DISEASE**

**CARI LYNN MEISEL**

Boston University College of Engineering, 2019

Major Professor: Joyce Y. Wong, Ph.D., Professor of Biomedical Engineering,  
Professor of Materials Science and Engineering

**ABSTRACT**

Calcific Aortic Valve Disease (CAVD) is the most common acquired valvular disorder in developed countries, and is estimated to affect more than 5 million Americans. In its severe form, the disease results in hemodynamically significant aortic stenosis, which causes a variety of negative physiological impacts to patients. All told, the physiological consequences of the disease mean that the heart must work harder to pump blood throughout the body, causing the heart muscle to weaken and putting patients at a significantly greater risk of cardiovascular event. However, no clinical imaging method currently available has the ability to reliably detect early CAVD, necessarily delaying diagnosis until patients are symptomatic and the disease has progressed to its late stages. Despite the extensive cost, recovery time, and heightened risk of post-surgical complications to patients, surgical approaches are often the only option for patients with aortic stenosis due to late diagnosis of the condition. The lack of diagnostic imaging techniques capable of detecting and monitoring early-stage disease is a major unmet need in the development of new treatments of CAVD.

To address this problem, we have developed a novel contrast agent for MRI to aid in earlier detection of CAVD by using chemically modified and targeted superparamagnetic iron oxide nanoparticles (SPIONs) targeted to hydroxyapatite (HA). We have characterized the *in vitro* physiochemical and binding properties of these SPIONs as well as the selectivity of their targeted binding. We have also done work to optimize the binding and MRI contrast properties of the SPIONs. Finally, we have assessed the medically-relevant properties of the SPIONs, including their potential for toxicity and systemic effects and their binding to excised human aortic valve samples.

Our results show that these HA-targeted SPIONs can be successfully fabricated via a fairly simple reaction scheme, and that they bind selectively to HA even in the presence of serum proteins. We have also determined that the reaction scheme for the addition of the poly(ethylene glycol) (PEG) is of particular importance in optimizing the MRI contrast properties of the SPIONs. Having a hydrophilic group linking the PEG to the SPIONs yields particles with the highest contrast. Additional studies indicated that these SPIONs do not have cytotoxic properties, and that they are not expected to interfere systemically with bone homeostasis, as they neither inhibit nor encourage HA nucleation and formation. We have confirmed that these particles are able to cross an endothelial barrier, and to bind to HA subsequently. Finally, we have demonstrated targeted binding of SPIONs to sites of calcification in excised human aortic valve tissue. All together,

these studies indicate that these HA-targeted SPIONs are suitable for further development as an MRI contrast agent for the early detection of CAVD.

## Table of Contents

Abstract .....	vi
List of Tables .....	xi
List of Figures .....	xii
List of Abbreviations .....	xv
Chapter 1: Introduction and Specific Aims .....	1
1.1 Motivation: Calcific Aortic Valve Disease and Aortic Stenosis .....	1
1.2 Current Clinical Practices in Aortic Stenosis .....	3
1.3 Characteristics of Early Stage CAVD .....	6
1.4 Medical Imaging and Contrast Agents .....	8
1.5 Research Objective Statement .....	10
1.6 Specific Aims .....	12
Chapter 2: Fabrication and <i>In Vitro</i> Characterization of SPIONs .....	14
2.1 Introduction .....	14
2.2 Methods and Materials .....	18
2.3 Results .....	27
2.4 Discussion .....	42
Chapter 3: Optimization of SPION Binding Properties and MR Contrast .....	48
3.1 Introduction .....	48
3.2 Methods and Materials .....	51
3.3 Results .....	60
3.4 Discussion .....	74

Chapter 4: Characterization of the Medical Properties of Targeted SPIONs .....	84
4.1 Introduction .....	84
4.2 Methods and Materials .....	91
4.3 Results .....	100
4.4 Discussion .....	117
Chapter 5: Conclusions and Further Studies .....	125
Bibliography .....	134
Curriculum Vitae .....	158

## List of Tables

Table 1.1: Summary of diagnosed aortic stenosis severity based on measured patient parameters .....	4
Table 2.1: DLS and zeta potential measurements of SPIONs at each step of fabrication .....	28
Table 2.2: Summary of peptide properties of HABP and OPN peptides .....	29
Table 3.1: Summary of DLS, zeta potential, and TGA data for all PEGylated SPIONs .....	65

## List of Figures

Figure 1.1: Diagram of the aortic valve in the heart, both diseased and non-diseased .....	1
Figure 1.2: Characteristics of early-stage CAVD .....	7
Figure 1.3: Visualization of T1 and T2 contrast in MRI .....	9
Figure 1.4: Schematic of functionalizing SPIONs for targeted binding to hydroxyapatite .....	11
Figure 2.1: Representative schematic of fabrication and functionalization of HA-targeted SPIONs .....	15
Figure 2.2: TEM image of SPION cores .....	27
Figure 2.3: Experiments assessing targeted binding of HA-SPIONs in sodium phosphate buffer solution .....	30
Figure 2.4: Impact of pH on SPION binding to HA .....	33
Figure 2.5: Fold change of nanoparticle size over time in 50% serum .....	34
Figure 2.6: Assessment of SPION effective diameter in 50% serum over a range of pH values .....	35
Figure 2.7: Measurement of the protein corona of SPIONs after incubation with 50% serum and several wash steps .....	37
Figure 2.8: SDS-PAGE gel images of SPION protein coronas after incubation with 50% serum and washing .....	39
Figure 2.9: Assessment of targeted binding specificity in 50% serum .....	41

Figure 3.1: Assessment of the impact of functionalizing SPIONs with different quantities of peptides per SPION .....	60
Figure 3.2: Assessment of the impact of functionalizing SPIONs with different peptide ratios .....	62
Figure 3.3: Schematic of particle fabrication with three different PEGylation methods .....	63
Figure 3.4: Impact of SPION core size and PEG chain length on $r_1$ .....	68
Figure 3.5: Impact of SPION core size and PEG chain length on $r_2$ CPMG .....	69
Figure 3.6: Comparison between relaxivities derived from $T_2^*$ measurements and $T_2$ CPMG measurements .....	71
Figure 3.7: Impact of SPION core size and PEG chain length on $r_2^*$ .....	72
Figure 3.8: Relationship between $r_2^*$ and CPMG-derived $r_2$ values .....	73
Figure 4.1: Summary of important physical properties of aortic valves .....	89
Figure 4.2: Schematic of Transwell experimental setup .....	98
Figure 4.3: MR results showing the measured signal differences between HABP-, OPN-, and PEG-SPIONs under non-binding conditions .....	102
Figure 4.4: MR results showing the measured relaxivity differences between unbound and bound particles for both HABP-SPIONs and OPN-SPIONs...	103
Figure 4.5: Results from LIVE-DEAD assay .....	105
Figure 4.6: Examination of the impact of HABP- and OPN-SPIONs on HA nucleation and formation <i>in vitro</i> .....	106

Figure 4.7: Comparison of forces generated by blood flow to those generated by centrifugation on the endothelial layer growing on a transwell membrane.. 108

Figure 4.8: Results from transwell experiments .....109

Figure 4.9: Selected images from experiments looking at binding of HABP-, OPN-, and PEG-SPIONs to diseased valve samples and normal tissue ..... 112

Figure 4.10: Heat map representation of experiments testing binding of SPIONs to excised human aortic valve samples ..... 114

Figure 4.11: Results from colocalization studies performed on non-diseased samples ..... 115

## List of Abbreviations

AS	-	aortic stenosis
BCA	-	bicinchoninic acid
CA	-	citric acid
CAVD	-	calcific aortic valve disease
CPMG	-	Carr-Purcell-Meiboom-Gill
CT	-	computed tomography
DI	-	deionized
DLS	-	dynamic light scattering
DSPE	-	1,2-Distearoylphosphatidylethanolamine
EDC	-	1-ethyl-3-(3-dimethylaminopropyl)carbodiimide
FBS	-	fetal bovine serum
HA	-	hydroxyapatite
HABP	-	hydroxyapatite binding peptide
HUVEC(s)	-	human umbilical cord vascular endothelial cell(s)
IA	-	iodoacetyl
kg	-	kilogram
m	-	meter
mm	-	millimeter
μm	-	micrometer
MR(I)	-	magnetic resonance (imaging)
NDRI	-	National Disease Research Interchange

NHS	-	N-hydroxysuccinimide
OA	-	oleic acid
OPN	-	osteopontin based peptide
Pa	-	Pascal
PBS	-	phosphate-buffered saline
PEG	-	poly(ethylene glycol)
PO	-	phosphine oxide
QALY	-	quality-adjusted life year
RT	-	room temperature
s	-	second
SAVR	-	surgical aortic valve replacement
SPION(s)	-	superparamagnetic iron oxide nanoparticle(s)
TAVR	-	transcatheter aortic valve replacement
TEM	-	transmission electron microscopy
TEER	-	TransEndothelial Electrical Resistance
TGA	-	thermogravimetric analysis

## Chapter 1: Introduction and Specific Aims

### 1.1 Motivation: Calcific Aortic Valve Disease and Aortic Stenosis

Calcific Aortic Valve Disease (CAVD) is a general term for any disease that involves calcification of the aortic valve, which serves to control blood flow from the left ventricle of the heart to the aorta and the rest of the body (**Figure 1.1**).<sup>1,2</sup>

CAVD is the most common acquired valvular disorder in developed countries, and is estimated to affect more than 5 million Americans.<sup>3</sup>

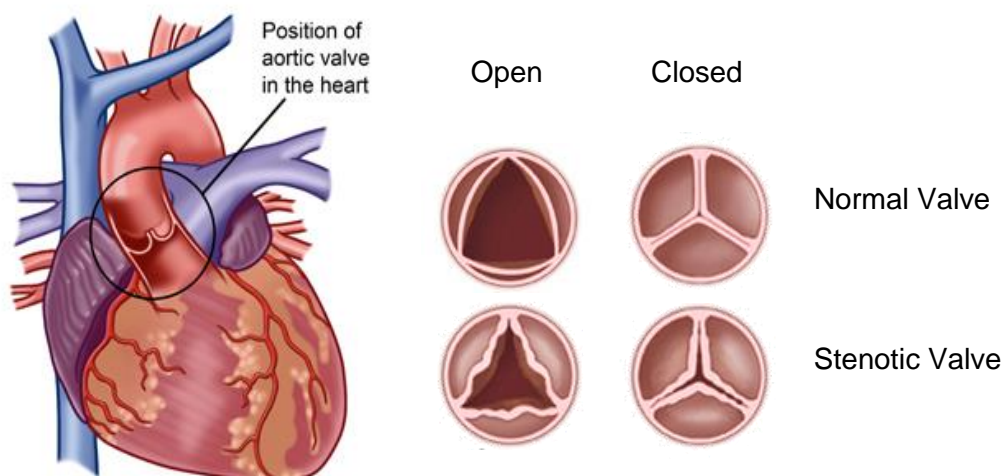


**Figure 1.1:** Illustration of the location of the aortic valve in the heart, as well as the difference between a normal valve and a stenotic valve in the open and closed states. The stenosis both prevents the valve from fully closing and hinders valve opening.

While the specific etiology of the disease is largely unknown, it is understood that greater than 50% of CAVD cases are due to an age-related progressive

calcification, 30–40% of cases are associated with calcification of a congenital bicuspid valve, and fewer than 10% of cases can be traced to acute rheumatic fever post-inflammation.<sup>4</sup> Regardless of the cause, the physiological impact on patients presenting with the disease can be severe.

In its early stages (aortic valvular sclerosis), CAVD is characterized by valve thickening due to lipocalcified deposits without left ventricular outflow obstruction.<sup>5</sup> Up to 25-30% of those over 65 years of age have aortic sclerosis, which is associated with a 50% increase in risk of a cardiovascular event.<sup>6</sup> As sclerosis progresses, the reduction in size of the valve orifice eventually results in hemodynamically significant stenosis, referred to as aortic stenosis (AS).<sup>5</sup> The difference between a normal valve and a stenotic valve is illustrated in **Figure 1.1**.<sup>1,2</sup> AS results in significant negative physiological impacts to patients, including increased ventricular wall stress, decreased stroke volume, and increased end-systolic volume.<sup>4</sup> All told, the physiological consequences of the disease mean that the heart must work harder to pump blood throughout the body, causing the heart muscle to weaken and putting patients at a significantly greater risk of cardiovascular event.<sup>4</sup> Given its prevalence and the aging of the national and global population, CAVD poses a significant socio-economic burden that current standard-of-care practices fail to effectively mitigate.

## **1.2 Current Clinical Practices in Aortic Stenosis**

AS is typically first observed during routine examination of the heart and circulatory system, where certain characteristics of the peripheral pulse or heartbeat can be indicative of the condition.<sup>7</sup> Symptomatic patients may additionally present with shortness of breath, syncope, and chest pain.<sup>5</sup> Confirmation of the diagnosis relies on one of the three primary methods of medical imaging used in the clinic today: ultrasound, computed tomography (CT), or magnetic resonance imaging (MRI).

An echocardiogram (heart ultrasound), the current reference standard for CAVD diagnosis and follow-up, detects leaflet thickening and late changes in transvalvular flow, regurgitation or leakage volume, and pressure differential due to aortic valve area reduction.<sup>8,9</sup> This can confirm the diagnosis by providing information about the physiological parameters as summarized in **Table 1.1**,<sup>4</sup> thus helping to stage the disease as well. In late stages of the disease, Computed Tomography (CT) can readily assess calcium burden, which may also have prognostic value, but cannot assess valve hemodynamics and has limited ability to detect and quantify calcium in early lesions.<sup>10,11</sup> Cardiac magnetic resonance imaging (MRI), although less available, provides similar hemodynamic information to echocardiography in addition to assessing myocardial viability, which can have important prognostic value.<sup>9</sup> Treatment practices and recommendations for patients with aortic valve stenosis vary depending on the disease progression and overall health of the patient at the time of diagnosis.<sup>12</sup>

Severity	Aortic Jet Velocity (m/s)	Mean Pressure Gradient (mmHg)	Aortic Valve Area (cm <sup>2</sup> )
Mild	2.0 – 2.9	< 20	1.5 – 2.0
Moderate	3.0 – 3.9	20 – 39	1.0 – 1.5
Severe	4.0 – 4.9	40 – 59	0.6 – 1.0

**Table 1.1:** Summary of diagnosed aortic stenosis severity based on measured patient parameters.

The recommended clinical practice in mild cases, where the patient may be asymptomatic or mildly symptomatic, is to monitor any changes in condition without further treatment.<sup>13</sup> Patients with mild, asymptomatic aortic stenosis show high rates of event-free survival one year after diagnosis ( $92 \pm 5\%$ ).<sup>14</sup> However the risk of cardiovascular event and/or death increases with each year subsequent to diagnosis, and event-free survival decreases to  $60 \pm 4\%$  after just 5 years.<sup>13</sup> The monitoring approach used in mild cases is necessary by default, as there are currently no widely-accepted lifestyle or pharmacological interventions for early-stage CAVD.<sup>15</sup> Although the effect of lipid lowering via statins has been studied, there is no data to suggest that such measures are effective in preventing or slowing the development of AS.<sup>16</sup>

The preferred treatment for patients with moderate to severe AS (symptomatic or asymptomatic) is valve repair or replacement, without which up to 50% of patients would not survive more than 2 years.<sup>4,17</sup> This replacement may be surgical (surgical aortic valve replacement – SAVR) or, in selected patients, minimally invasive (transcatheter aortic valve replacement – TAVR).<sup>18</sup> TAVR was approved

by the FDA in 2012 as a non-invasive option for high-risk patients, and is currently under examination for lower risk patients in several clinical trials.<sup>19,20</sup> Each year, approximately 75,000 SAVR procedures are performed in the United States, while in 2015, 24,808 TAVR procedures were performed.<sup>19,21</sup> The overall number of aortic valve replacements is projected to increase in the future as the population continues to age.

Although both SAVR and TAVR are effective treatments, both methods remain costly; studies report that each of the >100,000 valve replacements performed in the US per year<sup>22</sup> have associated costs of \$27K-43K per “quality-adjusted life year” (QALY) for SAVR, and \$55-\$62K per QALY for TAVR.<sup>23</sup> Valve replacement surgery also significantly impacts patients’ lives, with recovery times up to 10-12 weeks for high activity work.<sup>4</sup> In addition, patients may experience adverse post-surgical events such as stroke, atrial fibrillation, or valve deterioration/restenosis.<sup>24,25</sup>

Despite the extensive cost, recovery time, and heightened risk of post-surgical complications to patients, surgical approaches are often the only option for patients with aortic stenosis due to late diagnosis of the condition. Ultimately, no clinical imaging method currently available has the ability to reliably detect early CAVD, necessarily delaying diagnosis until patients are symptomatic and the disease has progressed to its late stages.<sup>4,17,26–29</sup> The lack of diagnostic imaging techniques capable of detecting and monitoring early-stage disease is a major unmet need in

the development of new treatments of CAVD.

### ***1.3 Characteristics of Early Stage CAVD***

Earlier diagnosis of CAVD would necessarily rely on early disease markers and characteristics. Fortunately, early CAVD progression continues to be a heavily researched topic, with a wide body of published literature available.

Current thinking postulates that the disease is initiated by endothelial disruption due to increased mechanical or decreased shear stress on the aortic valve. Although the cause of these changes in stress may not be known, hypertension is thought to play a role based on clinical research in humans.<sup>30,31</sup> It has been hypothesized that hypertension may result in high tensile stress on the leaflets of the aortic valve, or, alternately, that high volume flow rates such as those observed in patients with hypertension may cause turbulent blood flow patterns and low shear stress.<sup>32,33</sup> In either of these scenarios, endothelial disruption or injury would result.

As with atherosclerosis, this endothelial disruption is followed by inflammation, collagen and extracellular matrix disruption, lipoprotein deposition, and formation of microscopic calcification sites.<sup>5,34–37</sup> Although much of this research has been performed on samples from human aortic valves, some of it has been performed using mouse models similar to those used for atherosclerotic research, and thus

results may not necessarily translate directly to the disease path in human aortic valve disease. Photomicrographs depicting these changes to can be seen in **Figure 1.2**, along with comparisons to normal valve tissue.

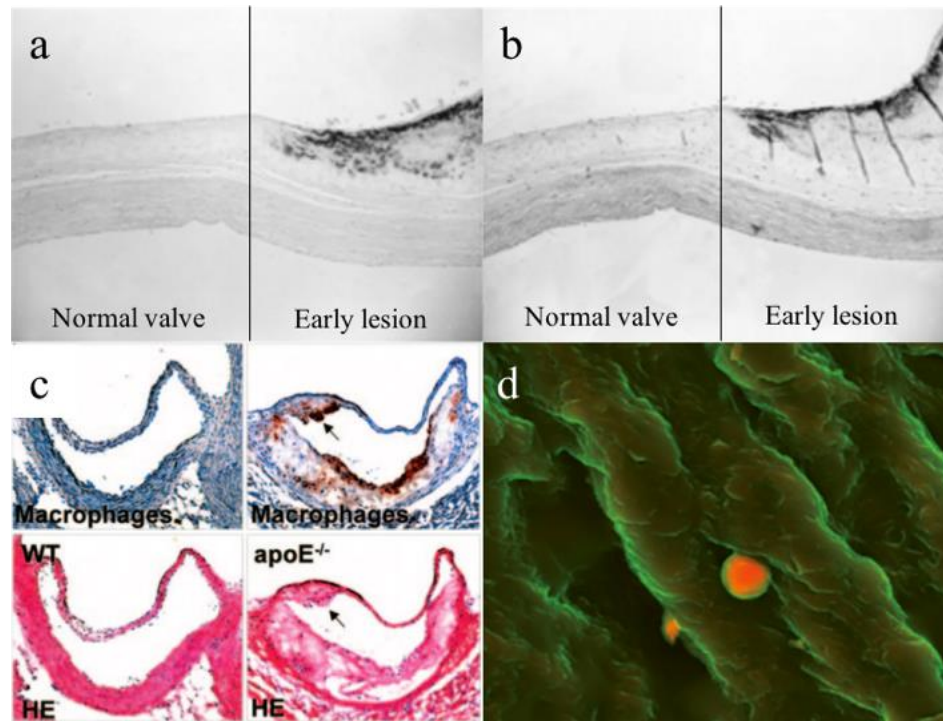


**Figure 1.2:** (A) Apolipoprotein B is observed in morphologically early human aortic valve lesions but not in normal valve regions through low-power photomicrograph stained via immunoreaction, (B) Apolipoprotein a is observed in morphologically early human aortic valve lesions but not in normal valve regions through low-power photomicrograph stained via immunoreaction, (C) Aortic valve leaflets of wild-type mice are thin with no macrophage infiltration, while leaflets of 30-week-old, hypercholesterolemic apolipoprotein E–deficient mice have an increased overall thickness associated with macrophage accumulation (D) Density dependent color SEM micrographs of human aortic valve presenting microcalcifications.

As the disease progresses, active calcification and lesion formation are observed; this may be in part due to the transdifferentiation of cardiovascular cells into

osteoblast-like cells.<sup>5,34–36</sup> These stages of the disease precede the typically diagnosable markers previously discussed such as decrease in aortic valve area and increase in aortic jet velocity.<sup>5,34–36</sup> Although early CAVD remains an active field of research, there has been little to no impact of this research on clinical treatment or diagnosis of CAVD and AS at this time.

#### ***1.4 Medical Imaging and Contrast Agents***

The growing and detailed understanding of early-stage CAVD admits the possibility of earlier diagnosis via ultrasound, CT, or MRI. MRI has distinct advantages over both ultrasound imaging and CT scans for potential applications in early CAVD detection. Ultrasound imaging of heart structures (echocardiography) suffers from interference from nearby bone or air, and results are often very operator-dependent, while CT scans carry a high dose of ionizing radiation which may become dangerous for the patient upon repeated exposure and scanning.<sup>8–10</sup> MRI is advantageous because it can provide more information about blood flow, more accurate tissue characterization, and often, better image contrast than other imaging modalities.<sup>8</sup> However, as discussed previously, MRI is not currently sensitive enough to detect early signs of CAVD, including valve thickening and the presence of microcalcifications. The use of a contrast agent would increase MRI sensitivity, and make it possible to use this imaging modality for early CAVD detection.

MRI contrast agents function by altering either longitudinal ( $T_1$ ) or transverse ( $T_2$ ) relaxation times of protons in proximity to the contrast agents (**Figure 1.3**).<sup>38–42</sup> To the viewer, this results in a change in the grey-scale image produced by the scan that can serve to highlight or darken desired features.

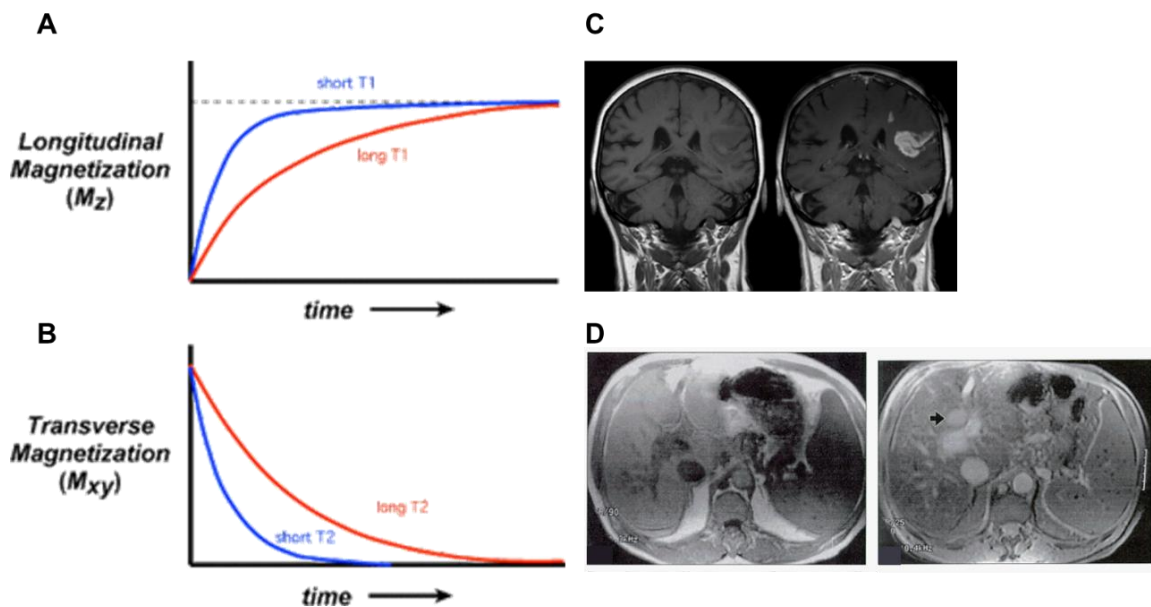


**Figure 1.3:** Illustration of the impact **(A)** longitudinal ( $T_1$ ) and **(B)** transverse ( $T_2$ ) MRI contrast agents. Contrast agents act to shorten  $T_1$  or  $T_2$  (blue line) in comparison to a scan without contrast (red line). MRI images with **(C)** longitudinal (gadolinium-based) and **(D)** transverse (iron-oxide based) contrast agents applied. Panels on the left are scans taken prior to the administration of contrast; panels on the right are scans taken after contrast agent administration.<sup>40–42</sup>

The two most commonly researched MRI contrast agents currently are gadolinium-based agents and iron-oxide-based agents. Gadolinium-based agents preferentially shorten  $T_1$  relaxation rates at low doses (**Figure 1.3C**), and so yield “bright spots” in areas of accumulation in  $T_1$ -weighted images.<sup>43</sup> However, gadolinium-based agents have been shown to carry potential safety risks,

including nephrotoxicity and neurotoxicity.<sup>44-47</sup> Superparamagnetic iron oxide nanoparticles (SPIONs) are iron-oxide-based MRI contrast agents that function by reducing the T<sub>2</sub> signal of nearby tissue, leading to a darkened area in T<sub>2</sub>-weighted MRI images (**Figure 1.3D**).<sup>38,48</sup> Several SPION-based MRI contrast agents have been approved by the FDA for clinical use for various indications, and they continue to be an active area of research.<sup>49,50</sup> SPIONs have the further advantage of not presenting the same associated safety risks as gadolinium-based contrast agents.<sup>45</sup> However, hypersensitivity or anaphylaxis reactions have been reported in the FDA-approved, carbohydrate-coated iron oxide agent Feraheme,<sup>51</sup> indicating that further clinical evaluation of any potential iron-oxide based contrast agent would be of the utmost importance. Literature demonstrates that SPIONs can be surface-functionalized using fairly basic chemistry techniques, allowing them to be targeted toward specific cells or cell characteristics.<sup>52-55</sup> This opens up a wide variety of applications, including specific disease detection.

### ***1.5 Research Objective Statement***

The stated goal of this dissertation is to develop and characterize a novel contrast agent for MRI to aid in earlier detection of CAVD by using chemically modified and targeted SPIONs (see **Figure 1.4**). Earlier CAVD diagnosis and improved monitoring could lead to an increased understanding of the risk factors associated with progression of the disease, thereby improving predictions as to which patients

are at risk of developing moderate to severe disease. Early diagnosis may also enable the identification of targets for future therapeutics, and potentially open the door for earlier treatment options aimed at halting CAVD progression that are not currently possible. For example, several pharmacologic interventions have been suggested to influence CAVD by targeting specific pathways such as the renin-angiotensin system or oxidative stress.<sup>56-58</sup>

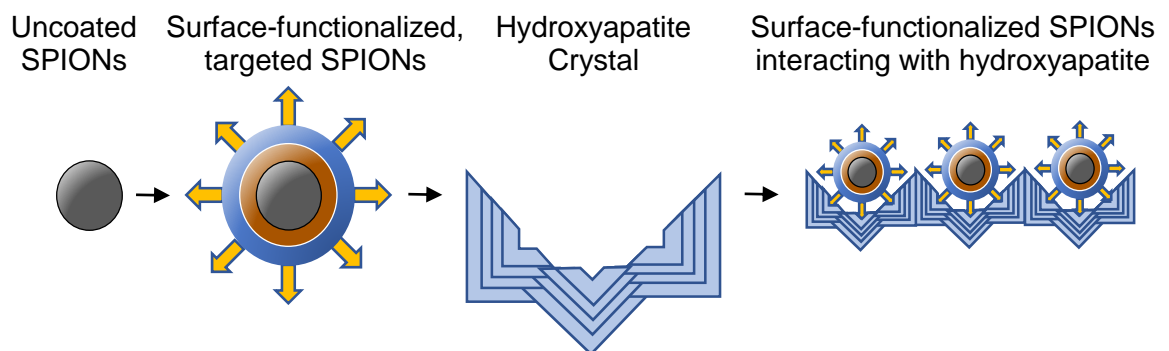


**Figure 1.4:** Example schematic of functionalizing SPIONs so that they can be used to bind to and target hydroxyapatite, a feature in the microcalcifications present in early CAVD. Note: not drawn to scale.

The first step towards achieving this objective is the selection of a target suitable for early detection of CAVD. Out of many potential disease markers, we have selected hydroxyapatite (HA) – a crystalline calcium phosphate mineral that is also abundant in bone. Similar approaches can be found in the literature; Chin, et al. have recently published a review summarizing work that has examined calcium-binding nanoparticles for vascular disease.<sup>59</sup> HA is one of the main components in valve lesions and is specifically indicative of the ongoing active calcification

processes that are characteristic of CAVD.<sup>5,10,60</sup> In addition, deposition of HA in the valve scales with disease severity, which is crucial to its utility as a target for a contrast agent capable of detecting disease earlier than is currently possible.<sup>61</sup> Although large HA deposits are found in severe CAVD, microcalcifications partially composed of HA are known to be present early in the disease (see **Figure 1.2**).<sup>34</sup> This makes HA the ideal target for the proposed contrast agent, since the presence of calcifications is a more specific marker of early stage CAVD than lipoprotein deposition or the presence of inflammatory markers or cells (e.g. macrophages).

## **1.6 Specific Aims**

This dissertation is divided into three specific aims that focus on fabrication and characterization of HA-targeted SPIONs and their binding, MR, and medical properties.

**Aim 1:** Fabrication and *in vitro* characterization of targeted SPIONs. For this aim, we have designed a fabrication schema that will result in HA-targeted and PEGylated SPIONs. Additionally, we have characterized the size and zeta potential of the SPIONs as well as the success of each functionalization step. Finally, we have characterized SPION binding to targeted and off-target surfaces, both with and without the presence of serum proteins.

**Aim 2:** Optimization of SPION binding and MR properties. For this aim, we have examined the impact of altering fabrication parameters of the SPIONs, including both their targeting peptide coating as well as the antibiofouling polymeric layer. These alterations were examined in light of either the ability of the SPIONs to bind to their target or the strength of the MR signal generated in order to optimize the fabrication process to produce nanoparticles with ideal binding and MR properties.

**Aim 3:** Characterization of the medical properties of targeted SPIONs. For this aim, we have examined the impact of targeting peptide addition on MR signal and assessed whether binding to HA could be detected via MR. We have also examined the impact of HA-targeted SPIONs on the formation of crystalline HA *in vitro*, tested the ability of the particles to exhibit binding to HA in MR scan, and observed particle translocation through an endothelial layer, with successful binding to HA occurring subsequently. Finally, we have tested the ability of these targeted SPIONs to bind to HA in excised human valve samples.

The findings reported in this dissertation provide a targeted, optimized MR contrast agent that may be capable of aiding in earlier detection of CAVD. In addition, the results from MR optimization of the particles have yielded important information that is widely useful in the development of any novel MR contrast agent in the future.

## Chapter 2: Fabrication and *In Vitro* Characterization of SPIONs<sup>62</sup>

### 2.1 Introduction

In order to produce HA-targeted SPIONs, a number fabrication and chemical functionalization steps must be undertaken (see **Figure 2.1**). Several methods of chemically functionalizing nanoparticle surfaces, thereby targeting them to specific cells or tissues, have been previously developed and described in the literature. These methods include functionalization of the nanoparticle surface with biological or biologically-derived molecules such as antibodies, peptides, or aptamers intended to interact with specific proteins.<sup>53,54,63–65</sup> For some applications (e.g. cancer treatment) these specific interactions may be intended to cause uptake of drug-carrying nanoparticles into cells via receptor-mediated endocytosis.<sup>55,66–68</sup> For applications such as disease detection, it is simply necessary for the interaction between the targeting moiety and the target to cause association of the nanoparticle with the disease target.<sup>69,70</sup> These studies will describe the development of a targeted SPION designed to associate with HA.

In order to target HA, two peptides have been selected and tested for SPION functionalization (see **Figure 2.1**). The first is a modified hydroxyapatite-binding peptide (HABP) characterized by Roy et al. using ribosome display.<sup>71</sup> The second is a modified and highly phosphorylated osteopontin-derived peptide (OPN) described and characterized by Hunter and Wang, et al.<sup>72,73</sup> These two peptides were chosen because it was hypothesized that their different origins (synthetic vs.

biological) and different properties (due to their differing amino acid compositions) may confer distinct properties upon functionalized SPIONs.

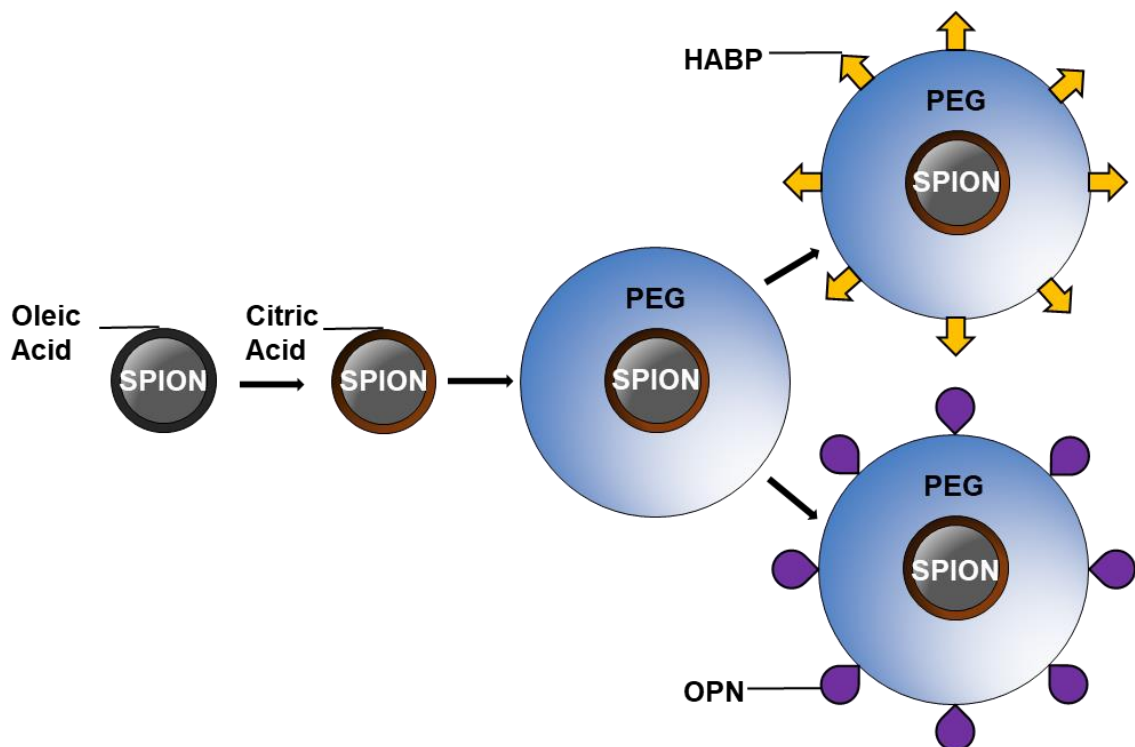


**Figure 2.1:** Schematic representing the fabrication and functionalization of HA-targeted SPIONs. A ligand exchange is performed on magnetic SPION cores coated in oleic acid to produce SPIONs coated in citric acid, and citric acid coated SPIONs are PEGylated using EDC/NHS chemistry. Targeting peptides HABP and OPN are added via an iodoacetyl/thiol interaction between iodoacetyl-PEG and peptides with cysteine residues. Specific methods are further discussed in Section 2.2.

Although specific targeting via antibodies, peptides, or aptamers has shown high rates of success *in vitro*, these methods have often failed *in vivo*.<sup>74-76</sup> One of the primary causes of *in vivo* failure is the formation of the so-called protein corona that occurs almost instantaneously upon exposure of nanoparticles to protein-rich media such as blood serum.<sup>77-79</sup> The composition of the protein corona in terms of protein type, concentration, and conformation varies depending on the specific

surface functionalization of the nanoparticles,<sup>80,81</sup> and can define their biological fate including biodistribution, cellular uptake, and immune response.<sup>82,83</sup> Additionally, the presence of the corona can block targeting moieties from interacting with their targets, causing a loss of targeting efficiency.<sup>84,85</sup> Previous results in the literature indicate that the protein corona can inhibit the targeting capability of nanoparticles by as much as 94%, even in a solution that is only 10% serum.<sup>84</sup> The protein corona consists of two layers: (1) the hard corona close to the nanoparticle surface, comprised of higher affinity proteins that may irreversibly bind to nanoparticles, and (2) the soft corona formed by loosely affiliated, lower affinity proteins that are reversibly bound and may exchange over time with proteins in the surrounding solution.<sup>86,87</sup> It has been hypothesized that the hard protein corona, which is both closer to the nanoparticle surface and more tightly associated, may have a greater impact on nanoparticle targeting capabilities.<sup>82,88</sup>

To prevent deposition of serum proteins, nanoparticles are commonly coated in an antibiofouling layer such as poly(ethylene glycol) (PEG) prior to the addition of targeting moieties.<sup>89,90</sup> PEG is thought to display good resistance against nonspecific protein adsorption in large part due to its extensive formation of hydrogen bonds with surrounding water.<sup>91</sup> However, recent findings have suggested that protein adsorption to the nanoparticle surface occurs even in nanoparticles that have been coated in PEG.<sup>92,93</sup> Studies show that, even at low concentrations of serum (10%), protein deposition still occurs onto PEGylated nanoparticle surfaces.<sup>94</sup> Given that blood is comprised of approximately 50-55%

protein-rich serum, this would present some obvious problems in the *in vivo* environment.

Unlike many other targeted nanoparticles, HA-targeted SPIONs do not need to be taken up by cells in order to be efficacious. Although the specific protein-protein or peptide-protein interactions required for specific cellular uptake are highly susceptible to blockage by the protein corona,<sup>64,95,96</sup> the effects of the protein corona have not been so thoroughly investigated for targeting strategies that do not require cellular uptake. In fact, targeting of non-protein disease features such as HA has not been examined at all.

To test the ability of HA-targeted SPIONs to maintain specific targeting capabilities even in the presence of serum proteins, we conjugated the two different HA-binding peptides (HABP and OPN) to PEGylated SPIONs and tested their binding properties in parallel. We assessed the specific and non-specific binding of these functionalized SPIONs in sodium phosphate buffer before characterizing the interaction of the nanoparticles with serum proteins in a 50% serum environment, to most accurately imitate the protein-rich *in vivo* environment. We additionally assessed the protein corona of the particles, to develop a better understanding of factors that may influence the ability of nanoparticles in general to bind to their targets in the presence of serum proteins.

Our findings demonstrated that, while our peptide-coated SPIONs show substantial interactions with serum proteins and the immediate development of a

protein corona, the majority of the observed interactions with serum proteins are loose associations (i.e., part of a soft corona). This has allowed these peptide-linked, HA-targeted SPIONs to maintain successful binding to HA even in the presence of serum. We hypothesize that this is due to the primarily charge-based interaction between the targeting peptides and HA,<sup>71,72</sup> which may help to avoid some of the typical problems observed with relying on specific protein-protein interactions to allow for targeted binding in high-protein environments. The work in this chapter has implications in the selection of targets for future work on targeted nanoparticles, in addition to offering proof-of-concept that these HA-targeted SPIONs may have utility in the detection of CAVD.

## **2.2 Materials and Methods**

### *Materials*

Iron tri(acetylacetonate), 1,2-tetradecanediol, oleic acid, oleylamine, dibenzyl ether, citric acid, diethyl ether, 2-methoxyethylamine, N-(3-Dimethylaminopropyl)-N'-ethylcarbodiimide hydrochloride (EDC), N-Hydroxysuccinimide (NHS), 1,2-dichlorobenzene, and N,N'-dimethylformamide were all purchased from Sigma-Aldrich (St. Louis, Missouri). Human Umbilical Cord Vascular Endothelial Cells (HUVECs) and cell media were acquired from Lonza (Portsmouth, New Hampshire). When it was purchased (as indicated in the Results and Discussion

sections), HA powder was also purchased from Sigma-Aldrich (St. Louis, Missouri). All functionalized PEG reagents were obtained from Nanocs (Boston, Massachusetts). Slide-A-Lyzer dialysis cassettes were acquired from Thermo Scientific (Rockford, Illinois). Fetal Bovine serum was obtained from Hyclone (Logan, Utah).

All statistical analysis and figure generation were performed in R (version 3.5.1), and graphed using ggplot2.

#### *Iron oxide particle synthesis and surface modification*

Oleic acid-coated iron oxide nanoparticles were synthesized via high-temperature thermal decomposition as previously described.<sup>97</sup> Briefly, the following reagents were mixed and stirred magnetically under nitrogen flow: 2mmol iron(III) tri(acetylacetonate), 10mmol 1,2-tetradecanediol, 6mmol oleic acid, 6mmol oleylamine, and benzyl ether. The resulting nanoparticles were precipitated in excess ethanol and pulled down using a magnet. The precipitated particles were washed with ethanol, dissolved in hexane, and centrifuged to remove aggregates. Oleic-acid coated SPIONs produced using this method were dried in a vacuum oven.

A ligand exchange served to replace oleic acid with citric acid. Oleic acid-coated nanoparticles and citric acid were dissolved in a 1:1 mixture of dichlorobenzene

and N,N-dimethylformamide. The mixture was heated to 100°C and left stirring for 24 hours. Citric acid-coated nanoparticles (CA-SPIONs) were precipitated in diethyl ether and washed with acetone and diethyl ether before drying in a vacuum oven.

CA-SPIONs were further coated with a layer of bifunctionalized PEG using a protocol similar to those previously described.<sup>97,98</sup> CA-SPIONs were dissolved in pH 9 sodium phosphate buffer with desired amine-terminated PEGs, combined with N-hydroxysuccinimide ester (NHS) and 1-ethyl-3-(3-dimethylaminopropyl) carbodiimide (EDC), and agitated for 24 hours at room temperature. For particles that would be further functionalized with HA-targeted peptides, PEG was added at a 1:4 molar ratio of NH<sub>2</sub>-PEG3.4k-iodoacetyl to NH<sub>2</sub>-PEG2k. SPIONs not functionalized to bind to HA were PEGylated with a 1:4 molar ratio of NH<sub>2</sub>-mPEG3.4k to NH<sub>2</sub>-mPEG2k. The resulting PEGylated SPIONs were purified by dialysis in all cases.

Two different HA-binding peptides were purchased from Peptide 2.0 (Chantilly, Virginia). HA Binding Peptide (HABP – SVSVGGMKPSRPGGGKC) and an osteopontin-derived peptide (OPN - DDVDD(pT)DD(pS)HQ(pS)DEGGGKC) were linked to SPIONs via an iodoacetyl-thiol interaction to produce either HABP-SPIONs or OPN-SPIONs. Peptides were added to iodoacetyl-PEG-SPION solutions in appropriate concentrations to target the addition of 25 peptide residues per SPION. Peptide addition reactions were allowed to run overnight at 4°C, and

conjugated particles were purified from excess peptide by dialysis against deionized water at 4°C.

A schematic of the overall SPION functionalization process can be seen in **Figure 2.1** above.

#### *Dynamic Light Scattering, Zeta Potential, BCA Assay Characterization, and TEM*

The size and zeta potential of HA-SPIONs were measured via dynamic light scattering (DLS) in pH 9 sodium phosphate buffer. All measurements were made with a 90Plus Dynamic Light Scattering Analyzer (Brookhaven Instruments) at a 90° detection angle. All samples were diluted 10x before measurement, as it has been previously indicated that high SPION concentrations may impact DLS readings.<sup>99</sup> DLS measures the impact of nanoparticle movement on light scattered through a solution of small nanoparticles, and from these measurements, the size of the particles causing the light to scatter can be inferred. The bicinchoninic acid assay (BCA assay) was used to quantify success of peptide addition to SPIONs. For the BCA, each peptide (HABP or OPN) was used to construct a calibration curve (rather than the much-larger bovine serum albumin provided) in order to obtain a more accurate measurement of the quantity of peptide present.

The shape and size of the SPIONs were examined on a JEOL 2100 (200 kV) transmission electron microscope (Tokyo, Japan). The samples were prepared by

placing a few drops of nanoparticle suspension onto a standard carbon-coated copper grid and then drying at ambient conditions. The TEM images were processed in ImageJ (NIH) to determine particle size and size distribution. All distinctly visible and easily delineated SPIONs in a given image were selected using the circular outline feature, and diameter was estimated by comparison to the scale bar (included in the images).

#### *In Vitro Binding Tests in Sodium Phosphate Buffer*

HA-SPIONs were shaken at room temperature (RT) for 30 minutes with HA in Costar Spin-X centrifuge tube filters over a range of HA quantities (0-200mg). After incubation, all samples were centrifuged at 3000 rpm for 3 minutes. The absorbance of the filtrate was measured at 510nm to determine the relative percentage of particles bound to the HA. Particles bound to HA cannot successfully pass through the filter, while unbound particles pass through easily. These experiments were repeated over a range of pH values (7.1-7.8).

The specificity of HA-SPION binding to HA was tested by comparing results from HA binding tests with results from experiments testing off-target binding to cholesterol, collagen, fibrin, fibrinogen, and human vascular endothelial cells (HUVECs). All off-target binding surfaces were produced to target 25mg of the off-target component per well, with the exception of HUVECs. A collagen-coated six-

well plate was used to test off-target HA-SPION binding to collagen, fibrin, and fibrinogen. For both the fibrin and fibrinogen gels, fibrinogen (Bovine plasma, Sigma-Aldrich) in pH 7.1 sodium phosphate buffer was incubated at RT for 10 minutes to allow binding to the collagen surface coating. Thrombin in PBS (Bovine plasma, Sigma-Aldrich) was used to crosslink fibrinogen into a fibrin gel for 1 hour. For the HA-coated plates, a protocol similar to that developed by de Bruyn *et al.* was adapted;<sup>100</sup> in short, two working solutions were prepared (12mM CaCl<sub>2</sub> and 7.5mM Na<sub>2</sub>HPO<sub>4</sub>), and were added in appropriate ratios to stoichiometrically yield 25mg of HA (Ca<sub>10</sub>(PO<sub>4</sub>)<sub>6</sub>(OH)<sub>2</sub>) upon full conversion of the salt components to a crystalline form. These solutions were mixed and allowed to dry on top of the fibrin gels, producing a thin HA coating that effectively adhered to the plate. All wells were washed twice with buffer and allowed to dry under vacuum.

Once the wells had dried, a 10x diluted SPION solution was added to each well and incubated for 30 minutes at RT. After incubation, samples were pulled from each well and filtered through a 0.2µm filter. The absorbance of each sample was measured at 510nm and compared to the absorbance of prepared samples of known SPION concentration or quantity to assess the number of SPIONs present after binding has been allowed to occur.

To test HA-SPION binding to cholesterol, one well of a tissue culture-treated six-well plate was filled with cholesterol in ethanol solution, and the ethanol was allowed to completely evaporate. After incubation, samples were pulled from each

well and filtered through a 0.2 $\mu$ m filter. The absorbance of each sample was measured at 510 nm and compared to the absorbance of prepared samples of known SPION concentration or quantity to assess the number of SPIONs present after binding has been allowed to occur.

To test binding against HUVECs, the cells were cultured at recommended conditions in 6-well plates. After a week in culture, at which time the cells were observed to be confluent, cells were pre-incubated at 4°C for 10 minutes to halt endosomal trafficking. 50 $\mu$ L of an HA-SPION solution was added to each well of the 6-well plate, and plates were incubated at 4°C for 30 minutes. Absorbance at 510nm was measured for samples of the media taken after incubation to determine the percentage of HA-SPIONs that remained in solution and did not adhere to HUVECs.

#### *SPION binding to Serum Proteins*

HABP-SPIONs, OPN-SPIONs, and PEG-SPIONs were each mixed 1:9 with a 50% fetal bovine serum (Hyclone) solution. The solution was transferred to a cuvette and allowed to sit at room temperature for 24 hours. DLS measurements were taken at specific time points (0 and 30 minutes; 1, 2, 4, 8, 12, and 24 hours) to observe any alterations in effective diameter of the SPIONs. These results were compared with samples that have been incubated similarly with DI water. These experiments were additionally repeated without timed incubation at various pH

levels (6-9).

To assess the amount of protein bound to the SPIONs, HABP-SPIONs, OPN-SPIONs, and PEG-SPIONs were each mixed 1:9 with 50% serum solution and incubated at room temperature for two hours. None of the prepared solutions showed visible signs of aggregation. All particles were washed by centrifugation 3x to remove unbound serum proteins (17900g for 30 min at 4°C) and resuspended in 200µL of DI water. DI water was chosen as a diluent and resuspension agent in these studies because the presence of salt can screen the repulsion between nanoparticles and induce aggregation;<sup>101</sup> for these studies, it was important to limit aggregation as much as possible during resuspension, in order to obtain an accurate final assessment of the final number of proteins per particle after all wash steps. Samples were removed after each washing step for subsequent protein measurement using the BCA assay, where they were compared to samples incubated in DI water as a control. Aliquots of samples incubated with either 50% serum or DI water and washed 3x were mixed 4:1 with Laemmli sample buffer and boiled in water for 5 minutes. These samples were loaded on a 4-20% Tris-glycine gel in Laemmli running buffer and resolved at 150V for 50 minutes at room temperature. After electrophoresis, the gel was fixed with 10% v/v acetic acid and 30% v/v ethanol for at least 30 minutes and stained with silver nitrate stain (Pierce) according to the manufacturer's protocol. The stained gel was scanned using a VersaDoc Scanner from Bio Rad and the scanned image is imported into ImageJ and cropped.

### *In Vitro Binding Tests in Serum*

Serum absorbs light at ~510nm, so an orthogonal method was used to measure SPION binding to specific surfaces in serum, although the protocol remained identical aside from the method of measurement. Plates were coated in cholesterol, collagen, fibrin, fibrinogen, and HA as previously described. All wells were washed twice with buffer and allowed to dry under vacuum.

Each coated well was incubated in a 50% fetal bovine serum solution for 30 minutes, while functionalized SPIONs (HABP-SPIONs, OPN-SPIONs, PEG-SPIONs, and CA-SPIONs) were simultaneously incubated at room temperature for 30 minutes. Serum was removed from the wells, and the SPIONs were diluted 1:9 in a 50% serum solution and incubated on the coated wells for 30 minutes at room temperature. After incubation, the SPION solutions were removed and wells were washed with DI water. All wells were stained with a Prussian Blue stain to detect iron for 35 minutes. Wells were rinsed again, allowed to dry under vacuum, and imaged on an Axiovert S100 microscope. To quantify the number of particles remaining, these images were compared to images of these same, identically-produced surfaces with known quantities of nanoparticles deposited on the surfaces. For example, images of fibrin surfaces with known quantities of PEG-SPIONs deposited onto the surface were used to act as a “calibration curve” for experimental samples of PEG-SPIONs deposited onto fibrin surfaces. From this information for all unique combinations of functionalized SPIONs and surfaces, the

number of particles (as a function of the “image darkness” due to the stain) was estimated. Image greyscale analysis was performed in ImageJ.

## 2.3 Results

### *Iron oxide particle synthesis and surface modification*

SPIONs cores, produced by high temperature thermal decomposition, have a core size of ~10nm as confirmed by TEM (**Figure 2.2**).

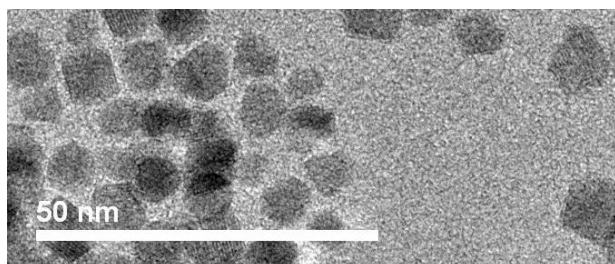


**Figure 2.2:** TEM image of ~10nm SPION cores. SPION core sizes were quantified in ImageJ, which yielded an average core size of  $9.39 \pm 0.98$ nm (mean  $\pm$  standard deviation).

SPIONs produced by high-temperature thermal decomposition are coated in oleic acid (**Figure 2.1**), which is highly hydrophobic. The ligand exchange was performed with citric acid to produce hydrophilic SPION cores (CA-SPIONs) that can be further functionalized by well-characterized methods utilizing the large number of available carboxylic acid residues present on the modified SPION surface. CA-SPIONs were further functionalized with PEG, which acts as an antibiofouling agent. A heterobifunctionalized iodoacetyl-PEG-NH<sub>2</sub> was selected to allow for subsequent functionalization of PEGylated particles with either HABP or OPN.

*Dynamic Light Scattering, Zeta Potential, BCA Assay Characterization, and TEM*

Successful coating of SPIONs with citric acid, PEG, and desired peptides was confirmed by DLS results, zeta potential measurements, and the BCA assay (**Table 2.1**). CA-SPIONs are expected to be the smallest in size, with size increasing at every step of functionalization. Additionally, CA-SPIONs are expected to be highly negatively charged due to the presence of multiple carboxylic acid residues around the core. PEGylated SPIONs are expected to have a zeta potential closer to neutral, which was confirmed (**Table 2.1**).

Fabrication Stage	Effective Diameter (nm)	Zeta Potential (mV)
CA-SPIONs	13.2	-35.1
PEG-SPIONs	19.2	-11.4
HABP-SPIONs	20.5	-30.8
OPN-SPIONs	25.1	-31.3

**Table 2.1:** DLS and zeta potential measurements of SPIONs at various stages of fabrication indicate success of functionalization. As expected, particle size increased with the addition of each surface modification. Additionally, zeta potential changes reflect the change in surface groups at each stage. Data presented as mean of 3 independent runs of particle fabrication.

Successful conjugation of either peptide (ribosome-display derived HABP or osteopontin-derived OPN) was confirmed via the BCA assay. BCA assay results yield a peptide concentration value for a given solution of peptide-coated SPIONs;

this peptide concentration, along with the measured quantity of SPIONs in the solution, was used to calculate the approximate number of peptides per SPION. Because the conjugation reaction was performed to target 25 peptides per SPION, we were able to calculate from these results an approximate reaction efficiency and approximate number of peptides conjugated per SPION. BCA assay results after peptide addition indicate a 72% reaction efficiency for the addition of HABP to SPIONs (~18 peptides/SPION) and a 92% reaction efficiency for the addition of OPN to SPIONs (~23 peptides/SPION).

HABP and OPN properties were evaluated using the online tool available from GenScript.<sup>102</sup> Properties of the peptides are summarized below (**Table 2.2**).

Property	HABP	OPN
Isoelectric Point	10.79	3.58
Charge	3	-6
Attribute	Basic	Acidic
Number of Hydrophobic Residues	6	1

**Table 2.2:** Summary of the peptide properties of both HABP and OPN. As expected, the peptides have different chemical properties due to their differing amino acid sequences. These properties may play an important role in functionalized SPION behavior. In particular, the differences in charge and number of hydrophobic residues are likely to confer different properties in HABP-SPIONs when compared to OPN-SPIONs.

### *In Vitro* Binding Tests in Sodium Phosphate Buffer

Functionalized SPION binding to HA was evaluated in sodium phosphate buffer via an *in vitro* assay developed for this purpose (**Figure 2.3**). HA-targeted SPIONs, coated with either HABP or OPN, bind to HA in centrifugal filter tubes in a dose-dependent manner as expected – e.g. the solution in the tube farthest to the left (0mg of HA) is much darker in color than the solution in the tube farthest to the right (200mg HA), indicating that fewer nanoparticles remain unbound and in solution with increasing quantities of HA (**Figure 2, A and B**). HABP-SPIONs bind in significantly ( $p < 0.05$ ) higher quantities than OPN-SPIONs to comparable amounts of HA at lower quantities of HA.

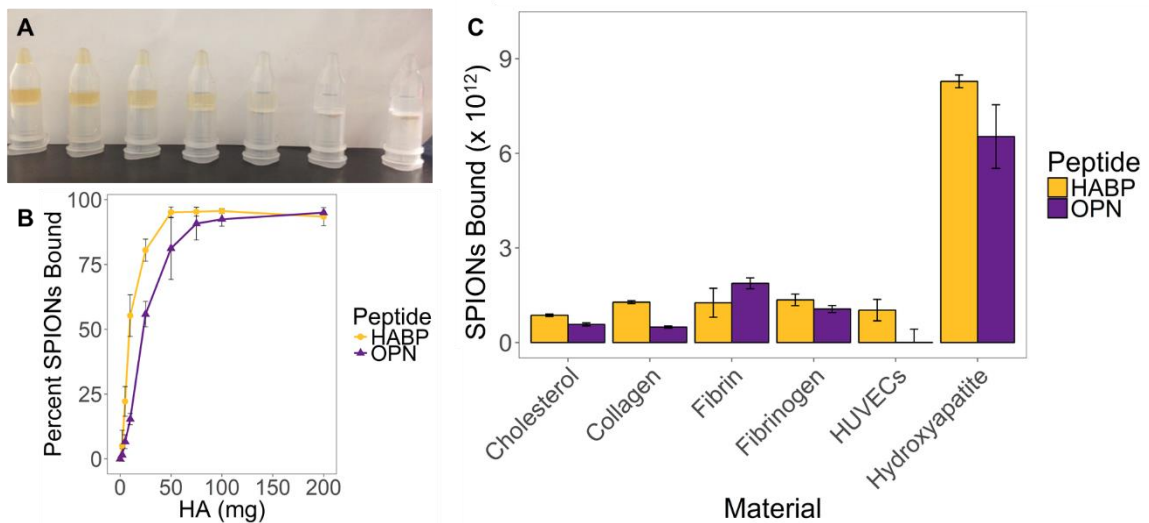


**Figure 2.3:** (A) Binding of HABP SPIONs to HA. From left to right, tubes contain 0, 5, 10, 25, 50, 100, and 200mg of HA. After filtration of the hydroxyapatite, the concentration of SPIONs remaining in the tubes is visibly different depending on the amount of HA in each tube – higher quantities of HA result in fewer particles remaining unbound. (B) Quantification of SPION binding from samples bound in the same setup as that illustrated in (A). Generally, 50mg of HA was sufficient to fully bind  $9.5 \times 10^{13}$  HABP-SPIONs, and

$7.7 \times 10^{13}$  OPN-SPIONs. **(C)** Quantification of HABP- and OPN-SPION binding to various biologically-relevant surfaces. HA-targeted SPIONs bind significantly more to HA than to other surfaces tested, although some degree of off-target binding did occur. Error bars are standard deviation; n=3.

For the studies in Figure **2.3A** and **B**, powdered HA was purchased from Sigma. This purchased form of HA does not lead to issues with the centrifugal filtration used for these experiments. Equal flow of liquid through the filter upon centrifugation is observed in all samples (**Figure 2.3A**); only the quantity of nanoparticles, assessed via an absorbance assay, differs. On the other hand, HA as formed by evaporation of mixed calcium and phosphate solutions lead to issues with filtration in the centrifugal filter tubes, but not in the syringe filters (data not shown). Therefore, for **Figure 2.3C**, the evaporation method was preferred, as this method is more likely to produce the mix of crystalline HA and amorphous, insoluble calcium phosphate that is more reflective of what may be found biologically.<sup>103,104</sup>

SPIONs suspended in sodium-phosphate buffer do not exhibit binding to other biologically-relevant off-target molecules (**Figure 2.3C**). These experiments were performed by coating the surface of cell culture plates in biologically-relevant substances (cholesterol, collagen, fibrinogen, fibrin, or HUVECs) and allowing binding to occur. For these studies, all surfaces (including HA) were fabricated such that there were ~25mg (or as close as possible to this target) of each material present for binding tests. For HUVECs, these studies were performed once

HUVECs reached confluence. The number of SPIONs was determined by comparing the absorbance of the filtrate to the absorbance of solutions with known quantities of nanoparticles. This method was chosen to account for any potential differences in the starting concentrations of the various nanoparticle solutions used. Low levels of non-specific binding are expected and observed, but binding to HA occurs at much higher levels; at least 5.23x and 4.28x more for HABP- and OPN-SPIONs, respectively. Binding to HA occurs significantly more than binding to all off-target surfaces for both HABP- and OPN-SPIONs ( $p < 0.05$ ).

It has been suggested that both HABP and OPN binding to HA is charge-mediated.<sup>71,72,105</sup> Therefore, HABP- and OPN-SPION binding to HA was assessed in sodium phosphate buffer at different pH levels (**Figure 2.4**). The pH levels of 7.1, 7.4, and 7.8 were selected because they may be physiologically relevant; pH levels in this range can be detected close to plaques in atherosclerotic disease.<sup>106</sup>

The different pH levels tested do not significantly impact HABP- or OPN-SPION binding to HA in terms of binding quantity; however, higher pH levels appear to lead to more variability in binding strength of SPIONs to HA. For example, for 50mg of HA, the standard deviations across runs at pH 7.1 are 2.05 and 11.96 for HABP- and OPN-SPIONs, respectively. At pH 7.4, those standard deviations are 17.14 and 28.69 respectively, and at pH 7.8, they are 21.35 and 36.60, respectively.

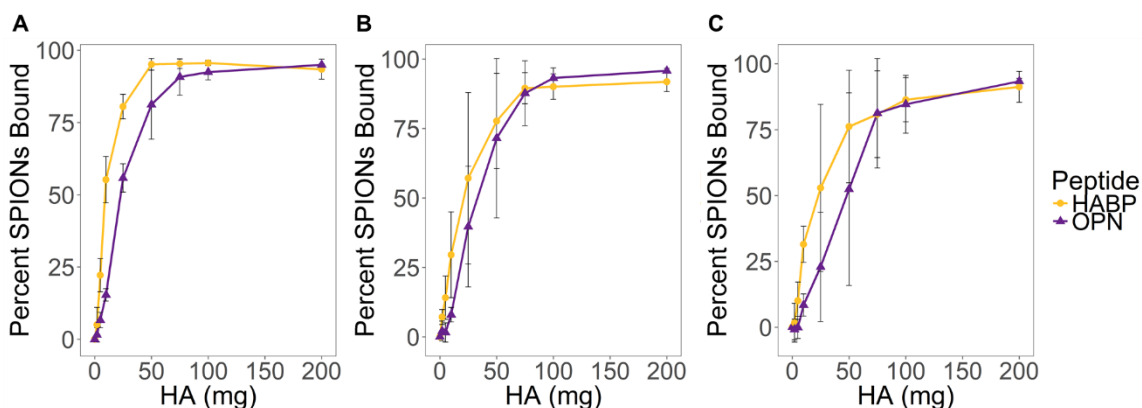


**Figure 2.4:** Quantification of the assessment of the impact of pH on SPION binding to HA in sodium phosphate buffer. Different pH values tested were: **(A)** 7.1, **(B)** 7.4, and **(C)** 7.8. Set-up for these experiments is equivalent to the set-up for results shown in Figure 2.3, (A) and (B). Error bars are standard deviation;  $n = 3$ .

### *SPION binding to Serum Proteins*

Like most if not all other nanoparticles, these functionalized SPIONs are expected to show binding to serum proteins. To assess the interactions of functionalized SPIONs with serum proteins, PEG-SPIONs as well as HABP-SPIONs and OPN-SPIONs were incubated with a 50% fetal bovine serum solution for 24 hours, and compared with SPIONs incubated in DI water to observe differences in apparent diameter that would indicate association with serum proteins (**Figure 2.5**). For these experiments, PEG-SPIONs were tested in addition to HA-targeted SPIONs in order to evaluate whether the effects shown were due specifically to the presence of the peptides. Results indicate that HABP-, OPN-, and PEG-SPIONs all associate with serum proteins immediately upon incubation. Samples develop an apparent protein corona as soon as serum is added to the nanoparticle solution.

This corona does not significantly alter in size ( $p > 0.05$ ) over 24 hours in any case.

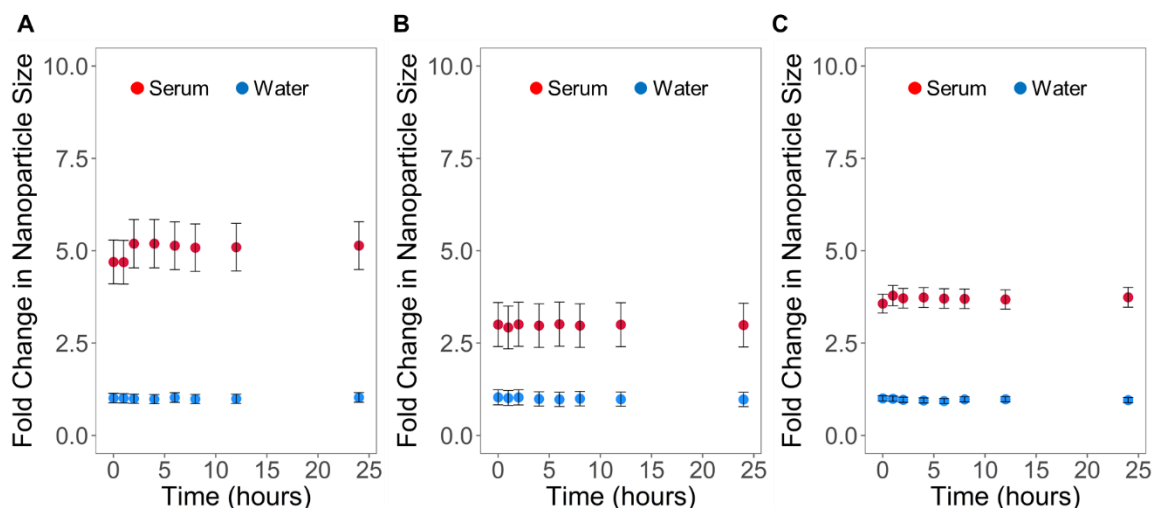


**Figure 2.5:** Fold change in nanoparticle size over time in a 50% serum solution. **(A)** HABP-SPIONs, **(B)** OPN-SPIONs, and **(C)** PEG-SPIONs were all tested under identical conditions. Both targeted (HABP- and OPN-SPIONs) and non-targeted (PEG-SPIONs) bind to proteins in serum, as evidenced by changes in effective particle diameter upon exposure to 50% serum. The protein corona that developed around all 3 functionalized SPIONs tested did not appear to alter significantly over the course of a 24-hour incubation. HABP-SPIONs appear to accumulate the largest protein corona, while OPN-SPIONs have the smallest. Despite the intended anti-biofouling function of PEG, PEG-SPIONs do still appear to accumulate a protein corona in 50% serum. Error bars are standard deviation;  $n = 3$ .

However, there are observed differences in the size of the associated protein corona depending on the SPION coating. HABP-SPIONs exhibit the largest effective diameter in 50% serum (4.64 – 5.28x the diameter in water). OPN-SPIONs have the smallest effective diameter in 50% serum (2.88 – 3.09x the diameter in water). PEG-SPIONs also demonstrate a substantial alteration in effective diameter in 50% serum (3.55 – 3.98x the diameter in water).

To better understand the protein corona of HABP-, OPN-, and PEG-SPIONs, several follow-up experiments were performed. Firstly, the formation of the protein corona in solutions of different pH was assessed (**Figure 2.6**). For these experiments, the pH of a 50% serum solution was altered over a broad range (pH 6-9), and functionalized SPIONs were added to each solution. The effective diameters of each SPION sample were analyzed by DLS. Diameters were normalized to the effective diameter of that particular functionalized SPION at a pH of 7.4, i.e. the pH of unaltered 50% serum solution. Altering the pH of the 50% serum solution does not appear to significantly impact the effective diameter of SPION samples ( $p > 0.05$ ), although average diameters shifted non-significantly with changes in pH.

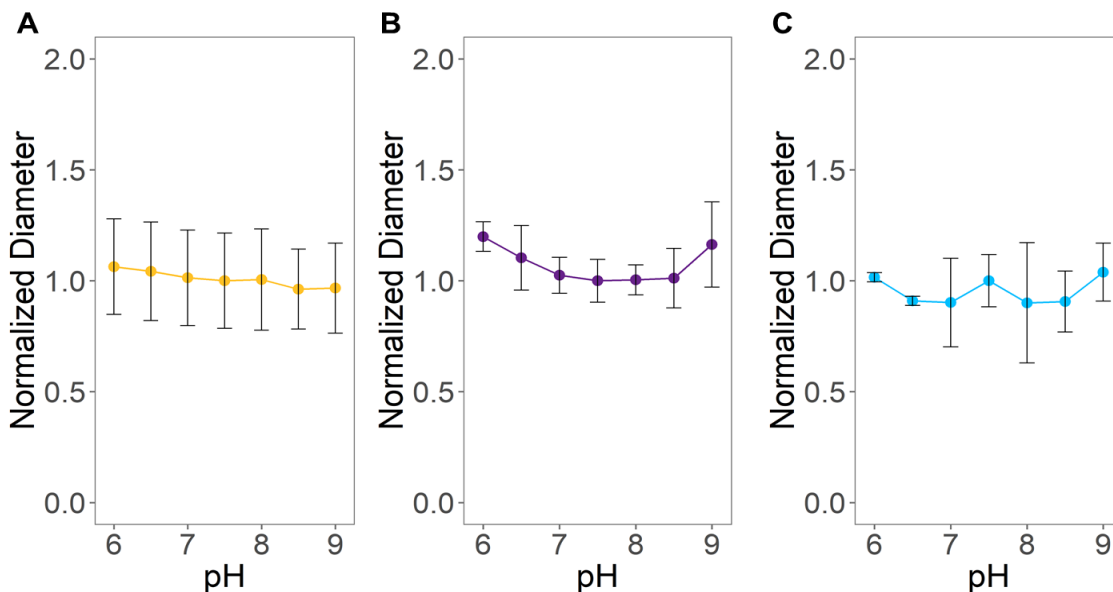


**Figure 2.6:** Assessment of **(A)** HABP-SPION, **(B)** OPN-SPION, and **(C)** PEG-SPION effective diameter in 50% serum at different pH values. All measurements were normalized to the diameter of particles in 50% serum at pH 7.4. Error bars are standard deviation,  $n = 3$ .

Subsequently, SPIONs were incubated for different amounts of time (0 minutes, 30 minutes, and 2 hours) with 50% serum and subjected to 3 wash steps via centrifugation (**Figure 2.7**). These times were selected for their clinical relevance; patients may be administered a contrast agent some time prior to clinical MR, but that time does not typically exceed 2 hours.<sup>107,108</sup> DI water was chosen as a diluent and resuspension agent in these studies because the presence of salt can screen the repulsion between nanoparticles and induce aggregation;<sup>101</sup> for these studies, it was important to limit aggregation as much as possible during resuspension, in order to obtain an accurate assessment of the final number of proteins per particle after all wash steps.

Proteins still associated with the nanoparticles after 3 washes are considered to be tightly associated (i.e., part of a “hard” corona), while those that were removed with wash steps are considered to be more loosely associated (i.e., part of a “soft” corona). Samples were taken after each wash, and the BCA assay was used to determine the amount of protein that remained associated with the particles. In all cases, the amount of associated protein is significantly reduced ( $p < 0.05$ , reduction by at least 10.78x with no incubation, at least 3.26x with 30 minutes of incubation, and at least 2.82x with 2 hours of incubation) after just one wash, with additional subsequent reductions observed across all experiments.

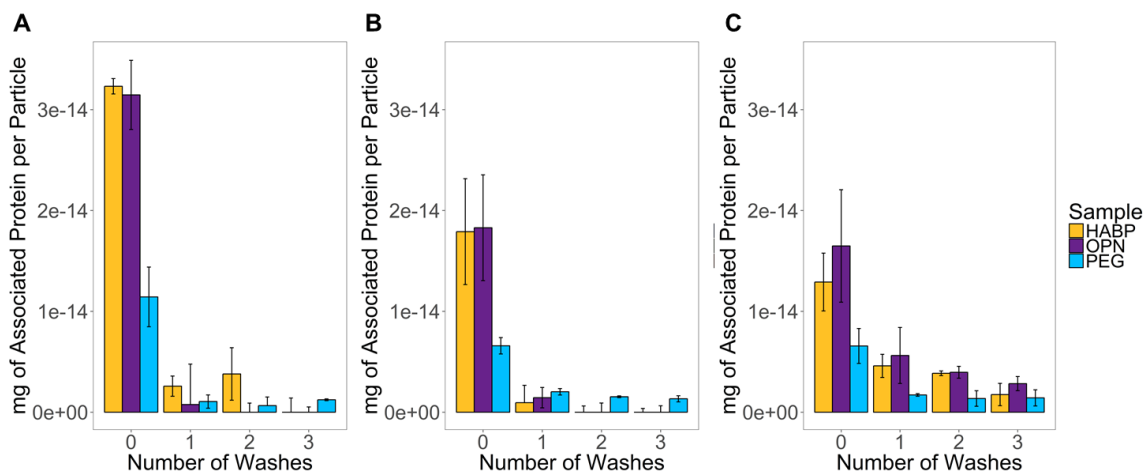


**Figure 2.7:** Soft and hard protein corona measured as mg of associated protein per particle after incubation in a 50% serum solution for (A) 0 minutes, (B) 30 minutes, and (C) 2 hours, followed by 3 wash steps via centrifugation and resuspension in DI water. Protein associated with the particles with no wash steps is considered to be part of the soft corona; protein associated with the particles after 3 washes is considered to be part of the hard corona. Error bars are standard deviation; n=3.

After 3 washes, PEGylated SPION samples that have been incubated in 50% serum for 0 or 30 minutes show increased protein in comparison to HABP- and OPN-SPIONs (for no incubation in comparison to OPN-SPIONs, and 30 minutes' incubation with both HABP- and OPN-SPIONs, this difference is significant, with  $p < 0.05$ ).

As might be expected, samples that were incubated for 2 hours show an increased level of protein in the hard corona in comparison to samples that were incubated for 0 and 30 minutes (**Figure 2.7C**). There are statistically significant ( $p < 0.05$ ) differences in the amount of protein per particle left after 3 washes for HABP- as well as OPN-SPIONs that had been incubated for 0 and 30 minutes in comparison

to those that had been incubated for 2 hours. However, the amount of protein in the hard corona for PEGylated samples does not change significantly ( $p > 0.05$ ).

The protein corona of HABP-, OPN-, and PEG-SPIONs after 3 washes was additionally qualitatively examined by SDS-PAGE gel electrophoresis followed by silver nitrate staining (**Figure 2.8**). These results can be compared to samples that had not been incubated with serum (**Figure 2.8A**). The darkness of the banding of the PEGylated SPION samples (rightmost well of each gel in **Figure 2.8 B, C, and D**) in comparison to all other samples reflects the increased number of PEGylated SPIONs that were successfully pelleted with each wash step. Qualitatively, PEGylated SPIONs formed a pellet more readily than HABP- and OPN-SPIONs upon centrifugation, and were more difficult to redisperse in water with each wash. This is likely the result of some degree of hydrophobic interactions between PEG chains, which are known to have some hydrophobic character.<sup>109</sup>

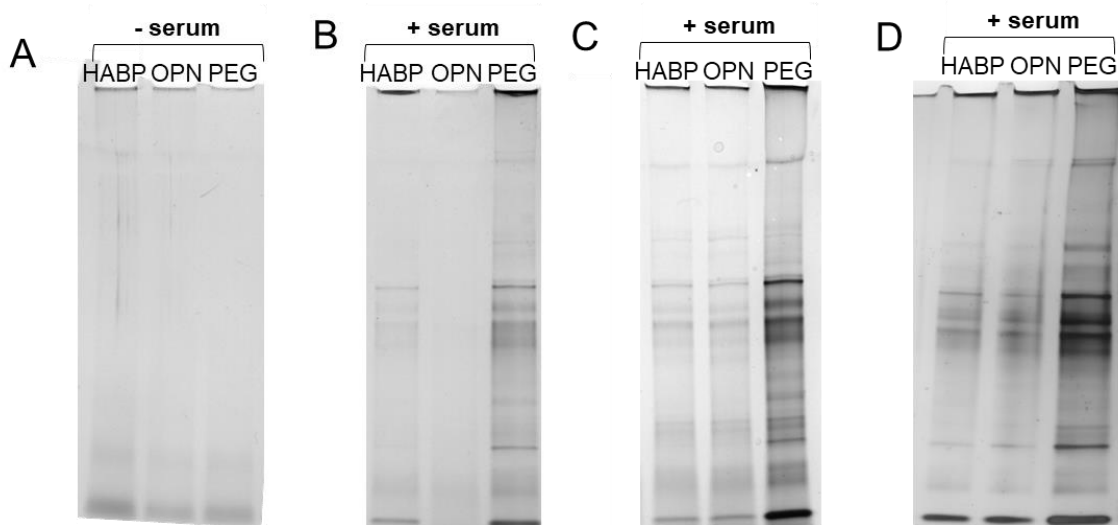


**Figure 2.8:** SDS-PAGE gels stained with silver nitrate. **(A)** Samples (HABP-, OPN-, and PEG-SPIONs, respectively) that were not incubated with serum. Wells in **(B)**, **(C)**, and **(D)** are samples (HABP-, OPN-, and PEG-SPIONs in each well, respectively) that were incubated with serum, washed 3x with water by centrifugation, and then mixed with an SDS-based running buffer and boiled to denature any protein remaining attached to the particles. Differences between wells reflect differences in which proteins may have preferentially adsorbed to different surface functionalizations; differences between gels reflect potential differences in the hard protein corona with longer incubations times. Samples were incubated with serum for: **(B)** 0 minutes, **(C)** 30 minutes, and **(D)** 2 hours prior to beginning the wash steps.

Beyond this, it is possible to observe some differences between preferentially adsorbed proteins to HABP-, OPN-, and PEGylated SPIONs, both within a single gel, and between gels. These results will be further analyzed in the Discussion (below).

### *In Vitro Binding Tests in Serum*

Finally, binding of HABP-, OPN-, and PEG-SPIONs both to HA as well as off-target surfaces was evaluated in 50% serum (**Figure 2.9**). Despite the fact that HABP- and OPN-SPIONs exhibit binding to serum proteins, they still demonstrate targeted binding to HA. Binding to HA occurred at a rate 5.97x greater than binding to any off-target surface for HABP-SPIONs, and 4.00x greater for OPN-SPIONs. Off-target surfaces evaluated include: cholesterol, collagen, fibrin, and fibrinogen. HUVECs were not tested in the experiments due to concerns that a rapid increase in environmental serum concentrations would impact membrane transport of the cells due to a rapid change in environmental osmolarity.<sup>110,111</sup> For these studies, PEG-SPIONs as well as CA-SPIONs were evaluated as negative controls to ensure that any binding trends observed in the targeted SPIONs were due to the presence of the peptide, and not merely due to the presence of a highly negative zeta potential.

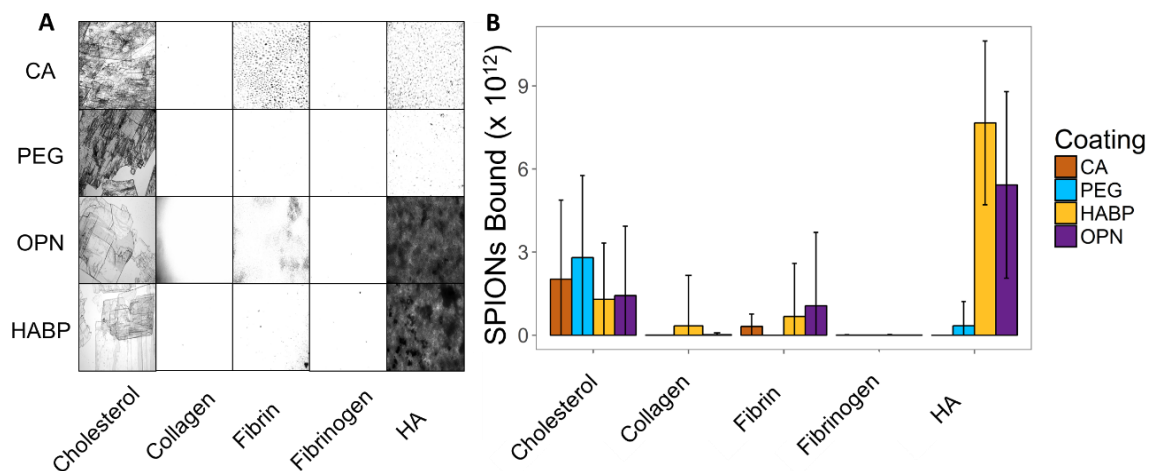


**Figure 2.9:** (A) Images taken at 20x of Prussian-Blue stained SPIONs bound to different surfaces to observe specific vs. non-specific binding. (B) Quantification of multiple runs of binding assays ( $n = 3$ ) demonstrate that both HABP- and OPN-SPIONs bind at significantly higher rates to HA than other biologically relevant surfaces, while PEG-SPIONs do not bind significantly to HA. PEG-SPIONs exhibit significant off-target binding to cholesterol, potentially due to the hydrophobic nature of the cholesterol surface.

Because HA needs to be coated on a fibrin layer to successfully stick to the plates, and because both HABP- and OPN-SPIONs exhibit some off-target binding to fibrin, it is likely that some of the particles in the HA wells are bound to fibrin rather than HA. However, the observed binding results for fibrin occur when the particles were interacting directly with an unaltered fibrin surface, not with a fibrin surface that has been blocked by a crystalline HA layer. Therefore, the vast majority of observed binding to HA is likely to the HA itself, with a small contribution from the underlying fibrin layer.

One notable observation of the results in **Figure 2.9B** in comparison to earlier

binding studies (**Figure 2C**) is that the variability of targeted and non-targeted SPION binding in serum appears to be much greater than the variability in sodium phosphate buffer. For example, in serum, between  $0 - 3.43 \times 10^{12}$  HABP-SPIONs bind to fibrin; in sodium phosphate buffer, that range is  $0.62 \times 10^{12} - 1.33 \times 10^{12}$ . In serum, between  $0 - 4.27 \times 10^{12}$  OPN-SPIONs bind to fibrin; in sodium phosphate buffer, that range is  $1.22 \times 10^{12} - 1.46 \times 10^{12}$ . This is perhaps unsurprising. However, even with this variability, binding of HABP- and OPN-SPIONs to HA is still significantly greater than off-target binding ( $p < 0.05$ ).

## **2.4 Discussion**

Functionalized SPIONs have successfully been fabricated using the scheme illustrated in **Figure 2.1**. The  $\sim 10\text{nm}$  SPION core size, as confirmed by TEM (**Figure 2.2**) was selected to reflect the size of SPIONs that are often developed for MR applications in the literature.<sup>38,112,113</sup> SPIONs may be grouped into three categories based on their size: (1) standard SPIONs (5-180nm), (2) ultrasmall SPIONs (10-50nm), and (3) very small SPIONs ( $<10\text{nm}$ ).<sup>114</sup> The 10nm core size was chosen because the most commonly used MRI agents are ultrasmall SPIONs; subsequent to all coating steps described, SPIONs with a core size of  $\sim 10\text{nm}$  remain categorized as “ultrasmall.”<sup>112</sup>

The ligand exchange with citric acid prior to PEGylation is one of a wide variety of

PEGylation methods demonstrated in the literature. This method was selected in part because the CA-SPION cores are themselves soluble in water, making characterization, storage, and subsequent PEGylation more facile than other PEGylation methods which largely rely on coating of hydrophobic, oleic-acid coated cores.

Coating with PEG was performed to aid in making these SPIONs “stealth” nanoparticles by preventing protein deposition and therefore recognition by the immune system.<sup>89–91</sup> Additionally, previous studies have indicated that polymer coatings such as PEG or dextran can help increase the circulation time of SPIONs after injection.<sup>115,116</sup> However, claims that PEG prevents the deposition of all serum proteins have been refuted or confounded by many recent studies showing that proteins present in blood or serum bind to PEGylated nanoparticles.<sup>92,93</sup> Nevertheless, PEG was used in part to also allow the addition of a specific binding site for peptides.

Two peptides were selected for binding studies to HA, as they are expected to have widely different properties. Ribosome-derived HABP is a synthetic peptide that, in addition to binding to HA, may show some binding to metallic surfaces.<sup>117</sup> OPN is a highly-phosphorylated peptide that has been derived from osteopontin, a bone-binding sialoprotein that plays roles in biomineralization, bone remodeling, and various immune functions.<sup>118–120</sup> Although both of these peptides bind to HA, characterization of these peptides *in silico* via an online tool from GenScript yields

the results summarized in **Table 2.2**, which indicate that the peptides have vastly different properties and are likely to behave very differently in solution. In particular, the acid/base nature, charge, and hydrophobicity of the peptides varies substantially. These differences in properties have notable impacts even in *in vitro* binding studies (**Figure 2.3**). Although both HABP- and OPN-SPIONs demonstrated binding to HA (**Figure 2.3B**), the increased binding of HABP-SPIONs at lower quantities of HA reflects a difference that likely reflects a difference in HABP and OPN interaction with HA. Importantly, however, both HABP- and OPN-SPIONs bind to small quantities (< 200mg) of HA. This was of particular concern, as this is a relevant quantity of HA in early cardiovascular disease.<sup>61</sup>

The differences in effective diameter observed upon exposure of functionalized SPIONs to serum proteins (**Figure 2.5**) are likely due to a combination of factors. HABP-SPIONs show the largest increase in effective diameter, indicating either that larger proteins are preferentially binding, more proteins are bound, more aggregation is occurring, or likely, some combination of all three factors. This may, in part, be due to the synthetic nature of the peptide, which, as its sequence was determined by ribosome display, is unlikely to have biological analogs. On the other hand, OPN-SPIONs showed the smallest increase in diameter, potentially indicating that fewer serum proteins tend to associate with these particles, or that less aggregation occurs. Despite the fact that PEG is intended to prevent

deposition of serum proteins, PEG-SPIONs without the addition of either peptide also demonstrate a substantial alteration in effective diameter in 50% serum. This indicates that serum proteins do adhere to or associate with PEGylated nanoparticles, as has been previously reported by other groups.<sup>92,93</sup> The vast majority of these interactions with serum protein are likely to be non-specific, as partially indicated by the fact that altering the pH does not significantly change the effective diameter of the SPIONs in serum (**Figure 2.6**). If the observable protein corona were the result of specific and strong binding interactions, it is likely that such large alterations in pH would disrupt these interactions, and a change in the size of the protein corona or the resulting zeta potential would be observed.

The fact that the protein corona is mostly nonspecific and does not substantially alter in size over the course of 24 hours in **Figure 2.5** does not necessarily indicate that it remains constant. It is well accepted that the nanoparticle corona is made up of a “hard” corona that consists of tightly bound proteins that and is unlikely to change significantly in composition over time, and a “soft” corona that consists of proteins that are associated with low affinity that may readily adsorb and desorb over time. **Figure 2.7** aims to visualize some of these changes. Changes observed across incubation times (0 hours, 30 minutes, and 2 hours) are reflective of alterations in the hard vs. soft protein corona. These results corroborate some of the findings from **Figure 2.5**; specifically, that the association of serum proteins with all SPIONs occurs immediately upon mixing of the nanoparticles with serum. Additionally, these results support previous literature, demonstrating that

PEGylated particles do show reduced protein association in comparison to SPIONs with attached peptide prior to any performed washes. However, while there may be less of a “soft” protein corona associated with PEGylated particles, there is an increased protein presence in the “hard” protein corona; barely any protein remains associated with HABP- or OPN-SPIONs after 3 washes for samples that have been incubated for 0 or 30 minutes. Ultimately, the difference between 2 hour and 0 hour/30 minute samples for HABP- and OPN-SPIONs does indicate an increased quantity of protein per SPION with longer incubation. This may suggest a decreased targeting efficiency in peptide-coated SPIONs upon longer incubation with serum.

Qualitative visualization of some of these results in **Figure 2.8** shows similar trends, in addition to some differences observed between samples in terms of the types of proteins bound to the SPIONs. The differences within a gel are to be expected; many previous studies have confirmed that different surface functionalizations yield an ultimately different protein corona composition.<sup>121,122</sup> The differences between gels would confirm previous results in the literature, which have found that, with incubation, loosely associated proteins close to the nanoparticle may be replaced by different proteins that more preferentially associate with a given surface functionalization.<sup>88</sup> The types of protein associated with each particle were not further assessed, as these experiments were performed in 50% fetal bovine serum, and specific protein analysis may not be comparable or relevant for medical applications in humans. Additionally, it has been shown that factors such as shear

stress (which would be experienced by SPIONs in circulation) contribute to observed differences in the protein corona formed on nanoparticles.<sup>123</sup> Because of this, and the matrix chosen, it was determined that assessing the exact composition of the corona would not yield medically relevant results for these particles. Further studies would be needed to assess targeted binding both in human serum as well as under flow conditions; yet even these studies could not fully recapitulate the *in vivo* environment.

Finally, despite the presence of 50% serum, HABP- and OPN-SPIONs do still bind to HA significantly more than they bind to any off-target surfaces. For these studies (**Figure 2.9**), CA-SPIONs in addition to PEG-SPIONs were examined as a control. Because CA-SPIONs, like HABP- and OPN-SPIONs, carry a highly negative surface charge, the results in **Figure 2.9** would indicate that it is not merely the presence of a negative surface charge that causes the targeted binding of HABP- and OPN-SPIONs to HA, although charge may certainly play a role.

The apparent off-target binding of PEG-SPIONs to cholesterol was unexpected, but is evident in microscopic images as well as the quantitative data. It is hypothesized that this binding may be due to the hydrophobic and crystalline nature of the deposited cholesterol. Similar results have been reported previously for cyclodextrin-coated nanoparticles.<sup>124,125</sup> For diseases such as atherosclerosis, it may be worth further examining the interaction between PEGylated nanoparticles and cholesterol in the future.

## Chapter 3: Optimization of SPION Binding Properties and MR Signal

### 3.1 Introduction

As described in Chapters 1 and 2, SPIONs are commonly used as contrast agents for clinical MRI.<sup>126–128</sup> SPIONs hold specific advantages over widely-used gadolinium-based MR contrast agents in that each nanoparticle contains thousands of iron atoms and approaches saturation magnetization under a magnetic field typical for MR, meaning that each nanocrystal can generate signal contrast several orders of magnitude higher than gadolinium chelates.<sup>129</sup> Additionally, SPIONs have demonstrably lower toxicity *in vivo* than gadolinium-based contrast agents.<sup>44,45,47,90,98</sup> These two features make SPIONs well-suited in particular for early detection or diagnosis of diseases ranging from cancer to atherosclerosis, among many others.

One challenge of using molecular-targeted, or more specifically, HA-targeted SPIONs as a method to detect early calcium deposits in CAVD is that, like many early-disease targets, these calcium deposits are typically present in small quantities. Detecting such small quantities of HA, even with the benefit of SPION-enhanced contrast, is challenging in MRI. It is therefore desirable and necessary to synthesize SPIONs with substantial signal enhancement in order to improve the sensitivity of these diagnostic methods. This can be achieved in one of two ways: 1) optimizing targeted SPION binding to HA, to ensure that as many SPIONs as possible can bind to the target, and/or 2) optimizing the targeted SPION makeup

to enhance MR signal of the particles themselves. However, few previous studies have comprehensively examined either approach to signal optimization.

The first approach (optimizing targeted SPION binding to HA to ensure that as many SPIONs as possible can bind to the target) would rely primarily on changes to the peptide coating of the SPIONs. As HA-SPIONs and OPN-SPIONs did demonstrate different binding properties (notably, **Figure 2.9B**, although the difference is not statistically significant, and **Figure 2.3B**, where the differences for small quantities of HA are statistically significant), it was hypothesized that altering the targeted number of peptides per SPION may also impact the number of SPIONs bound to a given quantity of HA. It was also hypothesized that combining HABP and OPN onto a single SPION, and altering the ratio of HABP:OPN peptides on a single SPION, may impact the number of SPIONs bound to HA as well. These hypotheses were tested using methods described below.

The second approach (optimizing the targeted SPION makeup to enhance MR signal of the particles themselves) would rely primarily on changes to the PEG coating and SPION core size that may yield corresponding changes in the MR signal of the SPIONs. SPIONs create contrast in MR imaging by affecting the relaxation properties of nearby protons; namely  $T_1$  (spin-lattice) and  $T_2$  (spin-spin).<sup>130</sup> The corresponding relaxivities  $r_1$  and  $r_2$ , i.e., the change in relaxation rates of water protons with respect to particle concentration are in part determined by the translational diffusion of the water molecules in the inhomogeneous magnetic

field caused by the SPIONs.<sup>129</sup> Although SPIONs impact both  $r_1$  as well as  $r_2$  relaxivities, they are primarily used as  $T_2$  contrast agents because of their larger  $r_2$  relaxivities. Two parameters of the SPIONs and their chemical coatings are known to impact the MR signal generated by the particles: (1) iron oxide core (size and material), and (2) the polymer coating surrounding the SPION core, which includes coating density (i.e. polymer chains per  $\text{nm}^2$ ), thickness (polymer chain length), and chemical composition.

Some prior work has explored the former aspect of SPION contrast agents. It is known that for a fixed total amount of iron in the core,  $r_2$  relaxivity of SPIONs increases with the magnetization and the total core size (i.e. iron oxide plus other elements that may be added to the core).<sup>131,132</sup> Altering the magnetization of SPIONs by doping the iron oxide with other magnetic elements (e.g. nickel, cobalt, and manganese) leads to enhancement of the measured relaxivities of the SPIONs.<sup>132–134</sup>

However, the effect of changes in polymer coating in terms of density, thickness, and chemical composition on the resulting MR properties of the SPIONS not been well-characterized to date. Of the limited prior studies, none have controlled for or measured coating density, which is thought to have a direct effect on the resultant relaxivities of the agent.<sup>98,135</sup> The relevance of understanding how altering the SPION core coating may impact MR signal is in part due to the fact that the strength of the magnetic field surrounding the SPION core diminishes rapidly with

distance; thus, the strongest part of the magnetic field surrounding the SPION often falls within the polymer coating.<sup>135,136</sup> SPION functionalization using different coating schemes, particularly in terms of method of chemical attachment of the coating to the core and polymer chain length, may affect their MR properties even if the coating density remains constant. The aim of the MR studies presented in this chapter is to determine the effect of different methods of chemical attachment of a polymer, polymer chain length, and polymer coating density on the MR relaxivities of SPIONs, thereby contributing a better understanding of the interaction of these parameters and the efficacy of the designed agent. These results will aid in better optimization of SPION MR properties in the future, with the aim of improving SPION contrast agents intended for clinical imaging.

The results of the experiments performed in this aim will aid in the signal enhancement and/or optimization of HA-targeted SPIONs for use in early detection of CAVD. These results will aid in the selection of an optimized coating schema, from the standpoint of both the peptide and polymer coatings.

### ***3.2 Materials and Methods***

A number of SPIONs were synthesized to be physiochemically distinct in terms of their core size, PEG chain length, and the method of PEG attachment to the SPION core. SPION properties including size, zeta potential, and coating density of the

attached PEG were evaluated. The MR relaxivities of these SPIONs were subsequently measured and compared.

### *Materials*

Materials previously discussed in Chapter 2 were obtained from the same sources. NH<sub>2</sub>-PEG and 1,2-Distearoyl-sn-glycero-3-phosphoethanolamine (DSPE) – PEG reagents were obtained from Nanocs (Boston, Massachusetts); phosphine oxide (PO)-PEG reagents were obtained from JenKem Technology (Plano, Texas). Cryogenic vials for sample measurements were obtained from Corning (Corning, New York).

### *Altering the number of peptides or the peptide ratio per SPION*

Iodoacetyl-PEG-SPIONs are fabricated as previously described in Chapter 1. To alter the number of peptides bound per SPION, HABP or OPN peptides are added to iodoacetyl-PEG-SPION solutions in appropriate concentrations to target the addition of 5, 10, 25, 50, and 100 peptide residues per SPION. To alter the peptide ratio per SPION, solutions of combined HABP and OPN are added to iodoacetyl-PEG SPION solutions in appropriate concentrations to target the addition of a 1:2, 2:1, and 1:1 ratio of HABP:OPN peptide residues, all targeting the addition of 25 total peptides. Peptide addition reactions are allowed to run overnight at 4 °C, and

conjugated particles are purified from excess peptide by dialysis against deionized water at 4°C. *In vitro* binding tests in sodium phosphate buffer are performed on these samples with powdered HA from Sigma, as previously described in Chapter 2. Statistical analysis and graphing of the results were performed in R.

### *PEGylation*

PEGylation of OA-SPIONs was accomplished via one of three protocols similar to the majority of those that have been previously used to functionalize SPIONs (see below).

1) *PO-PEGylation*.<sup>137</sup> OA-SPIONs are dissolved in 1mL of n-heptane or 1mL of 1,2 dichlorobenzene while PO-PEG (molecular weight 1, 2, or 5 kDa) is dissolved in 1mL of ethanol. Sufficient PEG is used to target a coating density of 0.70nm<sup>-2</sup>. The mixture is heated (70°C) and left stirring for at least 5 hours. PO-PEG coated nanoparticles (PO-PEG-SPIONs) are precipitated in n-hexane and collected on a magnet. They are then redispersed in ethanol before dispersing in DI water and remaining ethanol is allowed to evaporate. Excess PEG is removed by dialysis for at least 48 hours against DI water.

2) *NH<sub>2</sub>-PEGylation*.<sup>97,98</sup> A ligand exchange is performed to replace the oleic acid with citric acid. Oleic acid-coated nanoparticles and citric acid are dissolved in a 1:1 mixture of dichlorobenzene and N,N-dimethylformamide. The mixture is heated

to 100°C and left stirring for 24 hours. Citric acid coated nanoparticles (CA-SPIONs) are precipitated in diethyl ether and washed with acetone and diethyl ether before drying in a vacuum oven.

For PEGylation, CA-SPIONs are dissolved in pH 9 sodium phosphate buffer and filtered using syringe PTFE filters (0.2 µm). NH<sub>2</sub>-PEG (molecular weight 1, 2, or 5 kDa) is added to the CA-SPIONs in quantities sufficient to target a coating density of 0.70nm<sup>-2</sup>. 1-Ethyl-3-(3-dimethylaminopropyl)carbodiimide (EDC) and N-hydroxysuccinimide (NHS) are added in molar excess to the solution, which is allowed to mix overnight at room temperature. Excess PEG is removed by dialysis for at least 48 hours against DI water.

3) *DSPE-PEGylation*:<sup>135</sup> OA-SPIONs are dissolved in chloroform. A corresponding polymer solution is created through the dissolution of DSPE-PEG (molecular weight 1, 2, or 5 kDa) in a 1:1 mixture of chloroform and acetonitrile in quantities sufficient to target a coating density of 0.70nm<sup>-2</sup>. The two solutions are mixed for 15 minutes while 10mL of water and two washed marbles are warmed to 70°C. A rotary evaporator is used to remove the chloroform and acetonitrile, creating a thin film of particles and PEG on a roundbottom flask. The water and marbles are then added to the flask and swirled vigorously for 15 minutes until the film is dissolved. Once mixed, the solution is filtered through a 0.2µm syringe filter. DSPE-PEGylated nanoparticles are separated from DSPE-PEG micelles or liposomes by pulling down onto a magnet. The isolated DSPE-SPIONs are redispersed in water.

### *Dynamic Light Scattering, Zeta Potential, and Thermogravimetric Analysis*

The effective diameter of all SPIONs produced is measured via dynamic light scattering (DLS) in water. Samples are diluted 10x in water and measured on a 90Plus DLS Analyzer (Brookhaven Instruments) at a 90° detection angle. Dilution was performed because previous studies have indicated that high concentrations of nanoparticles may disrupt DLS readings.<sup>138</sup> Zeta potential measurements are performed on the same samples using the same apparatus.

The density of polymer coating is measured by thermogravimetric analysis (TGA) using a Discovery TGA system (TA Instruments). Samples are lyophilized to remove all water, and at least 1mg of each sample for each run is loaded onto a TGA pan. All TGA analysis is performed under nitrogen flow. Samples are ramped to 100°C and allowed to equilibrate to remove any additional water that may have been absorbed by samples during storage. Then, samples are ramped to 650°C and allowed to equilibrate. The mass remaining at the end of this ramping step is considered to be solely comprised of the iron oxide core of the particles; these values are used to calculate the amount of PEG that was attached to the particles prior to TGA analysis, and the corresponding surface density of PEG on each sample.

### *Preparation of Samples for MR Measurements*

The iron concentration in each resulting solution containing PEGylated particles is determined using a simple absorbance assay at 510nm, based on solutions containing known quantities of iron. Solutions at different concentrations (0, 5, 25, 50, 75, and 100 ppm) are prepared by dilution in water for MR. The solutions are stored in plastic cryogenic vials, and the amount of air in each vial is minimized to eliminate signal interference from the air-water interface. All vials are embedded into Styrofoam for MR measurements.

### *MR Equipment & Experiments*

Four MR experiments were performed for each set of samples. Two experiments were designed to measure  $R_2$ , one was designed to measure  $R_2^*$ , and one was designed to measure  $R_1$ . All experiments were performed on a 3 Tesla GE HDx clinical MR imager (GE, Milwaukee, WI) equipped with 40 mT/m gradients capable of 150 mT/m/sec slew rate and an 8 channel brain phased array receiver coil for signal reception.

The first experiment, designed to measure  $R_2$ , used a two-dimensional single echo spin echo sequence with a repetition time (TR) of 2 sec and repeated independently for 11 echo times (TE) ranging from 9 ms to 125 ms ( $TE_i = 9, 14, 20, 26, 34, 42, 50, 65, 80, 102.5$  and 125 ms). Other sequence parameters were 2 mm

slice thickness, 13-15 cm field-of-view (FOV), 256×256 matrix, 2 signal averages and ±19 kHz bandwidth. With these parameters, typical signal-to-noise ratio (SNR) was 40 at the shortest TE, reducing to 10 no earlier than the fourth echo for the highest agent concentrations.

Because T2 measurements using this Hahn single echo spin echo sequence are sensitive to molecular diffusion, a second experiment was performed to measure R<sub>2</sub> using a three-dimensional multi-echo spin echo Carr-Purcell-Meiboom-Gill sequence.<sup>139–143</sup> This sequence utilized non-selective radiofrequency pulses with composite refocusing (90<sub>x</sub>-180<sub>y</sub>-90<sub>x</sub>) as well as gradient crushers that alternated in polarity in every echo and that diminished in amplitude at every pair of echoes.<sup>144</sup> Sequence parameters were 1.5 sec TR, 16 echoes evenly spaced at 7.4 ms (first echo at 7.4 ms, last echo at 118.4 ms), 2 mm slice thickness, 13-15 cm FOV, 96 (readout) × 72 (phase) × 38 (slice) matrix, 1 signal average, and ±32.8 kHz bandwidth. SNR was typically >100 at the first echo, and reducing to no less than 30 at the 4th echo for the highest agent concentration.

R<sub>1</sub> was measured using a two-dimensional single echo spin echo sequence but with a fixed echo time of 9 ms and independently repeated for 12 repetition times ranging from 100 ms to 9 sec (TR<sub>i</sub>=100, 250, 500, 750, 1000, 1366, 1750, 2500, 4000, 5500, 7000, and 9000 ms). Other parameters were identical to the single echo spin echo R<sub>2</sub> experiment except that 4 signal averages were used for the shorter TRs in order to increase SNR, except for acquisitions with TR >2.5 sec for

which only 1 signal average was used to maintain a reasonable scan time. With these parameters, SNR was between 10–30 for the three shortest TRs and >30 for the remaining TRs.

Finally  $R_2^*$  was measured using a two-dimensional multi echo gradient recalled echo sequence with a 1.5 sec TR and 8 echoes collected between 3.6 and 40 ms with a spacing of 5.3 ms. Other sequence parameters were 2 mm slice thickness, 13–15 cm FOV,  $256 \times 256$  matrix, 2 signal averages and  $\pm 32.8$  kHz bandwidth. SNR was 12 at the first echo and dropped to approximately 3 by the 4<sup>th</sup> echo at the highest agent concentration.

### *MR Analysis*

Analysis of MR signal intensities to determine sample relaxation rates was performed using custom software developed in MATLAB (version R2013b, Mathworks Inc., Waltham MA). The software performed non-linear non-negative least squares fitting of signal intensity measurements across either the echo (for T2,  $T_2^*$ ) or the repetition times (for T1), using idealized mono-exponential signal models. For T2 and  $T_2^*$  measurements, the signal model was  $s(TE_i) = s_{TE=0} e^{-TE_i R}$ , where R the corresponding  $R_2$  or  $R_2^*$  relaxation rate. For T1 measurements, the signal model was  $s(TR_i) = s_{TR=\infty} (1 - e^{-TR_i R_1})$ . In both models, the non-linear optimization routine solved for the spin density  $s_{t=\{0,\infty\}}$  and the corresponding

relaxation rate.

Signal intensities in each sample were measured using a custom software user interface (also developed in MATLAB). The software allowed all DICOM images corresponding to a single experiment (e.g., all spin echo acquisitions with a single TR and varying TE for a T2 experiment) to be loaded, and regions-of-interest (ROIs) to be placed in any source axial slice in the image volume of one acquisition. The software then propagated the ROI to the corresponding slice and location in every acquisition (e.g., the multiple TEs or multiple TRs) in the experiment, thereby producing the average signal measurement for that ROI across the corresponding independent variable. ROIs were placed at the center of each vial for each solution concentration in at least 4 different axial slices covering the vial. The fitted relaxation times were recorded into Excel and averaged over the multitude of ROIs collected for each vial. A least squares linear fit was finally used to calculate the agent relaxivity ( $r_1$ ,  $r_2$ ,  $r_2^*$ ) as the slope of a straight line corresponding to the measured relaxation rates ( $R_1$ ,  $R_2$ ,  $R_2^*$ ) vs. known iron concentration values of each vial. Standard error in the slope was also estimated from this output. Plotting of all the results was done in R (version 3.5.1) using ggplot2.

### 3.3 Results

#### *Altering the number of peptides or the peptide ratio per SPION*

SPIONs with different quantities of attached peptide (HABP and OPN) were fabricated by stoichiometrically altering the quantities of peptide added to the SPION solutions before incubation. After addition of the correct amounts of peptide to target the addition of 5, 10, 25, 50, and 100 peptides per SPION for both HABP- and OPN-SPIONs, aggregation of the 100 peptide per SPION samples was observed for HABP-SPIONs. The aggregated SPIONs were not further tested (Figure 3.1).

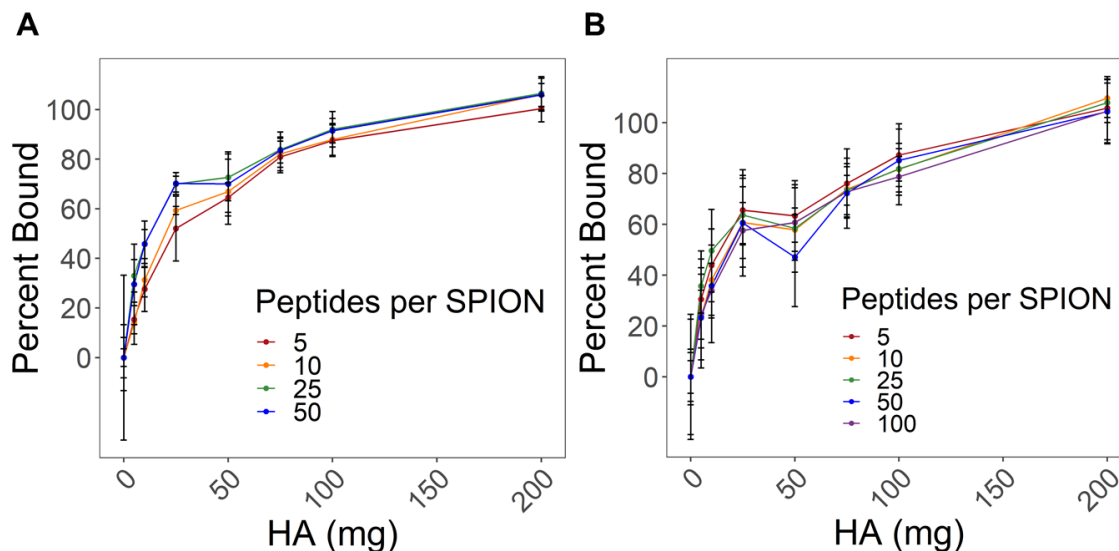


**Figure 3.1:** Assessment of the impact of functionalizing SPIONs with different quantities of peptides per SPION. Peptides per SPION are estimated based on the peptide addition reaction stoichiometry. Studies were performed using both (A) HABP-SPIONs and (B) OPN-SPIONs. 100 peptides per SPION HABP-SPIONs were not tested for binding properties because they are unstable in solution upon fabrication. Error bars are standard deviation; n = 3.

Across the different samples tested, the number of peptides per SPION did not appear to have a large effect on the percent of SPIONS that bind to a given quantity of HA. For HABP-SPIONS, increasing the number of peptides per SPION generally yielded an increased percent bound for a given quantity of HA; however, these differences are quantitatively small. The differences are only statistically significant in comparing HABP-SPIONS with 5 peptides/SPION to those with 50 peptides/SPION. For OPN-SPIONS, on the other hand, increasing the number of peptides per SPION generally yielded a decreased percent bound for a given quantity of HA. These differences are also qualitatively small. Again, the differences are only statistically significant in comparing OPN-SPIONS with 5 peptides/SPION to those with 50 peptides/SPION.

SPIONS with different ratios of attached peptide (HABP:OPN) were also fabricated by stoichiometrically altering the quantities of peptides added to the SPION solutions before incubation. All peptide solutions were mixed separately before adding this solution to the SPIONS. After addition of the correct amounts of peptide to target the addition 25 peptides per SPION with ratios of 1:1, 1:2, and 2:1 (HABP:OPN), binding to HA at different quantities was assessed (**Figure 3.2**).

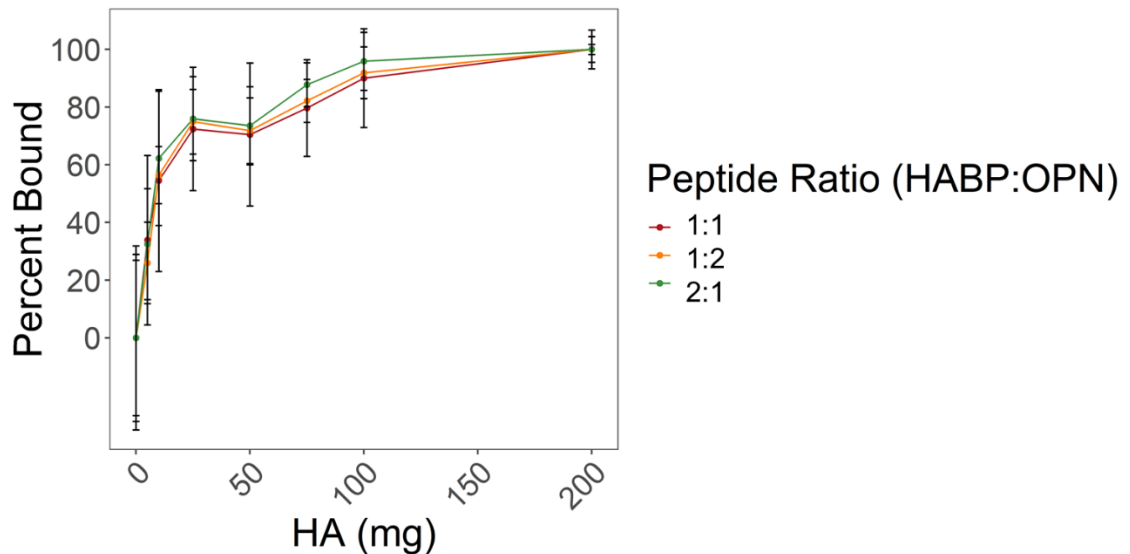


**Figure 3.2:** Assessment of impact of functionalizing SPIONs with different peptides ratios between HABP and OPN on a given SPION. Peptides per SPION are estimated based on the peptide addition reaction stoichiometry. Error bars are standard deviation; n= 3.

Across the different samples tested, the ratio of different peptides on each SPION did not appear to have a large effect on the percent of SPIONS that bind to a given quantity of HA. Differences between samples were not significant.

### *PEGylation of non-targeted SPIONs*

It was hypothesized that altering the chemical and physical properties of the SPIONs would yield alterations in the MR properties, and that these measurements could be used to identify a specific SPION makeup that would yield an optimal MR signal. In order to optimize the MR signal of SPIONs, both 4nm and 10nm SPION cores were successfully functionalized using 3 different fabrication

schemes, as shown in **Figure 3.3**. As described above, methods of fabrication included: (1) direct PEGylation via ligand exchange with PO-PEG, (2) a ligand exchange to coat particles with citric acid, followed by covalent addition of NH<sub>2</sub>-PEG via EDC/NHS chemistry, and (3) PEGylation via hydrophobic interactions between oleic acid on the SPION surface and DSPE residues on DSPE-PEG. For each method of fabrication, at least 3 different PEG chain lengths were added to different particle samples to observe the effect of polymer chain length on the resulting MR relaxivities. Tested PEG chain lengths were: (1) for PO-PEG SPIONs – 1000, 2000, and 5000 Da, (2) for NH<sub>2</sub>-PEG SPIONs – 1000, 2000, 3400, and 5000 Da, and (3) for DSPE-PEG SPIONs – 1000, 2000, 5000 Da. In total, 20 unique SPIONs were fabricated, characterized, and tested.

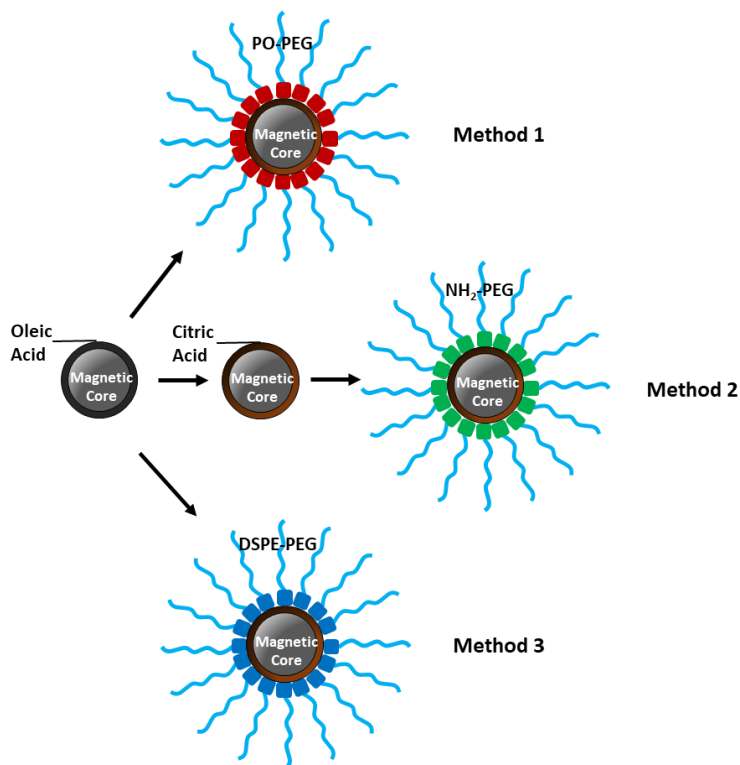


**Figure 3.3:** Schematic of particle fabrication. Oleic acid particles are coated with PEG via one of three methods: (1) direct PEGylation via ligand exchange with PO-PEG, (2) a ligand exchange to coat particles with citric acid, followed by covalent addition of NH<sub>2</sub>-PEG via EDC/NHS chemistry, or (3) PEGylation via hydrophobic association between oleic acid and DSPE residues on DSPE-PEG.

### *Dynamic Light Scattering, Zeta Potential, and Thermogravimetric Analysis*

DLS, zeta potential measurements, and TGA were used to characterize and confirm the success of SPION fabrication for each type of SPION produced (**Table 3.1**). Notably, each method of fabrication produced SPIONs with different properties in terms of effective diameter, zeta potential, and, in some cases, surface density. In PO-PEG SPIONs, nanoparticle effective diameter appears to increase as PEG chain length increases (e.g. for 4nm and 10nm PO-PEG SPIONs), as expected. These differences however were not statistically significant across multiple batches ( $p > 0.05$ ). For DSPE-PEG SPIONs (both 4 and 10nm diameter), the 5k PEG samples had a smaller effective diameter than either the 1k or the 2k PEG, although again these differences were not significant ( $p > 0.05$ ). This trend was also observed for 4nm NH<sub>2</sub>-PEG SPIONs, with 3.4k NH<sub>2</sub>-PEG SPIONs being significantly larger ( $p < 0.05$ ) than 1k, 2k, and 5k NH<sub>2</sub>-PEG SPIONs. For 10nm NH<sub>2</sub>-PEG SPIONs, this did not appear to be the case; 5k NH<sub>2</sub>-PEG SPIONs were significantly larger than 1k, 2k, and 3.4k NH<sub>2</sub>-PEG SPIONs. For both PO-PEG and NH<sub>2</sub>-PEG SPIONs, the effective diameters of the 4nm samples were significantly smaller ( $p < 0.05$ ) than the equivalent 10nm samples. For DSPE-PEG SPIONs, this was not the case. Finally, it can be observed for all samples that for a given core size and PEG chain length, the effective diameter observed between different PEGylation methods was such that NH<sub>2</sub>-PEG SPIONs < PO-PEG SPIONs < DSPE-PEG SPIONs. These differences vary in statistical significance, but this trend was evident across all samples.

Diameter (nm)	PEGylation Method	PEG Size (kDa)	Effective Diameter (nm)	Zeta Potential (mV)	Surface Density (PEG chains/nm <sup>2</sup> )
4	PO-PEG (Method 1)	1000	18.66 ± 4.14	-14.75 ± 1.58	0.56 ± 0.06
		2000	22.67 ± 3.21	-5.63 ± 6.13	0.82 ± 0.09
		5000	22.86 ± 2.54	-1.62 ± 4.21	0.93 ± 0.23
	NH <sub>2</sub> -PEG (Method 2)	1000	14.79 ± 3.74	-19.46 ± 1.71	0.68 ± 0.13
		2000	18.04 ± 4.24	-15.89 ± 1.11	0.93 ± 0.04
		3400	38.46 ± 6.16	-10.85 ± 1.29	0.87 ± 0.06
		5000	20.03 ± 4.42	-8.93 ± 1.21	0.86 ± 0.15
	DSPE-PEG (Method 3)	1000	64.24 ± 16.19	-23.55 ± 13.85	0.70 ± 0.05
		2000	82.40 ± 26.49	-18.36 ± 23.57	0.82 ± 0.05
5000		52.98 ± 11.54	22.17 ± 19.41	1.13 ± 0.11	
10	PO-PEG (Method 1)	1000	40.69 ± 5.42	-6.30 ± 1.29	0.41 ± 0.10
		2000	42.71 ± 7.45	-13.35 ± 3.16	0.67 ± 0.13
		5000	45.93 ± 5.47	-8.94 ± 0.89	0.66 ± 0.18
	NH <sub>2</sub> -PEG (Method 2)	1000	30.22 ± 5.46	-22.79 ± 2.75	0.35 ± 0.31
		2000	27.33 ± 5.17	-13.79 ± 1.84	0.62 ± 0.08
		3400	31.12 ± 5.57	-20.67 ± 1.39	0.67 ± 0.03
		5000	41.21 ± 6.35	-13.54 ± 1.65	0.60 ± 0.14
	DSPE-PEG (Method 3)	1000	58.07 ± 15.21	-31.14 ± 31.40	0.69 ± 0.00
		2000	75.45 ± 28.67	-16.10 ± 33.98	0.69 ± 0.01
		5000	55.49 ± 11.70	-3.61 ± 16.48	0.77 ± 0.27

**Table 3.1:** Summary of DLS, zeta potential, and TGA data for all particles produced as part of testing different PEGylation methods, PEG chain lengths, and SPION diameters for their impact to MR signal. Effective diameter was measured using DLS, zeta potential was measured on the same machine, and surface density was calculated from TGA results. Results are represented as mean ± standard deviation, n = 3.

Zeta potential results also reflected interesting trends. Generally speaking, zeta potential decreased with increasing PEG chain length (for 4nm PO-PEG SPIONs, 4nm NH<sub>2</sub>-PEG SPIONs, and 10nm DSPE-PEG SPIONs). For 4nm DSPE-PEG SPIONs, zeta potential results showed high error and no observable trend. For 10nm PO-PEG SPIONs, zeta potential results showed low error, but again, no definitive trend. And for 10nm NH<sub>2</sub>-PEG SPIONs, zeta potential appeared to be

bimodal, with 1k and 3.4k samples having more similar zeta potentials, which were different than the similar zeta potentials shared by 2k and 5k samples. Given the same PEG chain length and PEGylation method, the zeta potentials for 4nm samples were generally higher (or, closer to neutral) than the zeta potential for the equivalent 10nm sample. And finally, a definitive trend in zeta potentials as a function of PEGylation method was not observed.

TGA results generally indicated averages similar to the targeted surface density of 0.7 PEG chains/nm<sup>2</sup>. Importantly for the comparability of these results to one another, there were no statistically significant differences ( $p > 0.05$ ) in surface density between particles within the same PEGylation method and core size (e.g. all 10nm PO-PEG SPIONs) – with the exception of 4nm DSPE-PEG 5k samples, which exhibited a significantly higher surface density than either 1k or 2k DSPE-PEG samples of the same core size ( $p < 0.05$ ). This means that MR results from each given PEGylation method and core size are solely due to differences in PEG chain length, with the exception of results from the 4nm DSPE-PEG 5k samples (c.f., MR results below). Additionally, there were no statistically significant differences in surface density between particles with the same PEG chain length and core size (e.g. all 4nm SPIONs with any 1k PEG). This means that MR results from each given core size and PEG chain length are solely due to differences in PEGylation method, and the chemical differences in the resulting particles.

### *MR Equipment & Experiments*

The impact of SPION core size, PEGylation method, and PEG chain length on  $r_1$  relaxivity was marked (**Figure 3.4**). The PEGylation method and the resulting chemical composition of the layer closest to the SPION core had a large impact on agent  $r_1$  rate. DSPE-PEG SPIONS had a markedly lower  $r_1$  relaxivity than either NH<sub>2</sub>-PEG or PO-PEG SPIONS. For 4nm SPIONS with comparable PEG chain lengths, NH<sub>2</sub>-PEG SPIONS had  $r_1$  relaxivities at least 2.15x higher than PO-PEG SPIONS, and at least 8.23x higher than DSPE-PEG SPIONS for equivalent PEG chain lengths. For 10nm SPIONS, NH<sub>2</sub>-PEG SPIONS had  $r_1$  relaxivities of at least 2.09x higher than PO-PEG SPIONS, and at least 33.87x higher than DSPE-PEG SPIONS.

Interestingly, for NH<sub>2</sub>- and PO-PEG SPIONS, the maximum effect imparted on  $r_1$  relaxivity by changing the PEG chain length was between 34-45% and was not markedly different for the two different core sizes. However, for DSPE-PEG SPIONS,  $r_1$  relaxivity differed by a factor of 360 (10 nm core) to 480% (4 nm core) by changing the PEG chain length.

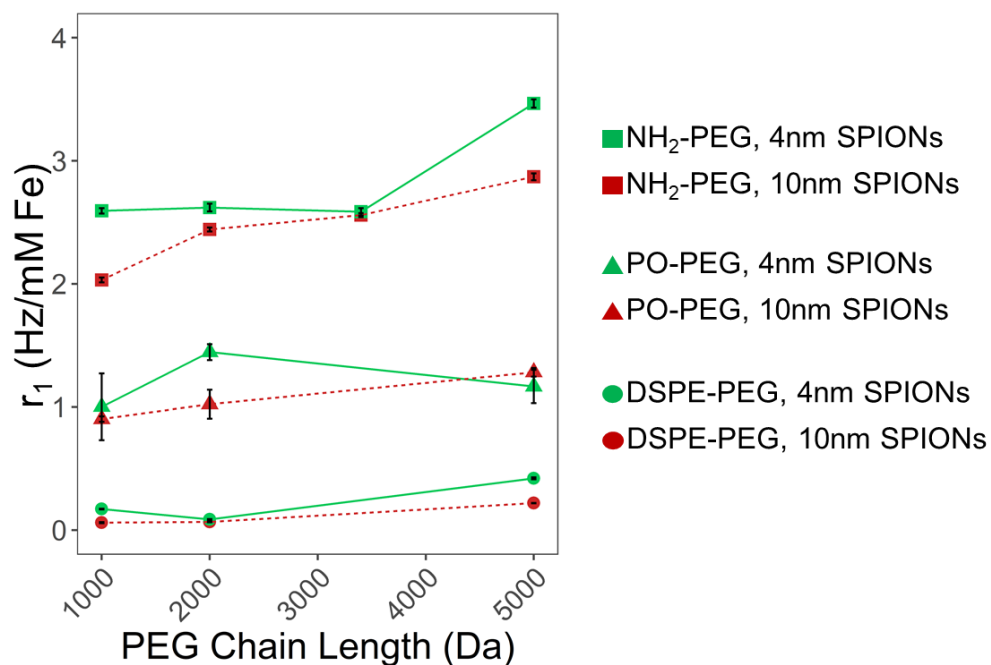


**Figure 3.4:** Impact of SPION core size and PEG chain length on  $r_1$  for PO-PEG SPIONs, NH<sub>2</sub>-PEG SPIONs, and DSPE-PEG SPIONs. Error bars are standard error in the calculated slope value.

For 10nm SPIONs, increasing the PEG chain length generally resulted in an increase in  $r_1$  relaxivity (Figure 2). For 4nm SPIONs, a trend was not apparent. With the notable exception of the 5k PO-PEG SPIONs for which the 10nm SPION had a higher  $r_1$  relaxivity, for all PEGylation methods and PEG chain lengths, 4nm SPIONs had higher  $r_1$  relaxivities than their 10nm counterparts. This is the opposite effect than expected (and previously reported) for  $r_2$  relaxivity. Differences in equivalent samples with different core sizes ranged from 0.91x (PO-PEG5k, where the  $r_1$  of 10nm samples was greater than that of 4nm samples) to 2.84 (DSPE-PEG1k).

The impact of SPION core size, PEGylation method, and PEG chain length on  $r_2$ , as measured using the CPMG method, was significant, and only partly in line with what was observed with the  $r_1$  trends (**Figure 3.5**). Again, the PEGylation method and the resulting chemical composition of the layer closest to the SPION core had the most definitive impact on  $r_2$  relaxivities. In line with  $r_1$  results, across PEG chain lengths,  $\text{NH}_2$ -PEG SPIONs had the highest  $r_2$  relaxivities; 1.41 – 4.67x higher than DSPE-PEG SPIONs and 1.06 – 7.02x higher than PO-PEG SPIONs.

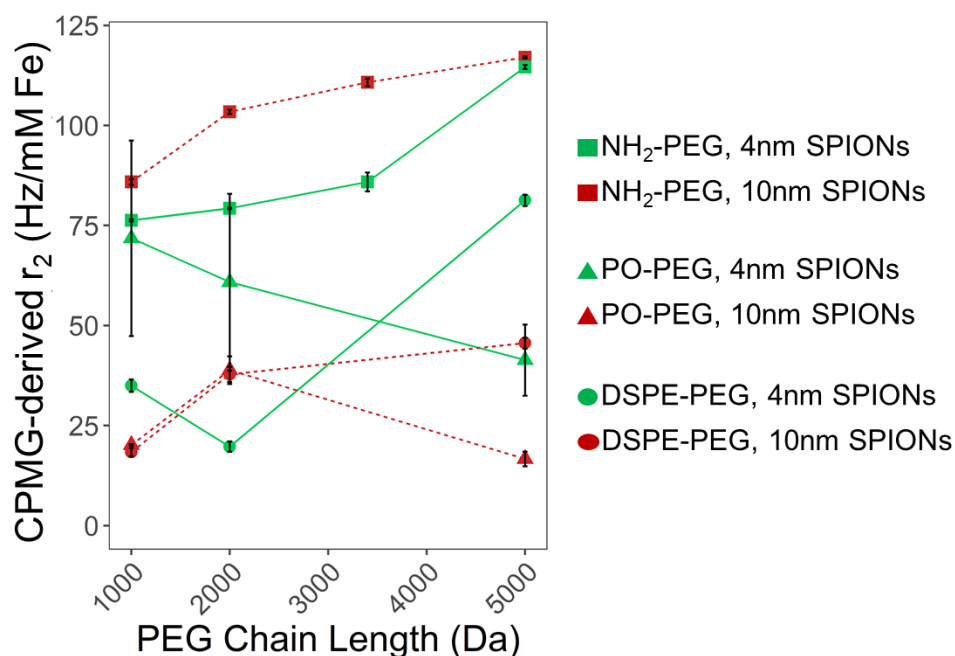


**Figure 3.5:** Impact of SPION core size and PEG chain length on  $r_2$  CPMG for PO-PEG SPIONs,  $\text{NH}_2$ -PEG SPIONs, and DSPE-PEG SPIONs. Error bars are standard error in the calculated slope value.

For  $\text{NH}_2$ -PEG SPIONs with both 4nm and 10nm cores, increasing the PEG chain length lead to an increase in  $r_2$  relaxivity. This was also the case only for DPSE-

PEG SPIONs with 10nm cores. For DSPE-PEG SPIONs with 4nm cores the largest PEG length also led to the largest  $r_2$ , but there was a drop in  $r_2$  at the intermediate PEG length. For PO-PEG SPIONs with 10nm cores, there was not a definitive trend. However, for PO-PEG SPIONs with 4nm cores, increasing the PEG chain length lead to a consistent decrease in  $r_2$  relaxivity. Additionally, for  $\text{NH}_2$ -PEG SPIONs,  $r_2$  relaxivities were higher for the 10nm core sizes at each PEG chain length. Differences in equivalent samples with different core sizes ranged from 1.02x (PEG5k) to 1.30x (PEG2k). However, the opposite was true for PO-PEG SPIONs. Differences in equivalent samples with different core sizes for PO-PEG SPIONs ranged from 1.57x (PEG2k) to 3.56x (PEG1k). Differences in equivalent samples with different core sizes for DSPE-PEG SPIONs did not show a consistent trend.

Spin echo-derived  $r_2$  relaxivities were higher than or comparable to (i.e. the calculated values share an overlapping standard error range) CPMG relaxivities as expected (**Figure 3.6**). Where they were greater,  $r_2$  SE-derived relaxivities were 1.023x to 1.20x the  $r_2$  CPMG-derived relaxivities, with the highest ratio observed for 5k PO-PEG, 10nm SPIONs.

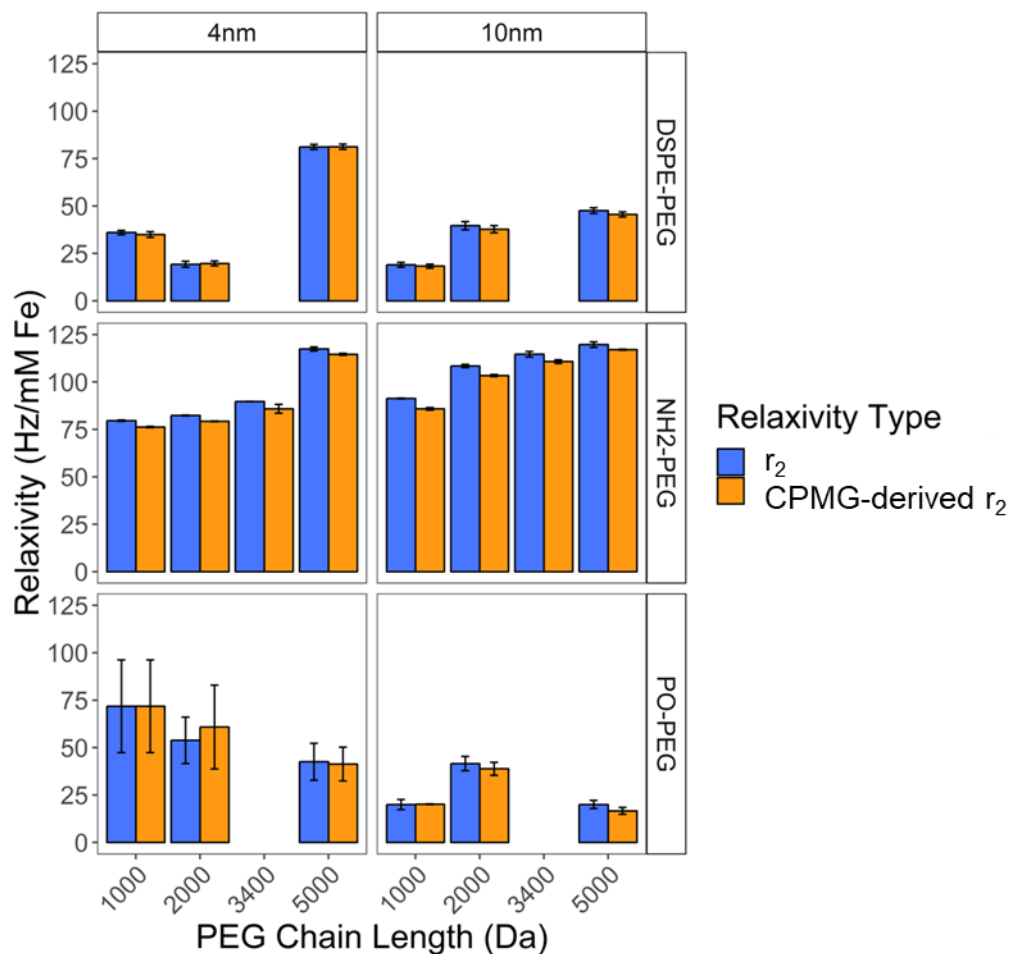


**Figure 3.6:** Comparison between relaxivities derived from SE measurements (blue) and CPMG measurements (orange). The general similarity of these results indicates that diffusion of particles in solution did not play a substantial role in altering measured relaxation rates. As with other experiments, 3.4k PEG samples were only tested in NH<sub>2</sub>-PEG SPIONs due to limited PEG agent availability. Error bars are standard error in the calculated slope value.

The  $r_2^*$  relaxivities are provided in **Figure 3.7**. The impact of SPION core size, PEGylation method, and PEG chain length on  $r_2^*$  was significant. With the exception of the 4nm 1k PO-PEG SPIONs, NH<sub>2</sub>-PEG SPIONs had the highest  $r_2^*$  relaxivities across PEG chain lengths. For NH<sub>2</sub>-PEG SPIONs with both 4nm and

10nm cores, increasing the PEG chain length lead to an increase in  $r_2^*$  relaxivity. This was also the case only for DPSE-PEG SPIONs with 10nm cores. For DSPE-PEG SPIONs with 4nm cores, and for PO-PEG SPIONs with 10nm cores, there was not a definitive trend. However, for PO-PEG SPIONs with 4nm cores, increasing the PEG chain length lead to a consistent decrease in  $r_2^*$  relaxivity. Additionally, for  $\text{NH}_2$ -PEG SPIONs,  $r_2^*$  relaxivities were higher for the 10nm core sizes at each PEG chain length, while the opposite was true for PO-PEG SPIONs. Differences in equivalent samples with different core sizes for DSPE-PEG SPIONs did not show a consistent trend.

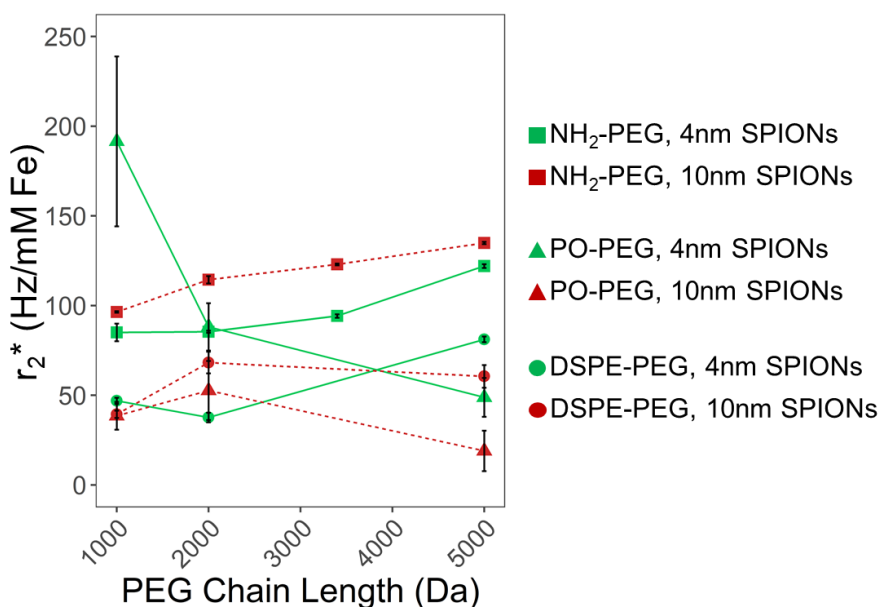


**Figure 3.7:** Impact of SPION core size and PEG chain length on  $r_2^*$  for PO-PEG SPIONs,  $\text{NH}_2$ -PEG SPIONs, and DSPE-PEG SPIONs. Error bars are standard error in the calculated slope value.

The  $r_2^*$  relaxivities are plotted vs.  $r_2$  relaxivities for each given sample in **Figure 3.8**. As expected, they were either comparable to (with the inclusion of standard

error) or significantly greater than CPMG relaxivities. Where they were greater,  $r_2^*$  were 1.08x to 2.67x the  $r_2$  CPMG-derived relaxivities, with the highest ratio observed for 1k PO-PEG, 4nm SPIONs. This particular data point was deemed an outlier and excluded from further analysis. Linear regressions were performed on these data not including the outlier, and are indicated with the black lines in **Figure 3.8**. Grey shading indicates the 95% confidence interval. It can be observed that there is a strong positive correlation between  $r_2^*$  and  $r_2$  for each PEG attachment method (all  $R > 0.85$ ). For  $\text{NH}_2$ -PEG SPIONs, the relationship between  $r_2^*$  and  $r_2$  is almost perfectly linear ( $R = 0.986$ ). The slopes of the linear regression also vary with PEG attachment method:  $0.69 \pm 0.16$  for DSPE-PEG SPIONs,  $1.13 \pm 0.07$  for  $\text{NH}_2$ -PEG SPIONs, and  $1.35 \pm 0.24$  for PO-PEG SPIONs (mean  $\pm$  standard error). While the  $\text{NH}_2$ -PEG SPIONs and PO-PEG SPIONs are comparable, given the overlapping standard errors, the relaxivities of the DSPE-PEG SPIONs have a significantly different relationship.

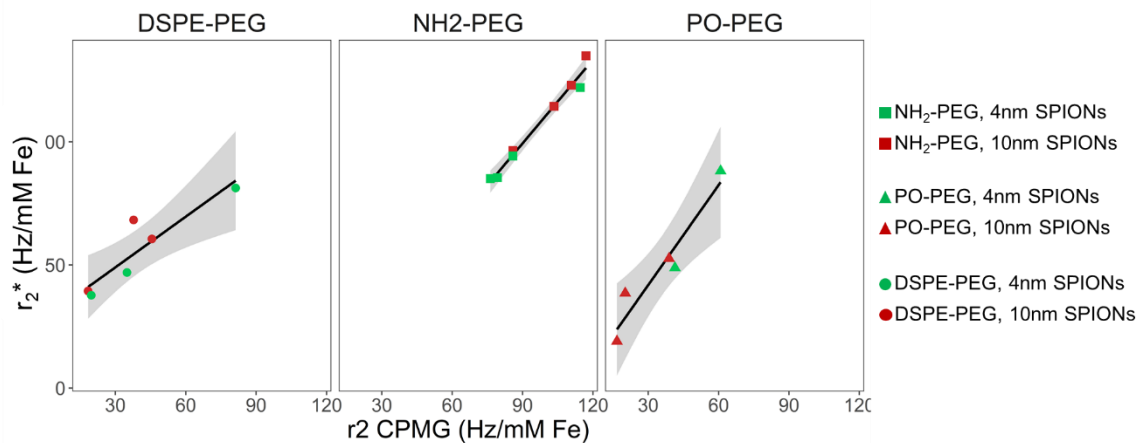


**Figure 3.8:** Relationship between  $r_2^*$  and CPMG-derived  $r_2$  values across all samples. Black lines indicate fit from a linear regression; grey shading indicates the 95% confidence interval.

### **3.4 Discussion**

Because HA deposits in early CAVD are generally present in very small quantities, it is desirable and necessary to synthesize SPIONs with substantial signal enhancement. This will ultimately help to improve the sensitivity of diagnosis, and enable the detection of earlier disease in patients. As discussed in the introduction to this chapter, SPION signal enhancement can be achieved via one of two methods: 1) optimizing targeted SPION binding to HA, to ensure that as many SPIONs as possible can bind to the target, and/or 2) optimizing the targeted SPION makeup to enhance MR signal of the particles themselves.

For approach 1 (optimizing targeted SPION binding to HA to ensure that as many SPIONs as possible will bind to the target), different peptide quantities per SPION were tested to better understand whether or not altering the density of the peptide coating could improve the binding properties of the SPIONs. It was largely observed that altering either the number of peptides per SPION or the composition of the peptide coating in terms of HABP:OPN ratio did not yield large quantitative differences in particles binding to a given quantity of HA. This is perhaps unsurprising, especially as these studies were not performed under flow conditions. While it may be helpful for more peptides on each SPION to bind to HA, these differences may not be measurable under the conditions used for these experiments. Future work may be performed to observe differences in the binding properties of SPIONs with different quantities of attached peptide under flow,

where the number of peptides per SPION that successfully bind to the HA may have more of an impact. However, as the only significant differences observed in these studies were between samples with 5 peptides/SPION and 50 peptides/SPION, and as neither set of samples showed significant differences from samples with 25 peptides/SPION, 25 peptides/SPION was chosen as the baseline value for both HABP- and OPN-SPIONS moving forward. However, it should be noted here that, as SPIONS with 10 peptides/SPION yielded statistically similar results for both HABP- and OPN-SPIONS, these could be used instead for future studies if cost-effectiveness of SPION production is of concern.

Additionally, to fully explore options for approach 1, SPIONS with different ratios of HABP:OPN combined onto a single SPION were tested. It was hypothesized that, given the slightly different properties of HABP- and OPN-SPIONS at low concentrations of HA (Figure 2.4), this approach might serve to combine the properties of both HABP- and OPN-SPIONS in a quantifiable manner. These, similarly, did not yield significant differences in terms of the binding properties of the SPIONS. As there was no measurable difference in SPION binding properties when both HABP- and OPN-peptides were used in comparison to when only one peptide was used, HABP- and OPN-SPIONS were produced separately for the remainder of the studies described in this dissertation. This was done because HABP and OPN peptides are two of the most expensive reagents in the SPION production process; these results indicate that purchasing both peptides and combining them to coat the SPIONS is unnecessary from a signal optimization

standpoint.

For approach 2 (optimizing the targeted SPION makeup to enhance MR signal of the particles themselves), as previously discussed, 20 different SPION samples were produced with different core sizes, PEG chain lengths, and PEGylation methods.

SPION core sizes of 10 and 4nm were chosen to reflect those sizes that are often developed for MR applications in the literature.<sup>38,113,145</sup> SPIONs are often grouped into three categories based on size: (1) standard SPIONs (50–180nm), (2) ultrasmall SPIONs (10–50nm), and (3) very small SPIONs (<10nm).<sup>114</sup> The core sizes selected allow us to examine both ultrasmall and very small SPIONs, which are indeed the most commonly encountered.

The three PEGylation methods selected represent a cross section of different PEGylation methods widely used in the literature, and were chosen based on the chemical properties they would impart to the nanoparticles. It was hypothesized that the hydrophilicity or hydrophobicity of the chemical group closest to the SPION core would have a large impact on the MR relaxivities, as this is largely dependent on the ability of water to move around and close to the SPION cores.

Method 1 (PO-PEG) is similar to many direct PEGylation or direct ligand exchange methods, where the SPION cores are PEGylated in a one-step process that relies on direct interaction between a functional group on the PEG and the SPION

core.<sup>137</sup> This particular method will result in SPIONs with a small, combination hydrophilic/hydrophobic group closest to the core; PO-PEG dissolves readily in a combination of ethanol and n-hexane. Method 2 (NH<sub>2</sub>-PEG) is similar to many two-step processes, where a ligand exchange is performed to first replace the original (often hydrophobic) coating of the SPIONs, followed by PEGylation via attachment to the new coating material.<sup>97,98</sup> This particular method will result in SPIONs with a small, strongly hydrophilic group closest to the core. Method 3 (DSPE-PEG) is similar to many one-step processes that rely upon somewhat weaker hydrophobic interactions or associations to link the PEG to the SPION core.<sup>135</sup> This particular method will result in SPIONs with a bulky, very hydrophobic group closest to the core.

The PEG chain lengths (1000, 2000, (3400), and 5000 Da) were selected because they tend to be widely commercially available, and have been widely used in previous reports dealing with functionalized SPIONs.<sup>97,98,135,137</sup> The targeted PEG chain density on the SPIONs (0.7 PEG chains/nm<sup>2</sup>) was selected as a fairly high target; this target should be close to the maximum of what is feasible in a well-equipped laboratory setting.<sup>146</sup>

DLS measurements were chosen to observe effective rather than absolute diameters as the behavior of particles in solution was of particular interest for this study. Effective diameters were measured in DI water, so any contribution of ions should be negligible; however, differences in the amount of aggregation or the

spread of the PEG layer should be reflected in differences in the measured effective diameter. Because both aggregation as well as PEG chain conformation may impact measured MR relaxivities, effective diameter measurements were of more use than absolute diameter as measured by methods such as, e.g., transmission electron microscopy (TEM). In this series of measurements, variations between samples fabricated with different parameters were observed.

It would generally be expected that, with equivalent core sizes and PEGylation methods, longer PEG chain lengths would lead to larger effective diameters, as observed with PO-PEG SPIONs. However, in cases where this was not observed, it is possible that aggregation effects were at play; for example, DSPE-PEG SPIONs with smaller PEG chain lengths may aggregate more readily, and thus only the effective diameter measured for the 5k DSPE-PEG SPIONs measured the effective diameter of single SPIONs, rather than multiple particles. This seems to be a likely explanation particularly for DSPE-PEG SPIONs, as the effective diameter of 5k DSPE-PEG SPIONs was generally substantially lower than the 2k DSPE-PEG SPIONs of the same core size. The larger standard deviation observed in DSPE-PEG SPION effective diameter measures could also be reflective of aggregation. For NH<sub>2</sub>-PEG SPIONs, where the general size progression is 1k < 2k < 5k < 3.4k, it is thought that the observed difference between 3.4k and 5k samples may be due to a difference in the preferred PEG chain conformation, or to potentially a small amount of aggregation occurring, as the standard deviations are not as high as those observed for DSPE-PEG SPIONs.

In comparing samples with similar PEGylation methods and PEG chain lengths, it would be expected that the effective diameter of 4nm samples would be smaller than 10nm samples. This was confirmed for both PO-PEG and NH<sub>2</sub>-PEG SPIONs. However, this was not true for DSPE-PEG SPIONs. It is likely that, again, aggregation plays a role in these results, and that perhaps DSPE-PEG SPIONs are less stable in aqueous solution than samples where there is a more hydrophilic group present closer to the core.

Zeta potential measurements reflect the potential at the slipping/shear plane of particles in solution.<sup>147</sup> While PEG itself does not carry a high surface charge, SPIONs alone in solution tend to carry a high negative charge (e.g. CA-SPIONs have a zeta potential of around -35mV; the zeta potential of OA-SPIONs in water cannot be measured, as OA-SPIONs are insoluble in water). It is thus expected that coating with the more neutral PEG will raise the zeta potential of the particles closer to neutral (0mV).<sup>147,148</sup> This was observed in all cases.

The general increase towards neutral of zeta potential with increasing PEG chain length may perhaps be expected; it is possible that longer PEG chains help to better “mask” the highly negatively charged SPION core. Additionally, the higher zeta potential in the 4nm samples as compared to the 10nm samples of the same PEGylation method and PEG chain length may be due to the same effect; the PEG chains are simply larger with respect to the size of the SPION core, and may thus do a better job of masking the negative charge of the core. Finally, it is intuitively

understood that there was no observed trend in zeta potentials as a function of PEGylation method, since the solution-facing ends of each PEG chain should have been chemically identical regardless of the PEGylation method.

The observed results from TGA tests simply indicated that the majority of samples have non-significant differences in terms of surface coverage (with the exception of 4nm DSPE-PEG 5k samples, which have a statistically significantly greater surface coverage). This indicates that, with the exception of the 4nm DSPE-PEG 5k SPIONs, observed differences in MR relaxivities between samples will solely be due to differences in core size, PEG chain length, or PEGylation method. This is an important confirmation step that has been omitted in previous literature examining the impact of these parameters on SPION MR properties.<sup>98,135</sup>

Perhaps the most salient trend in MR measurements is that  $r_1$  and  $r_2$  relaxivities are greater in NH<sub>2</sub>-PEG SPIONs than either PO-PEG or DSPE-PEG SPIONs of the same core size and PEG chain length. It is hypothesized that this is due to the hydrophilic nature of the group closest to the core for these SPIONs (citric acid), in comparison to the less hydrophilic nature of the phosphine oxide and the hydrophobic nature of the DSPE. The more hydrophilic group near the core may allow water to move more easily closer to the core, and spend more time in proximity to the magnetic field generated by the core. In comparing PO-PEG and DSPE-PEG SPIONs across particles with the same core size and PEG chain length, results appear to differ between  $r_1$  and  $r_2$  relaxivities. PO-PEG SPIONs

show far higher  $r_1$  relaxivities across the board. However, the difference between  $r_2$  relaxivities for PO-PEG and DSPE-PEG SPIONs do not show a consistent trend. As expected,  $r_2^*$  relaxivities were either comparable to, or greater than, CPMG-derived  $r_2$  relaxivities.

For NH<sub>2</sub>-PEG and DSPE-PEG SPIONs, within a given SPION core, increasing the PEG chain length from 1k to 5k generally lead to an increase in for  $r_1$  and CPMG-derived  $r_2$  relaxivities. This is in keeping with results from Tong, et al. who considered PEG chain lengths over 1kDa.<sup>135</sup> This is likely because the increased PEG chain length creates a larger corona which slows the movement of water molecules around the particle, thus increasing the amount of time the water protons spend in proximity to the core. Interestingly, this is not true for PO-PEG SPIONs, which do not show a consistent trend with PEG chain length. While for 4nm PO-PEG SPIONs, increased PEG chain length leads to decreased  $r_2$ , this does not hold true for 10nm PO-PEG SPIONs.

The trend observed with respect to the  $r_2$  vs.  $r_2^*$  data is likely because the coating of the particles has an impact on the magnetic field. The particles with more hydrophilic coatings (NH<sub>2</sub>-PEG SPIONs and PO-PEG SPIONs) showed similar relationships between  $r_2$  and  $r_2^*$ , while DSPE-PEG SPIONs showed a substantially lower slope in the regression. This may mean that the hydrophilicity or hydrophobicity of the group closest to the core has an effect on the magnetic field.

Results of this study do not necessarily corroborate some previous findings,<sup>131,132</sup> for example that SPIONs with larger core sizes yield higher  $r_2$  relaxivities in

samples with equivalent PEG chain length and PEGylation method. Although this is true for NH<sub>2</sub>-PEG SPIONs, there is a less distinctive trend for both PO-PEG and DSPE-PEG SPIONs. The trend observed in 5kDa PO-PEG SPIONs could potentially be linked to the increased surface coverage of the 4nm samples as measured by TGA; however, this is not the case in the 1kDa samples. On the other hand, SPIONs with larger core sizes generally yielded lower (or comparable) R1 relaxivities in samples with equivalent PEG chain length and PEGylation method. This trend may be related to recent results demonstrating that SPIONs with sufficiently small core diameters can actually be used as T1 contrast agents.<sup>137,149</sup> Additional work will need to be performed to further elucidate the impact of SPION core size on MR relaxivities with different PEG attachment methods.

Although other direct relationships between relaxivities and the other measured parameters were examined, there were largely no significant correlations (data not shown). In the future, it may be beneficial to perform multiparametric modeling on these or similar results to observe the combined impact of multiple factors.

Overall, results from these studies indicate that the chemical composition and, in particular, the hydrophobicity/hydrophilicity of the group that serves to link PEG chains to a SPION core may actually play a larger role in the resulting MR signal than other variable properties such as SPION core size and PEG chain length. In addition, these studies show that the impact of SPION core size and PEG chain length on the resulting sample relaxivities is not a simple relationship, but appears

to be conflated as well with the impact of the PEGylation method and the nature of the chemical group closer to the SPION core. To our knowledge, this is the first time a study has been performed examining the impact of PEGylation method on MR signal; it is also the first time such a comprehensive and controlled study of the impact of different fabrication parameters on MR signal has been performed.

## **Chapter 4: Characterization of the Medical Properties of Targeted SPIONs**

### ***4.1 Introduction***

Previous work described in Chapters 2 and 3 detailed the fabrication, *in vitro* characterization, and MR signal optimization of HA-targeted SPIONs. In this chapter, we focus on the medically-relevant properties for the eventual successful clinical use of these targeted SPIONs.

In the clinic, HA-targeted SPIONs intended for use in the detection of early-stage CAVD would be administered to patients, potentially intravenously, and would be expected to bind to any HA deposits present in the aortic valve. They may additionally demonstrate off-target binding to HA present elsewhere in the body. The final, fully-functionalized and bound SPIONs must therefore be detectable via standard MR imaging; they must not cause harmful systemic or local effects; and they must be able to reach their target and bind successfully. The experiments described in this chapter aim to show that the HA-targeted SPIONs fabricated in Chapter 2 and optimized in Chapter 3 have all of these properties, and are thus suitable for further testing development.

Although the MR signal of PEGylated SPIONs was measured and optimized as discussed in Chapter 3, these results do not account for the potential impact of the addition of a targeting peptide on the MR signal. Previous results in the literature have only occasionally addressed the fact that the addition of any targeting moiety

such as a peptide will alter the MR signal of SPIONs.<sup>150,151</sup> The study by Faraj, et al. indicates that the addition of an antibody in their system typically led to an increase in R2 and no alteration in R1, though the increase was inconsistent between samples.<sup>151</sup> Many studies simply perform MR measurements with the final, fully-conjugated SPIONs.<sup>152–154</sup> Measuring the change in MR signal as a result of peptide addition can aid in understanding what may be expected in measurements made in a clinical setting.

An additional, crucial pre-clinical MR study entails measuring the MR signal of SPIONs bound to HA *in vitro*. Previous results in the literature have reported that bound SPIONs generally demonstrate an increased MR signal compared to unbound SPIONs.<sup>155,156</sup> This is thought to be because particles bound to their target will move more slowly through solution, and thus moving water molecules in the solution will spend more time in proximity to the core, leading ultimately to an increased MR signal. Although we have already demonstrated SPION binding to HA *in vitro*, observing binding via an alteration in MR signal is an additional, orthogonal method that can be used to confirm that binding is occurring. MR measurement of the fully-functionalized particles and confirmation of binding via MR are important benchmarks for ensuring particle functionality in a clinical setting.

The potential for harmful systemic effects of HA-targeted SPIONs also must also be addressed. Unlike gadolinium contrast agents, SPIONs generally display low cytotoxicity, particularly for PEG-coated particles at relevant concentrations under

100  $\mu\text{g/mL}$ .<sup>157–159</sup> As others have reported, doses in humans have been  $\sim 1\text{mg Fe/kg}$ , corresponding to far less than 100  $\mu\text{g/mL}$  ( $\sim 13\ \mu\text{g/mL}$  for an average adult male in the United States).<sup>160</sup> Although transient systemic effects (e.g. diarrhea, nausea, headache) have been observed *in vivo* in some studies, these effects were reversible and diminished over time.<sup>51,161,162</sup> Hypersensitivity/anaphylaxis reactions have been reported in the FDA-approved, carbohydrate-coated iron oxide agent Feraheme,<sup>51</sup> indicating that further clinical evaluation of any potential iron-oxide based contrast agent would be of the utmost importance. Subsequent to injection, particles with diameters  $<60\text{nm}$  showed circulation times of  $\sim 90$  minutes, and tended to accumulate in the liver (80-90%) and the spleen (5-8%), with smaller quantities present in the brain, heart, kidney, lung tissue, bone marrow, and lymph nodes.<sup>163,164</sup> The overall lack of long-term negative effects from SPIONs is thought to be primarily because they are degraded and cleared from systemic circulation by endogenous iron metabolic pathways, including uptake by macrophages in the liver and spleen.<sup>161,163,165</sup> Thus, the systemic effects of SPIONs are generally considered to be minimal, although many studies continue to evaluate SPION toxicity in specific cell cultures, with specific surface modifications, and with specific incubation times. In this chapter, we evaluate the specific toxicity of PEG-, HABP-, and OPN-SPIONs at a biologically relevant dosage and incubation time in HUVECs to ensure safety in their ultimate *in vivo* application.

In addition to considerations of systemic or cellular toxicity, the impacts of functionalized SPIONs on HA nucleation and formation are unknown. OPN and related peptides have been shown in literature to contribute to slowing the nucleation and formation of HA nanocrystals, in addition to potentially disrupting existing crystal structures.<sup>73,120</sup> Although from the standpoint of CAVD, this effect may be beneficial and lend the functionalized SPIONs theranostic capabilities, this could present clinical issues systemically. HA nucleation and formation in the body is an active and ongoing process, not only where diseases such as CAVD are present, but also in maintenance of the skeletal system.<sup>166</sup> Therefore, although preventing or disrupting HA deposition may help to treat CAVD by preventing further deposition of HA in the aortic valve, ultimately, the potential for negative systemic effects also must be explored. Previous studies such as those by de Bruyn et al. have examined HA nucleation and formation *in vitro* by using a borderline-saturated calcium-phosphate solution and examining the formation of HA nanocrystals over time using DLS.<sup>100</sup> These studies tested the impact of adding various forms of the osteopontin protein (phosphorylated and non-phosphorylated) prior to mixing of the calcium and phosphate solutions, and determined that all tested forms of osteopontin do inhibit HA nucleation and formation. However, these studies were not performed in serum. Thus, in order to assess the impact of SPIONs on HA nucleation and formation, both HABP and OPN peptides and functionalized SPIONs were tested in a similar experimental setup, both without serum and in the presence of 50% serum.

Another important consideration in developing HA-targeted SPIONs for use as a CAVD diagnostic tool is the ability of the nanoparticles to reach their target *in vivo*. Small deposits of HA found in early stages of CAVD are contained within the valve structure; that is, they are subendothelial.<sup>167</sup> Therefore, particles in the bloodstream must pass through the endothelial barrier to reach the HA deposits. Although previous studies by Kim et al. have demonstrated that nanoparticles of diameters <70nm are able to pass through the endothelial barrier under inflammatory conditions in atherosclerotic vessels,<sup>168</sup> similar studies have not been performed in heart valves, which experience vastly different pressures and flow dynamics than vessel walls. For example, the aortic valve experiences direct pressure during diastole, while vessel walls typically experience shear stress (**Figure 4.1A**).<sup>57</sup> To account for this, we used a unique Transwell™ and centrifugation setup that we developed and customized particularly for this application. Transwell experiments were performed to examine nanoparticle translocation through an endothelial cell layer under physiologically-relevant pressures, and their ability to bind to HA subsequently.

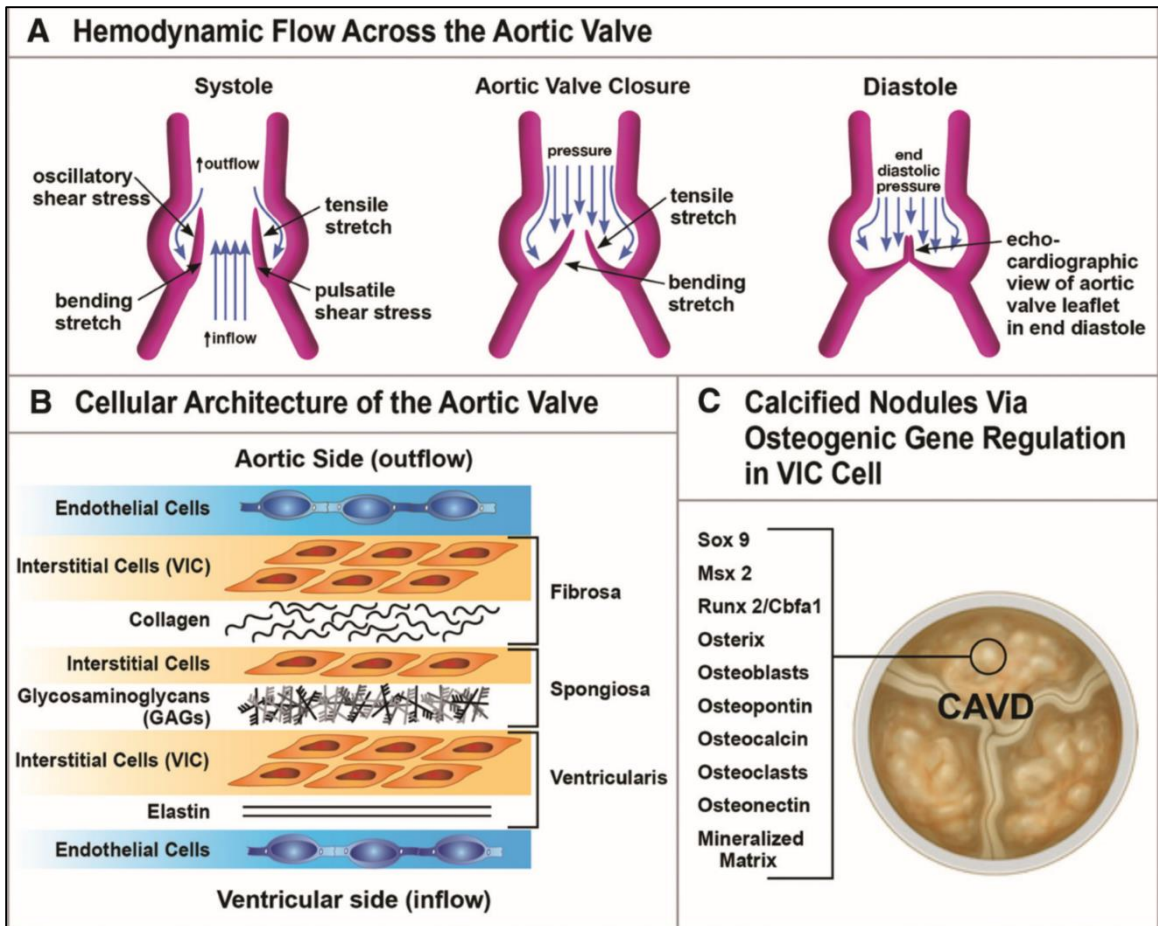


**Figure 4.1:**<sup>57</sup> **(A)** Hemodynamic force perspective of systole and diastole in the aortic valve. **(B)** Graphic representation of the cellular and extracellular architecture of a normal aortic valve. **(C)** Representation of the genes involved in the osteogenic phenotype of a calcified aortic valve surface.

Finally, although the studies described thus far have evaluated binding to HA under medically-relevant circumstances, binding to HA in diseased valve samples has not yet been evaluated. The microenvironment in the aortic valve will differ distinctly from the experimental setups described thus far in this dissertation. In addition to HA, amorphous calcium phosphate, and endothelial cells, the aortic

valve contains interstitial cells and extracellular matrix components including collagen, glycosaminoglycans, and elastin (**Figure 4.1B**). Assessing HA-SPION binding to HA deposits in the aortic valve can be performed either by examination of an animal model, or by using excised human aortic valve samples.

Although there are several animal models of CAVD, to date no single animal model is fully characteristic of human CAVD.<sup>57</sup> The most commonly used animal models are mouse, rabbit, and pig models. However, the mouse aortic valve structure differs significantly from that of humans,<sup>169</sup> rabbits do not form spontaneous atherosclerotic lesions and differ from human in their lipid metabolism,<sup>170–175</sup> and porcine models are often prohibitively expensive and difficult to maintain. To overcome these limitations, we have instead tested the binding of HA-SPIONs in excised human aortic valve samples. These results have illustrated the selective binding of HABP-SPIONs in particular to diseased samples.

Our findings from these diverse experiments have demonstrated, overall, that the HA-targeted SPIONs described in this dissertation are suitable for further development as a contrast agent for the early detection of CAVD. MR studies indicated that, as expected, SPION functionalization with peptides does alter the MR signal of the final, HA targeted SPIONs, and that SPION binding to HA can be observed via MR, despite the limitations of this measurement. Cytotoxicity studies have confirmed that none of the functionalized SPIONs exhibited cytotoxic qualities. Transwell studies have shown that, while both HABP- and OPN-SPIONs

were able to pass through an endothelial barrier, only HABP-SPIONs exhibited significant subsequent binding to HA. Finally, in studies using excised human aortic valve samples, HABP-SPIONs showed selective binding to diseased samples. Together, these results suggest that HABP-SPIONs in particular have demonstrated the potential for success in their intended application, and merit further study as a potential MR contrast agent for early detection of CAVD.

## ***4.2 Materials and Methods***

A variety of experiments were performed using HABP-, OPN-, and PEG-SPIONs to determine whether these SPIONs are suitable for further development as a clinical contrast agent. These experiments evaluated the functionalized SPIONs in terms of their MR properties, cyto- and systemic toxicity, ability to pass through an endothelial layer, and their selectivity in binding to diseased human valve samples.

### ***Materials***

Materials previously discussed in Chapters 2 and 3 were obtained from the same sources described therein. Ticagel Bind-KX and FASTir Xanthan EC were generously donated by TIC Gums. The LIVE/DEAD assay kit was purchased from ThermoFisher Scientific (Waltham, MA). The 0.4 $\mu$ m pore, PE Transwell plates

were purchased from Corning, in addition to all cell culture flasks and plates (Corning, NY). Human aortic valve samples were obtained through the National Disease Research Interchange (NDRI, Philadelphia, PA).

All statistical analysis and figure generation was performed in R, version 3.5.1.

#### *Preparation of Bound and Unbound Samples for MR Measurements*

The iron concentration in each solution was determined using a simple absorbance assay at 510nm, based on solutions containing known quantities of iron. Solutions at different concentrations (0, 5, 25, 50, 75, and 100 ppm) were prepared by dilution for MR. For evaluation of the relaxivity of functionalized SPIONs, these dilutions were performed in water. For evaluation of the relaxivities of bound vs. unbound SPIONs, the suspended HA solutions were created by mixing measured quantities of HA (Sigma, St. Louis, MO) with a gel-like mixture of 0.5% Ticagel Bind-KX and 0.1% FASTir Xanthan EC. For control (unbound) samples, the gel was created without the addition of HA. The solutions were stored in plastic cryogenic vials, and the amount of air in each vial was minimized to eliminate signal interference from the air-water interface. All vials were embedded into Styrofoam for MR measurements.

### *MR Equipment & Experiments*

Two MR experiments were performed for each set of samples. One experiment was designed to measure  $R_2$  and one was designed to measure  $R_1$ . All experiments were performed on a 3 Tesla GE HDx clinical MR imager (GE, Milwaukee, WI) equipped with 40 mT/m gradients capable of 150 mT/m/sec slew rate and an 8-channel brain phased array receiver coil for signal reception.

Because T2 measurements using this Hahn single echo spin echo sequence are sensitive to molecular diffusion, an experiment was performed to measure  $R_2$  using a three-dimensional multi-echo spin echo Carr-Purcell-Meiboom-Gill sequence.<sup>139-143</sup> This sequence utilized non-selective radiofrequency pulses with composite refocusing ( $90_x-180_y-90_x$ ) as well as gradient crushers that alternated in polarity in every echo and that diminished in amplitude at every pair of echoes.<sup>144</sup> Sequence parameters were 1.5 sec TR, 16 echoes evenly spaced at 7.4 ms (first echo at 7.4 ms, last echo at 118.4 ms), 2 mm slice thickness, 13-15 cm FOV, 96 (readout)  $\times$  72 (phase)  $\times$  38 (slice) matrix, 1 signal average, and  $\pm 32.8$  kHz bandwidth. SNR was typically  $>100$  at the first echo, and reducing to no less than 30 at the 4th echo for the highest agent concentration.

$R_1$  was measured using a two-dimensional single echo spin echo sequence but with a fixed echo time of 9 ms and independently repeated for 12 repetition times ranging from 100 ms to 9 sec ( $TR_i=100, 250, 500, 750, 1000, 1366, 1750, 2500, 4000, 5500, 7000, \text{ and } 9000$  ms). Other parameters were identical to the single

echo spin echo  $R_2$  experiment except that 4 signal averages were used for the shorter TRs in order to increase SNR, except for acquisitions with TR >2.5 sec for which only 1 signal average was used to maintain a reasonable scan time. With these parameters, SNR was between 10-30 for the three shortest TRs and >30 for the remaining TRs.

### *MR Analysis*

Analysis of MR signal intensities to determine sample relaxation rates was performed using custom software developed in MATLAB (version R2013b, MathWorks Inc., Waltham MA). The software performed non-linear non-negative least squares fitting of signal intensity measurements across either the echo (for T2, T2\*) or the repetition times (for T1), using idealized mono-exponential signal models. For T2 measurements, the signal model was  $s(TE_i) = s_{TE=0} e^{-TE_i R}$ , where R the corresponding  $R_2$  relaxation rate. For T1 measurements, the signal model was  $s(TR_i) = s_{TR=\infty} (1 - e^{-TR_i R_1})$ . In both models, the non-linear optimization routine solved for the spin density  $s_{t=\{0,\infty\}}$  and the corresponding relaxation rate.

Signal intensities in each sample were measured using a custom software user interface (also developed in MATLAB). The software allowed all DICOM images corresponding to a single experiment to be loaded, and regions-of-interest (ROIs) to be placed in any source axial slice in the image volume of one acquisition. The

software then propagated the ROI to the corresponding slice and location in every acquisition in the experiment, thereby producing the average signal measurement for that ROI across the corresponding independent variable. ROIs were placed at the center of each vial for each solution concentration in at least 4 different axial slices covering the vial. The fitted relaxation times were recorded into Excel and averaged over the multitude of ROIs collected for each vial. A least squares linear fit was finally used to calculate the agent relaxivity ( $r_1$ ,  $r_2$ ) as the slope of a straight line corresponding to the measured relaxation rates ( $R_1$ ,  $R_2$ ) vs. known iron concentration values of each vial. Standard error in the slope was also estimated from this output. Plotting of all the results was done in R (version 3.5.1) using ggplot2.

### *LIVE/DEAD Assay*

A LIVE/DEAD assay was performed as recommended to assess cytotoxicity of functionalized SPIONs. Briefly, HUVECs were cultured as recommended on tissue-coated plastic. When cells were visibly confluent, enough SPION solution to reach a concentration of 100 parts per million (ppm) was diluted in standard cell media and added to the HUVECs. SPIONs were incubated with cells at 37°C for 2 hours. Cells were rinsed with sterile PBS and stained as proscribed in the LIVE/DEAD kit protocol, with optimal concentrations of 1 $\mu$ M Calcein AM and 2 $\mu$ M Ethidium homodimer-1 having been previously determined in other HUVEC

samples. Cells were imaged on an Olympus IX81 microscope using appropriate fluorescent filters. Live and dead cells were quantified using ImageJ, and subsequent statistical analysis were performed in R.

### *Hydroxyapatite Nucleation and Formation Studies*

Similarly to the protocols previously described, this protocol was adapted from work by de Bruyn et al.<sup>100</sup> Two working solutions were prepared in advance (0.5M CaCl<sub>2</sub> and 0.25M Na<sub>2</sub>HPO<sub>4</sub>). On the day that measurements were performed, these solutions were diluted in either DI water or 50% serum to 12mM CaCl<sub>2</sub> and 7.5mM Na<sub>2</sub>HPO<sub>4</sub>, respectively, and the pH of all solutions was adjusted to 7.4. These solutions were mixed in a 1:1 ratio. SPION samples or peptides were added such that the additional solution made up 1/10<sup>th</sup> the volume of the total solution, keeping concentrations of either SPIONs or peptides consistent across experiments. Mixed solutions were measured every 4 minutes for a total of 40 minutes via DLS, as previously described. Control solutions were solutions where sodium phosphate buffer was added instead of either SPION samples or peptides. Sodium phosphate buffer was chosen as the control for these studies because SPIONs remain suspended in sodium phosphate buffer after fabrication is complete.

### *Nanoparticle Endothelial Translocation Studies*

HUVECs were cultured at recommended conditions in T-75 flasks. When cells were 80% confluent, they were split into 0.4 $\mu$ m pore size, poly(ethylene) (PE) membrane transwells. Cells were cultured on the transwell membranes until they reached confluence, as determined by observation of the cell layer under a microscope and confirmed by TEER. TEER measurements were performed using an EVOM2 from World Precision Instruments. A schematic representing the sequence of events in the nanoparticle translocation studies is below (**Figure 4.2**).

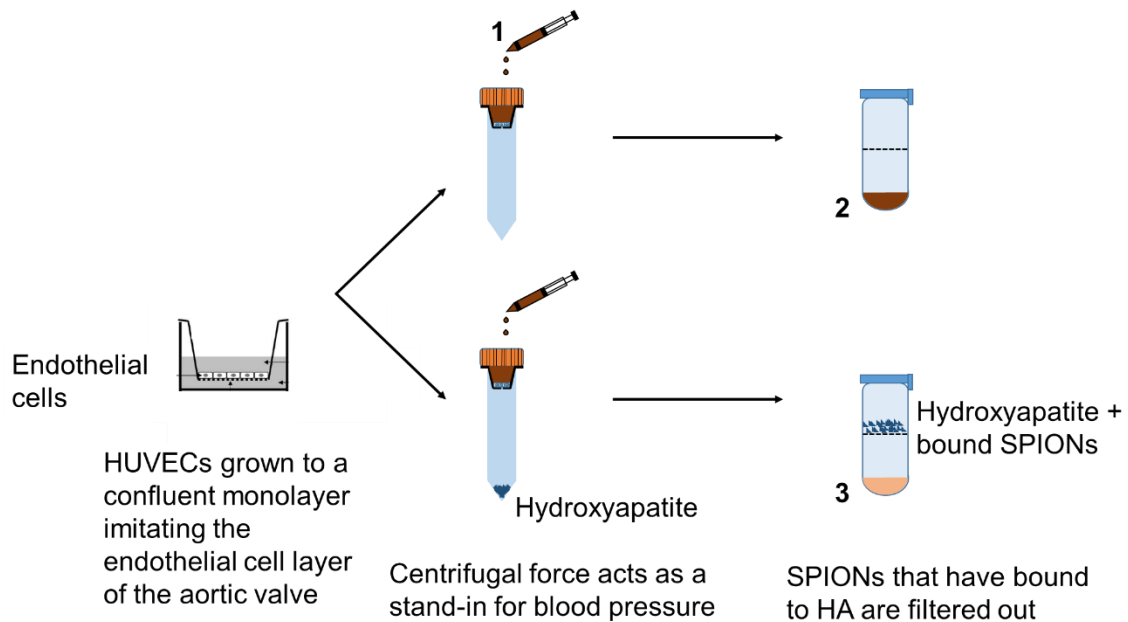


**Figure 4.2:** Schematic of transwell experimental setup. Briefly, HUVECs are grown to a confluent monolayer on transwell membranes. The transwell membranes are loaded into centrifuge tubes, and solution containing nanoparticles is loaded into the top compartment (1). Some centrifuge tubes are pre-loaded with HA in the bottom compartment as labeled in the figure to measure binding to HA, while some do not so that translocation alone can be assessed. Following centrifugation, nanoparticles that have passed through the endothelial layer are in the bottom of the centrifuge tube (not shown). The entire solution in the bottom of the centrifuge tube is loaded into a filter centrifugation tube, so that any HA that may have been present can be filtered out. The solution that passes through this second filtration represents the nanoparticles that have passed through the endothelial membrane (2) and for tubes that contained HA, contains the SPIONs that remain unbound to the HA (3).

For all nanoparticle translocation studies, all media was removed from the transwell inserts, and they were placed into 15mL conical tubes. For studies involving binding to HA, 10mg of HA was first deposited in the bottom of each conical tube via the addition of appropriate quantities of prepared, sterilized 0.5M  $\text{CaCl}_2$  and 0.25M  $\text{Na}_2\text{HPO}_4$  solutions. These solutions were allowed to evaporate completely prior to translocation studies. Nanoparticles (HABP-, OPN-, or PEG-

SPIONs) were loaded at a concentration of 200ppm in 50% serum into the transwell inserts, and the conical tubes were sealed by parafilm. The conical tubes were centrifuged at 2500rpm (1258 x g) for 10 minutes. Samples were agitated and allowed to incubate for 30 minutes after centrifugation. Liquid that passed through the transwell membrane was collected from the bottom of the conical tube, and loaded into 0.4µm Costar Spin-X centrifuge tubes. These samples were centrifuged at 3000rpm for 5 minutes to remove any HA and HA-bound SPIONs from the sample. To assess the concentration of nanoparticles remaining in solution subsequent to these tests, the absorbance of the filtered liquid was measured at 410nm, and compared to a concentration curve comprising known concentrations of HABP-, OPN-, or PEG-SPIONs in 50% serum solution.

#### *Binding Studies in Excised Human Aortic Valve Samples*

Excised valves from control samples (i.e. from donors who had not been diagnosed with AS) were obtained from the NDRI as formalin-fixed, paraffin-embedded tissue. Portions of the tissue were deparaffinized in several washes of xylene and rehydrated in ethanol and water. Samples were blocked with 50% FBS before being incubated with SPIONs for 30 min. After exposure to SPIONs, samples were stained with Prussian blue stain for 35 min, and images of the samples were captured. After Prussian Blue staining, some samples were stained with silver nitrate using the Von Kossa method as well, as described.<sup>176</sup> The Von

Kossa method relies on the reaction between silver ions and phosphate in the presence of acid, whereby the phosphate may be replaced by silver deposits, visualized as black/grey in color. Images of stained samples were collected via an iPhone camera and processed in ImageJ.

Portions of non-diseased samples were sliced and mounted on slides. Slides were deparaffinized immediately prior to staining, as has been previously described<sup>177</sup> using a series of xylene and ethanol washes. For alizarin red staining, samples were incubated for 2 minutes with Alizarin Red solution, following which they were washed several times with acetone. For nanoparticle binding studies, samples were washed in DI water and incubated for 30 minutes with diluted nanoparticle solution in 50% FBS. The remaining nanoparticles were washed off with DI water, following which slides were incubated with Prussian Blue solution (a 1:1 mix of 5% potassium ferrocyanide and 5% HCl).

Images of stained slides were collected via an Eclipse Ni-E microscope and assessed in ImageJ.

### **4.3 Results**

Based on optimization results described in Chapter 3, all studies in this chapter were performed on 10nm core SPIONs with PEG brush chain lengths of 3.4k, PEGylated using method 2 (ligand exchange with citric acid, followed by the

addition of NH<sub>2</sub>-PEG via EDC/NHS chemistry) as these SPIONs showed the maximal MR signal in previous studies.

### *MR Measurements*

As with the addition of PEG chains of different lengths, the addition of peptides to PEG has a marked impact on the MR signal, and in particular, on  $r_2$  (**Figure 4.3**). For CPMG-derived relaxivities, the MR signal for HABP-SPIONs is, on average, greater than that of either OPN- or PEG-SPIONs. However, the  $r_1$  trends are different, showing that PEG-SPIONs have a greater  $r_1$  signal than either HABP- or OPN-SPIONs. Importantly, differences between HABP- and OPN-SPIONs were observed. This indicates that, not only does the addition of a peptide impact the MR signal of the resulting particles, but also that the type and qualities of the peptide added impact the MR signal as well.

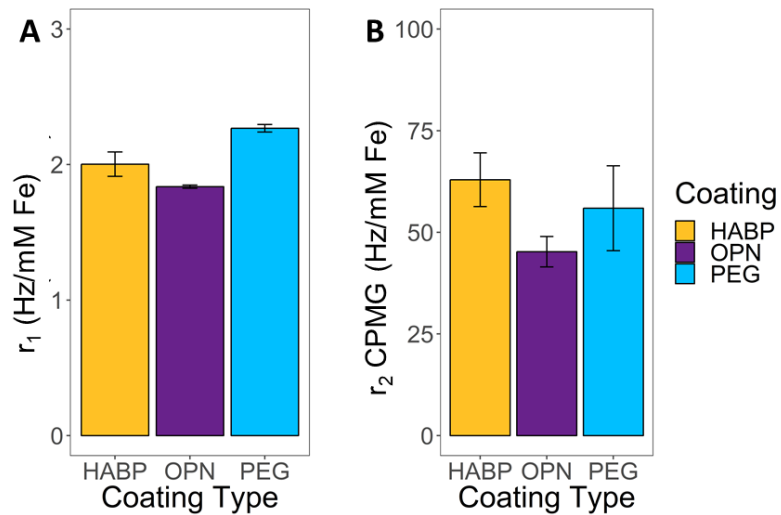


**Figure 4.3:** MR results showing the measured signal differences between HABP-, OPN-, and PEG-SPIONs under non-binding conditions. Each bar represents the slope of a line over 5 different SPION samples at different concentrations, as calculated by using the least squares method to calculate the statistics for a straight line corresponding to the measured signal vs. known iron concentration values. The slope of this line corresponds to the relaxivity for the sample. Error bars represent standard error in the calculation of this slope. Signal measured is **(A)**  $r_1$  **(B)** CPMG-derived  $r_2$ .

The MR properties of unbound vs. bound SPIONs were assessed to determine if there was a measurable signal difference between the two (**Figure 4.4**). Binding of SPIONs to HA is expected to yield increased relaxivities. Results generally indicated that bound HABP-SPIONs did exhibit higher relaxivities than unbound HABP-SPIONs, while OPN-SPIONs did not show a consistent trend. This confirms that HABP-SPIONs do bind to their HA target, and that this binding can be observed via MR. The error on these samples is notably higher than those in other samples tested in Chapter 3 and **Figure 4.3**, likely because these samples needed to be mixed into a gel-like solution to keep the HA suspended for the duration of the image scans. The lower magnitude of the relaxivities in comparison to other

samples tested in Chapter 3 and **Figure 4.2** is also likely due to the gel-like nature of the suspension, which would naturally have a lower water content and lower water mobility than the samples that were previously tested.

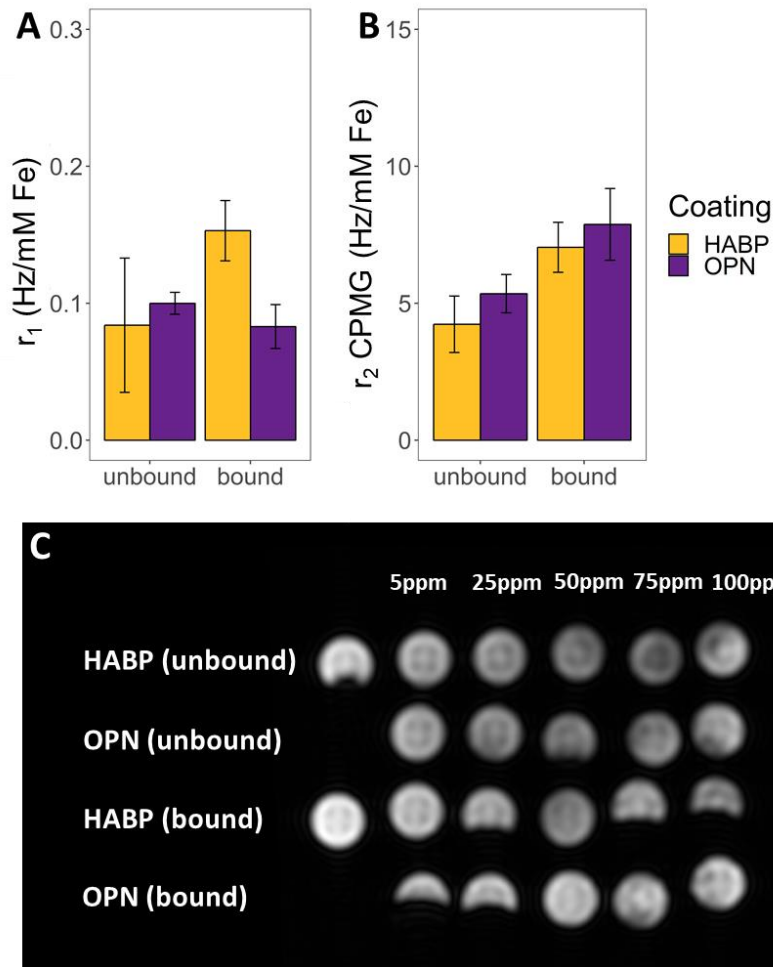


**Figure 4.4:** MR results showing the measured relaxivity differences between unbound (left) and bound (right) particles for both HABP-SPIONs (orange) and OPN-SPIONs (purple). Each bar represents the slope of a line over 5 different SPION samples at different concentrations, as calculated by using the least squares method to calculate the statistics for a straight line corresponding to the measured signal vs. known iron concentration values. The slope of this line corresponds to the relaxivity for the sample. Error bars represent standard error in the calculation of this slope. Signal measured is **(A)**  $r_1$  **(B)** CPMG-derived  $r_2$ . **(C)** Raw  $T_2$  weighted image.

However, as discussed by Caravan, et al., with a longer correlation time as in for the bound nanoparticles,  $r_2$  is expected to increase more than  $r_1$ ; i.e.  $r_2/r_1$  will increase from unbound particles to bound particles.<sup>178</sup> While this is true for OPN-SPIONs (unbound  $r_2/r_1 = 33.57 \pm 6.67$ ; bound  $r_2/r_1 = 56.73 \pm 12.05$ ), these results were inconclusive for HABP-SPIONs (unbound  $r_2/r_1 = 50.39 \pm 29.44$ ; bound  $r_2/r_1 = 46.03 \pm 8.95$ ). The high error, as previously noted, may be due to incomplete mixing of the samples, as is also evidenced by the image of an MRI slice provided in **Figure 4.4C**.

#### *LIVE/DEAD Assay*

The specific cytotoxicity of functionalized SPIONS in HUVECs was examined via a LIVE/DEAD assay (**Figure 4.5**).<sup>62</sup> HUVECs were chosen for these studies because SPIONs entering the body via injection are most likely to encounter endothelial cells. After incubation with various functionalized SPIONs, samples that had been incubated with HABP-, OPN-, and PEG-SPIONs did not show significantly higher rates of cell death than control samples ( $p > 0.05$ ).

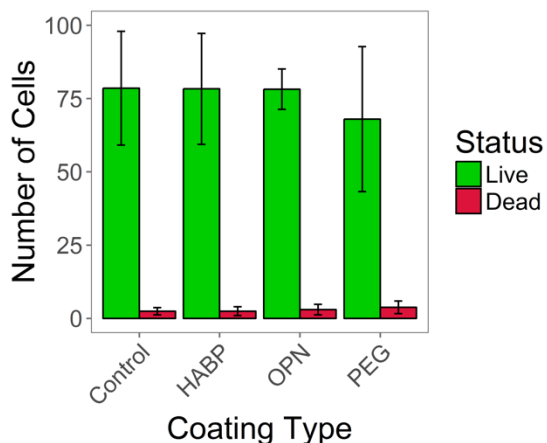


**Figure 4.5:** Results from a LIVE-DEAD assay indicating that HABP-, OPN-, and PEG-SPIONs do not demonstrate significant ( $p < 0.05$ ) toxicity to HUVECs after incubation. The incubation of HUVECs HABP-, OPN-, and PEG-SPIONs for 2 hours does not lead to increased cytotoxicity when compared to the control. For these studies, error bars are standard deviation and  $n=3$ .

#### *Hydroxyapatite Nucleation and Formation Studies*

The impact of functionalized SPIONs on HA nucleation and formation was assessed (**Figure 4.6**). Results in buffer solution with HABP and OPN peptides alone (unconjugated to SPIONs) indicated that the OPN peptide has an inhibitory effect on the nucleation and formation of HA nanocrystals (**Figure 4.6A**). There is no significant difference between the control sample and HABP peptide alone ( $p > 0.05$ ); however, there was a significant difference between the control sample and the OPN peptide ( $p < 0.05$ ). This result was expected based on previous research which described similar effects of OPN. When HABP and OPN were conjugated onto SPIONs, however, this effect was not observed (**Figure 4.6B**). Instead, buffer solutions with either HABP- and OPN-SPIONs showed potentially more rapid nucleation and formation of HA nanocrystals, with significantly larger crystals observed at almost every timepoint except at 24 and 40 minutes ( $p < 0.05$ ).

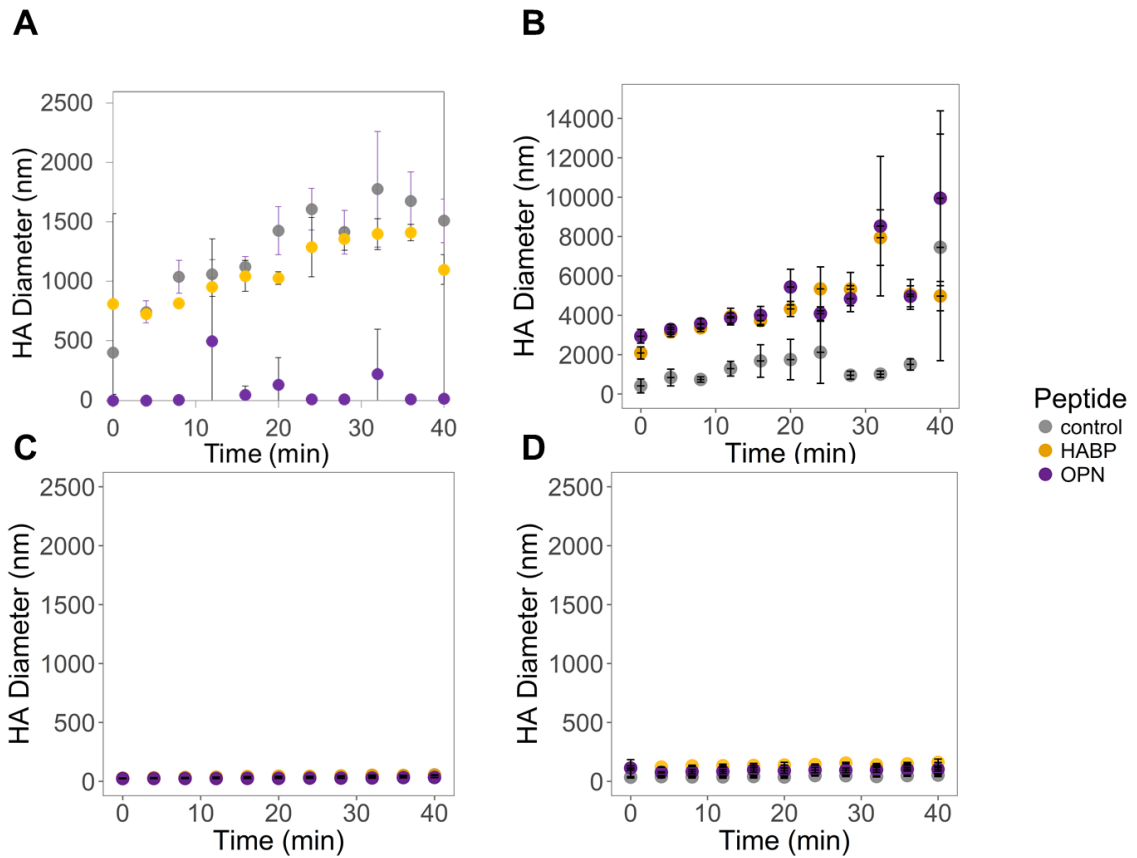


**Figure 4.6:** Examination of the impact of HABP- and OPN-SPIONs on HA nucleation and formation *in vitro*. HA nucleation and the formation of nanocrystals was measured over 40 minutes via DLS, and the impacts of the presence of **(A)** HABP and OPN peptides alone in buffer, **(B)** HABP- and OPN-SPIONs in buffer, **(C)** HABP and OPN peptides alone in 50% serum, and **(D)** HABP- and OPN-SPIONs in 50% serum were evaluated.

However, neither of these trends were observed in samples containing 50% serum (**Figure 4.6 C and D**). In the presence of 50% serum, there were no observable or quantifiable differences in HA nucleation and formation in samples containing HABP and OPN peptides, or in samples containing HABP- and OPN-SPIONs, in

comparison to the control, where only sodium phosphate buffer has been added. Serum in general appears to prohibit HA nucleation and formation.

### *Nanoparticle Endothelial Translocation Studies*

The ability of functionalized SPIONs to pass through an endothelial layer was assessed via the setup shown in **Figure 4.7**. Briefly, HUVECs are cultured on 0.4µm PE transwell membranes until confluent. Confluence was confirmed by transepithelial electrical resistance measurements (TEER), which was calculated using the equation:  $TEER_{reported} = (\Omega_{cell\ sheet} - \Omega_{transwell}) \cdot area$ . These calculations yielded a TEER measurement of  $18.4 \pm 1.9 \Omega\text{cm}^2$ , which is in keeping with results from the literature indicating that confluence for HUVECs on transwell membranes is considered to correspond to a range of TEERs between 10-20  $\Omega\text{cm}^2$ .<sup>179–181</sup>

For centrifugation through the epithelial layer and transwell membrane in the center step, calculations were performed to determine a centrifugation speed that would come close to, but not exceed, the pressure that would be experienced by particles under blood flow conditions. Those calculations are shown below (**Figure 4.7**). It was determined from these calculations that 2500 rpm, or 1258 x g was an appropriate rate of centrifugation.

### Blood Pressure Calculation

Diastolic blood pressure = 80mmHg



Conversion to SI units = 10,666 Pa

### Transwell Pressure Calculation

$$F_{net} = ma$$

*m* = mass of the liquid in the transwell

*a* = acceleration due to centrifugation

$$F_{net} = (2 \times 10^{-4} \text{ kg}) \left( 1258 \frac{\text{m}}{\text{s}^2} \right) = 0.2516 \frac{\text{kg} \cdot \text{m}}{\text{s}^2}$$

$$\text{Pressure} = \frac{F_{net}}{\text{area}}$$

area = area of transwell membrane

$$\text{Pressure} = \frac{0.2516 \frac{\text{kg} \cdot \text{m}}{\text{s}^2}}{0.33 \text{ cm}^2} = \text{7624 Pa}$$

**Figure 4.7:** Comparison of forces generated by blood flow to those generated by centrifugation on the endothelial layer growing on a transwell membrane. The force generated by centrifugation approaches that of the pressure on the valve during diastole without exceeding it, meaning that this rate of centrifugation is appropriate for the experiments described.

The absorbance of samples in the transwell setup is measured at several steps throughout the process to evaluate the concentration of nanoparticles at each step. Each step at which the absorbance is measured is indicated by a number in **Figure 4.2**, and has a corresponding labeled bar in **Figure 4.8A**. To summarize, nanoparticle concentrations were measured upon initial placement of 200ppm of particle solution into the transwell apparatus (#1), and then after the second round of centrifugation both for samples not containing HA (#2), and for samples containing HA (#3). A concentration curve for each type of nanoparticle tested was generated to correlate concentration of nanoparticles with absorbance.

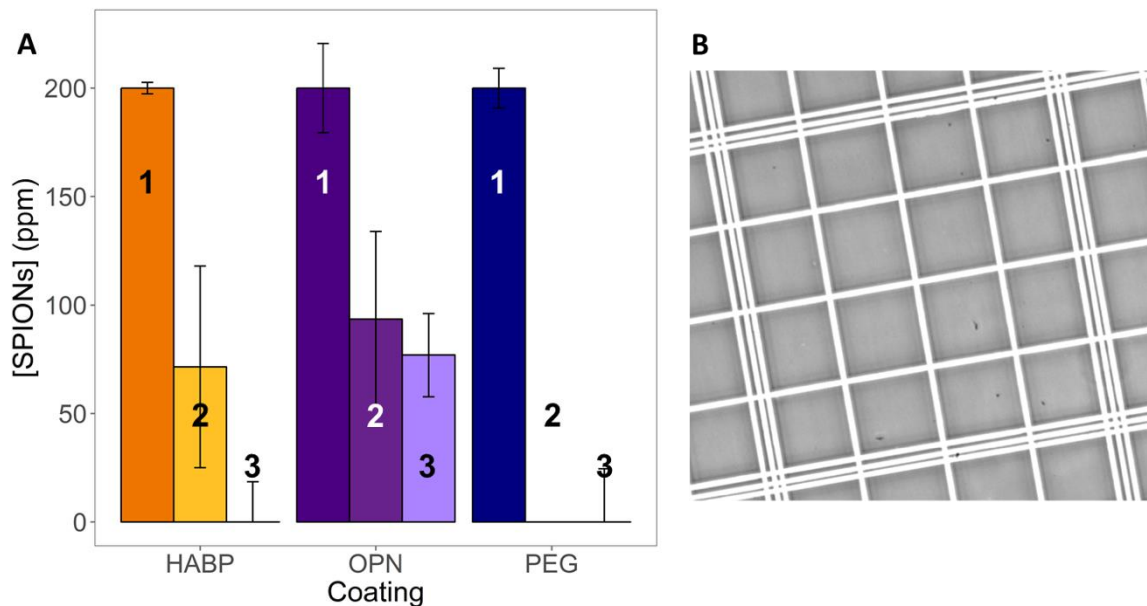


**Figure 4.8: (A)** Results from transwell experiments depicted in Figure 4.4. Results indicate the concentration of SPIONs added into the transwell compartment (rightmost bar for each coating type), the concentration of SPIONs in the solution that has been centrifuged through the endothelial layer on the transwell membrane (middle bar), and the concentration of SPIONs remaining after binding to HA has been allowed to occur (leftmost bar). Statistical significance ( $p < 0.05$ ) is indicated by \*, error bars are standard deviation, and  $n=3$ . **(B)** Example image of hemocytometer after loading with fluid centrifuged through the endothelial layer on a transwell membrane, indicating that there are no dead (or live) cells that have been forced through the transwell membrane.

Results in **Figure 4.8A** indicated that both HABP- and OPN-SPIONs are able to pass through the endothelial barrier and the transwell membrane (**#2**, orange and purple bars). The concentration of HABP-SPIONs remaining in the solution that has passed through the endothelial barrier is significantly less than the starting concentration of 200ppm ( $p < 0.05$ ); on average, 35.7% of HABP-SPIONs pass through during centrifugation. Likewise, the concentration of OPN-SPIONs remaining in the solution that has passed through the endothelial barrier is

significantly less than the starting concentration of 200ppm ( $p < 0.05$ ); on average, 46.7% of OPN-SPIONs pass through during centrifugation. The difference between the concentrations of the HABP- and OPN-SPIONs that passed through the endothelial barrier was not significant ( $p > 0.05$ ). PEG-SPIONs, on the whole, appear unable to pass through the endothelial barrier (#2, blue bar).

The ability of functionalized SPIONs to bind to HA after passing through the endothelial barrier was also assessed (#3). In samples where HA was loaded into the centrifuge tube, so that any material that passed through the endothelial barrier would be allowed to bind to the HA, the measured concentration of HABP-SPIONs in the final solution was significantly less than the concentration of samples with no HA in the bottom of the centrifuge tube ( $p < 0.05$ ). The average concentration of SPIONs decreased from ~71.5 to ~0ppm. However, the concentrations of OPN-SPIONs between these two samples did not significantly alter ( $p > 0.05$ ), though the average concentration again decreased from ~93.5 to ~76.9ppm. There was no significant difference between these two sets of samples for PEG-SPIONs ( $p > 0.05$ ).

The solution that passed through the endothelial barrier and transwell membrane was additionally assessed via hemocytometer to determine if any live or dead cells were passing through the membrane (**Figure 4.8B**). As expected, no evidence of live or dead whole cells was observed, indicating that, unlike nanoparticles, cells were not able to pass through the transwell membrane.

### *Binding Studies in Excised Human Aortic Valve Samples*

Human aortic valve samples were obtained from the NDRI as formalin-fixed, paraffin-embedded sections. These samples were obtained from deceased tissue donors, as well as donors who had the aortic valve removed as part of a SAVR procedure. Donors were all over 60 years of age, and were comprised of both men and women. Limited information was available for each individual donor, as tissues were de-identified in keeping with an exemption letter obtained from Boston University's Institutional Review Board.

Stenotic tissue could not be sliced using a microtome. Therefore, to perform comparable studies on both diseased and non-diseased samples, tissue samples were cut into sections, and the sections were incubated with 50% FBS (to block non-specific binding) and functionalized SPIONs before washing and staining with Prussian Blue to visualize areas where SPIONs had deposited (**Figure 4.9**). Subsequent to Prussian Blue staining, samples were stained using the Von Kossa method to observe any colocalization between the stains. Sections of normal tissue were also prepared similarly in order to observe any visible off-target binding. While microscopic calcium or HA deposits may be observed in non-diseased tissue, macroscopically-visible deposits were not expected.

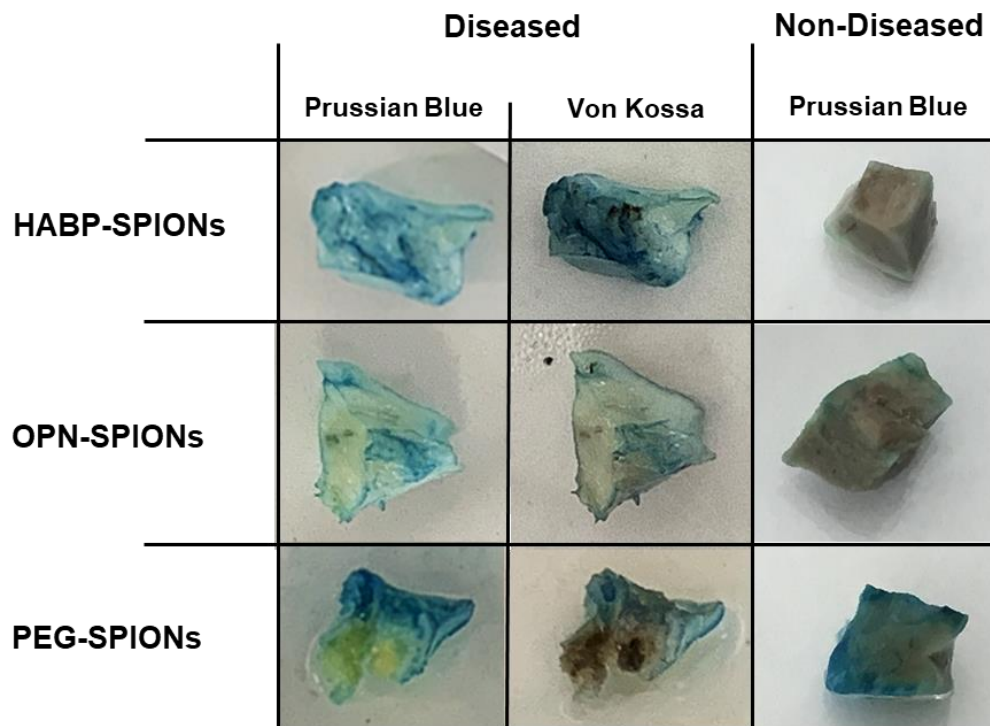


**Figure 4.9:** Selected images from experiments looking at binding of HABP-, OPN-, and PEG-SPIONs to both diseased valve samples and normal tissue. Nanoparticle binding is indicated by the blue color due to Prussian Blue staining for iron. Von Kossa staining for calcium is indicated by dark grey-black areas. All tissue samples were incubated with 50% serum prior to the addition of nanoparticles. While all particles showed some degree of binding to diseased valve tissue, PEG-SPIONs also showed substantial off-target binding to normal tissue.

Results from these studies indicated that HABP-, OPN-, and PEG-SPIONs all show visible binding to diseased valve samples (see the blue/green color in the first column of **Figure 4.9**). This is perhaps unsurprising, given the results demonstrated in Chapter 2. It is worth restating that PEG-SPIONs showed substantial binding to cholesterol in the studies discussed in Chapter 2; diseased valve tissue would be expected to have cholesterol deposits in addition to HA deposits, so the binding of PEG-SPIONs to diseased valve tissue may be expected.

After incubation with nanoparticles and staining with Prussian Blue, samples were also stained using the Von Kossa method (see grey-black color in the second column **Figure 4.9**). The Von Kossa method was chosen for this application because there is no cross-reaction with iron. The colocalization of the Prussian Blue and Von Kossa stains, which would indicate that the SPIONs are binding to calcium-phosphate deposits in the diseased tissue, was observed primarily in HABP-SPIONs, where the blue color from the Prussian Blue stain was overlaid with a darker grey-black stain. OPN-SPIONs also showed some colocalization as well, but qualitatively, not as strongly as the HABP-SPIONs. PEG-SPIONs showed some colocalization, but also a significant amount of off-target binding, as evidenced by the large grey and black deposits in an area of the sample that exhibited no blue staining. PEG-SPIONs also showed visibly detectable binding to non-diseased samples, while OPN-SPIONs showed less off-target binding, and HABP-SPIONs did not show appreciable off-target binding.

Similar experiments with Prussian Blue staining were repeated across 3 different samples, with 3 replicates for each sample tested. Results across all experiments were collected and scored on a scale from 1-5, with 1 meaning “No visible blue stain” and 5 meaning “Substantial blue deposits.” These results were all put into a heat map (**Figure 4.11A**), and averaged across runs for easier visualization (**Figure 4.11B**). These results confirmed observations from **Figure 4.10** that, while HABP-, OPN-, and PEG-SPIONs all demonstrate some degree of binding to diseased samples, off target binding is observed strongly with PEG-SPIONs,

weakly with OPN-SPIONs, and to a very small degree with HABP-SPIONs. In addition, HABP-SPIONs bind more consistently to diseased samples than either OPN-SPIONs or PEG-SPIONs.

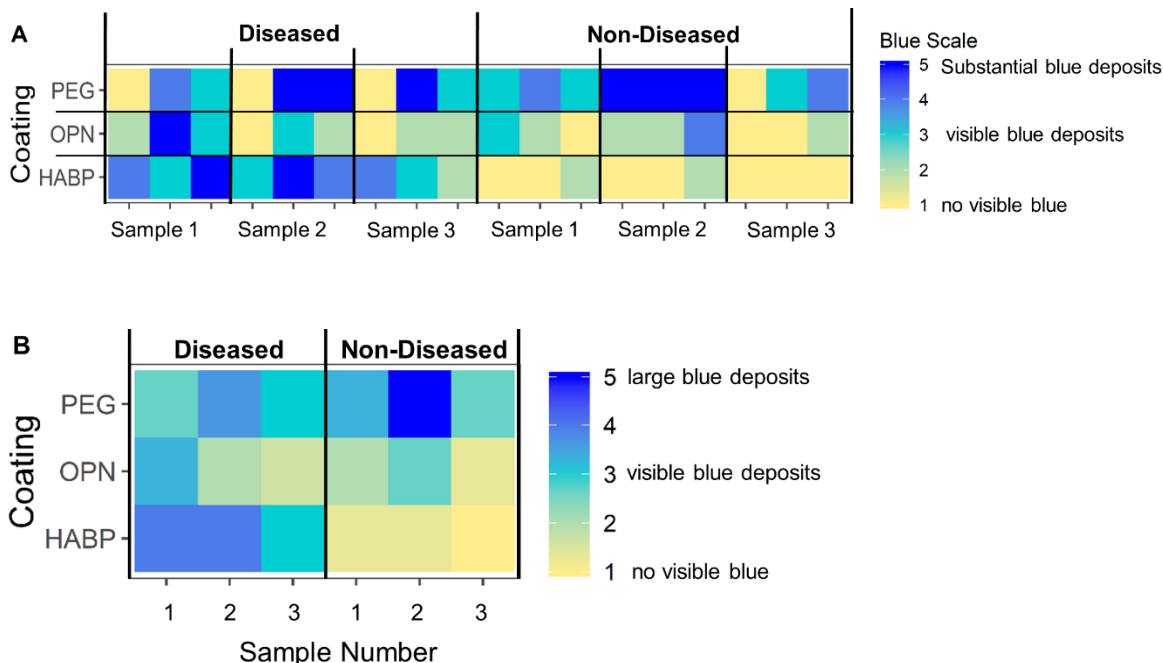


**Figure 4.10:** Heat map representation of experiments testing binding of SPIONs to excised human aortic valve samples. Darker blue shading corresponds to more observed binding. **(A)** Representation of all results across all replicates, and **(B)** representation of results averaged across replicates for easier visualization.

Because of these results, HABP-SPIONs alone were selected for further study using additional methods. With the remaining non-diseased samples, we were able to mount slices of tissue sections onto microscope slides. Although these non-diseased samples did not show macroscopic evidence of calcium deposits, it is feasible or even likely that microscopic calcium deposits may be observed because the age of all donors was >60 years old. To test this, and to determine if these

microcalcifications could be detected by HABP-SPIONs, two consecutive tissue slices were mounted on a single slide, allowing separate stains to be performed on each slice. One slice was exposed to HABP-SPIONs and stained with Prussian blue; the other was stained with Alizarin red, which stains calcium deposits red. Alizarin red was chosen for these studies because the resulting red color was more readily isolated via a simple red light filter. Co-staining of a single slice was not useful in these studies because Alizarin red cross-reacts with iron. These slices were imaged with a color microscope, allowing separation of the color channels (i.e. isolation of the blue channel to isolate Prussian blue stain, isolation of the red channel to isolate Alizarin red stain). False-color images for ease of visualization are provided in **Figure 4.11A** and **B**, indicating a very similar stain pattern and, potentially, visible microcalcifications.

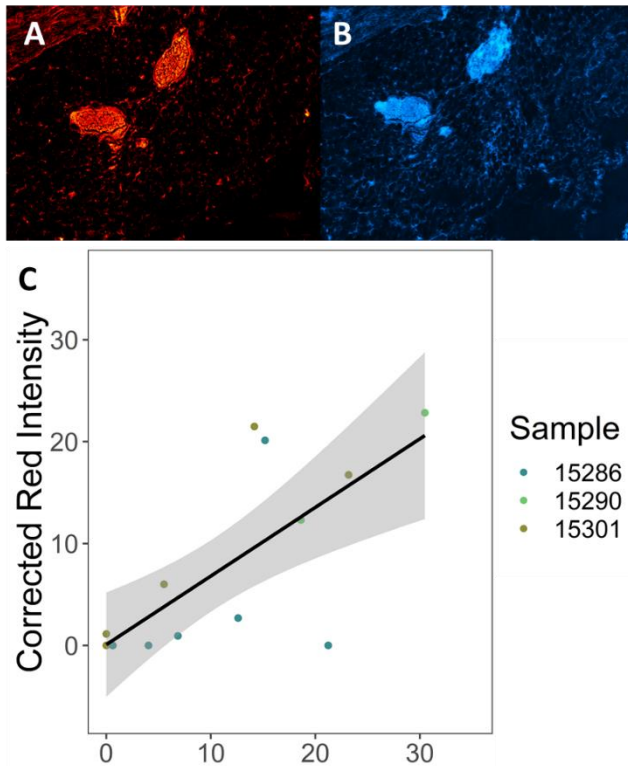


**Figure 4.11:** (A) Microscope image of non-diseased valve sample stained with Alizarin Red at magnification 4x. The red channel of the original image was isolated and false colored in ImageJ for ease of visualization. (B) Microscope image of non-diseased valve incubated with HABP-SPIONs and stained with Prussian blue at magnification 4x. The blue channel of the original image was isolated and false colored in ImageJ for ease of visualization. (C) Quantification of red intensity vs. blue intensity for paired valve slices stained with Alizarin Red (y axis) vs. Prussian blue (x axis) to visualize correlation between red and blue stain in paired samples. A simple linear regression was performed (black line), and the grey shading indicates the 95% confidence interval.

Several staining procedures were performed on remaining non-diseased tissue, and the quantity of red stain in Alizarin red-stained slices was compared with the quantity of blue stain in Prussian blue-stained slices for each pair of slices mounted on a single slide. Stain quantifications were performed using ImageJ. Results from this comparison are in **Figure 4.11C**. A linear regression was performed, indicating a significant positive trend and strong correlation, with  $R = 0.72$  and  $p = 0.0016$ . Although these results are preliminary, this correlation provides good evidence that HABP-SPIONs may additionally be able to detect microcalcifications in early-stage CAVD.

#### **4.4 Discussion**

Understanding the medically-relevant properties of HA-SPIONs is key to their application as a contrast agent for early CAVD detection. To this end, the medical relevance of functionalized SPIONs was assessed on several fronts, including the MR contrast they generate, their cytotoxicity to endothelial cells, their interaction with and impact on HA nucleation and formation, their ability to pass through an endothelial layer and bind to HA subsequently, and their ability to detect HA deposits in excised human aortic valve samples.

Previous results discussed in Chapter 3 indicated that relaxivities for SPIONs could be optimized by adjusting the chemical and physical properties of the SPIONs. However, these results did not account for differences in relaxivity caused by the addition of peptides. **Figure 4.3** indicates that the addition of peptides does further impact the measured relaxivities, and that this impact actually depends on the nature of the peptide itself. The differences observed between the relaxivities of HABP- and OPN-SPIONs could be due to several factors, including the differences in peptide properties listed in **Table 2.2**. Notably, the number of hydrophobic residues is much higher for HABP (6 residues) than for OPN (1 residue). As observed with differences between relaxivity with different methods of PEGylation in Chapter 3, the hydrophobicity or hydrophilicity of groups close to the SPION core may make a substantial difference in the MR properties of the resulting SPIONs. However, unlike in Chapter 3, where hydrophobic groups close to the

core resulted in lower MR signal, here we observe that a hydrophobic peptide attached to the PEG actually increases  $r_1$  and  $r_2$ . It is hypothesized that, while a hydrophobic moiety closest to the core prevents water from approaching close to the core, a somewhat hydrophobic moiety partially surrounding the hydrophilic moiety closest to the core may actually serve to trap water molecules in close proximity to the core. Alternatively, or additionally, it is possible that some degree of aggregation of HABP-SPIONs plays a role in their increased relaxivity. As discussed in Chapter 3, HABP-SPIONs fabricated to have ~100 peptides/SPION aggregated immediately and dropped out of solution; perhaps a smaller amount or degree of aggregation is occurring in all HABP-SPIONs. Further studies would be needed to determine the precise cause of the signal enhancement observed in HABP-SPIONs.

The impact of binding to HA on relaxivities was also assessed (**Figure 4.4**). In general, previous research has demonstrated that bound particles exhibit increased relaxivities. Bound particles move through water more slowly, thus giving water molecules more time on average close to the core and increasing the apparent relaxivity. As expected, bound HABP-SPIONs did demonstrate increased relaxivity in comparison to unbound particles, thus confirming particle binding via an additional method orthogonal to those used in Chapter 2. However, OPN-SPIONs did not. On the other hand, OPN-SPIONs exhibited the expected increase in  $r_2/r_1$ , while results for HABP-SPIONs were inconclusive. It is hypothesized that this inconsistency may have been due to the incomplete sample mixing visible via

MRI and caused by the gel-like nature of the HA suspension. Although the method of mixing used in these experiments showed the best results of any method attempted thus far, samples still failed to mix completely. In the future, it may be beneficial to perform imaging on bound SPIONs that are not suspended in liquid, although it may be difficult to obtain relaxivities from these kinds of experiments.

The gel-like matrix necessary to suspend HA for the necessary length of time to perform MR measurements severely impacted the resulting relaxivities, and potentially the magnitude of the error. It is also hypothesized that the error may be high because not all nanoparticles were bound to HA upon testing; as HA was added to the gel prior to the addition of particles in order to facilitate mixing of the gel and consistent suspension of the HA, it is possible that not all particles added subsequently were bound to HA (i.e. incomplete mixing between HA and SPIONs may have been an issue). However, studies performed where all of the particles were bound to HA prior to the addition of the HA-particle complexes to the gel (data not shown) showed even higher error and visible failure to mix, even after 24 hours of vigorous agitation. Thus, even though particle binding may have been incomplete, the methods used to produce the data shown in **Figure 4.4** are preferable. However, because incomplete binding may have been an issue, we cannot say quantitatively that these relaxivities represent those that could be observed under 100% bound conditions. Instead, we conclude that examining the qualitative trends in the data (i.e. that bound HABP-SPION particles generally exhibited higher MR signal than unbound HABP-SPION particles) indicates

successful binding of both HABP-SPIONs to HA.

Cytotoxicity studies performed confirm what has been previously shown in the literature: that polymer-coated and functionalized SPIONs are not cytotoxic, and are generally safe for biological use at physiologically-relevant concentrations (**Figure 4.5**).<sup>98,115,182</sup> Although this was demonstrably true in HUVECs after 2 hours of incubation, the effects of repeated exposure were not assessed in this system. Additionally, broader effects of exposure, as previously described by Singh et al., have not yet been assessed for these particular SPIONs.<sup>165</sup> Therefore, future experiments will need to address issues of systemic toxicity and repeated exposure.

Because functionalized SPIONs bind to HA, as demonstrated both in Chapter 2 and **Figure 4.4**, it is possible that they have an impact on HA nucleation and formation. This is particularly true because previous research has demonstrated that the OPN peptide alone, as discussed previously, can disrupt HA crystal formation. Although in calcific deposits found in CAVD this disruption may be an advantage, the functionalized SPIONs are expected to show some degree of off-target binding to bone throughout the body, where the potential disruption of HA crystal formation and deposition may have negative physiological impacts. Bone mineral in the body is consistently undergoing resorption and redeposition processes, and interfering with these processes is thought to play a role in diseases such as osteoporosis.<sup>73,166</sup>

However, while the OPN peptide alone did, as expected, slow HA nanocrystal nucleation and formation, both HABP- and OPN-conjugated SPIONs actually seemed to increase the rate of HA nanocrystal nucleation and formation in buffer (**Figure 4.6**). This could also lead to a variety of negative physiological impacts. Fortunately, this effect was limited to buffer-only solution; upon the addition of 50% serum, it was observed that HABP and OPN peptide alone, in addition to HABP- and OPN-SPIONs, showed no difference from the control in terms of HA nanocrystal nucleation and formation (**Figure 4.6**). This indicates that addition of particles may not have theranostic applications, but also that they are safe for systemic administration.

Evaluating the ability of SPIONs to pass through an endothelial barrier and still bind to HA is a particularly important set of experiments, given that the small HA deposits present in early CAVD are largely present underneath the epithelium of the aortic valve. Although it is possible to use a transwell setup to examine the diffusion of particles through an endothelial layer, as has been described in many previous studies, in these studies we wanted to recapitulate, to whatever degree possible, the forces that will act on the particles as they are under the pressure of blood flow. To this end, a centrifuge speed was chosen as previously described to approach, but not exceed the pressure that would be experienced by particles in the bloodstream, especially given that it is likely that the endothelial barrier *in vivo* will exhibit higher integrity than the *in vitro* endothelial layer on the transwell membrane. Although TEER measurements are not typically performed *in vivo*,

estimates of TEER values up to or over 1000  $\Omega\text{cm}^2$  have been reported from various cell types in different barrier models.<sup>183–185</sup> However, it has also been well-established that the presence of inflammation or inflammatory cytokines, such as those present in CAVD, does decrease the barrier function of endothelial cells.<sup>183,186,187</sup> Thus, although the transwell apparatus and the HUVECs used for these studies may not recapitulate precisely the barrier function of valvular endothelial cells, they may serve as an adequate stand-in for the evaluation of endothelial function under the inflammatory conditions present in CAVD and AS.

Results from these transwell experiments indicated that HABP- and OPN-SPIONs both successfully passed through the endothelial layer and transwell membrane upon centrifugation (**Figure 4.8**). As expected, not all of the particles passed through. However, the rates of passage were comparable for both HABP- and OPN-SPIONs, and were far greater than the rates of passive diffusion of nanoparticles through an endothelial layer as described by Kim et al.<sup>168</sup> This is to be expected, given that these particles were under additional direct pressure to pass through the barrier, as would be physiologically accurate for particles passing through the endothelial barrier of an aortic valve under blood flow.

However, PEGylated SPIONs without the addition of peptide were unable to pass through (**Figure 4.8**). It is unknown whether the PEGylated particles without peptides did not pass through because of interactions with the endothelial layer itself, or because of interactions with the transwell membrane. It may be due,

again, to the somewhat hydrophobic nature of the PEGylated SPIONs, and the potential for their interaction with the transwell membrane itself – in much the same way that the PEGylated particles alone showed high levels of interaction with cholesterol. The material of the transwell membranes, polyethylene, is also somewhat hydrophobic. Although the surface of the transwell membranes is treated for tissue culture, the pores themselves may not be fully treated, and PEGylated particles traveling through the pores may get stuck. If this is the case, repeating similar experiments with whole excised human valve samples may show that PEGylated particles are able to pass through the endothelial layer; future work will be necessary to determine whether this is true.

For studies involving binding of particles to HA subsequent to passage through the endothelial layer, HA was fabricated by drying a borderline saturated calcium phosphate solution. This method was chosen, rather than using powdered HA that can be purchased, because it may more accurately recapitulate the mixture between crystalline HA and amorphous, insoluble calcium phosphate that is present in bone mineral *in vivo*. HABP-SPIONs exhibited significant binding ( $p < 0.05$ ) to ~10mg of HA produced by this method after passing through the endothelial barrier, while OPN-SPIONs did not exhibit significant binding ( $p > 0.05$ ) (**Figure 4.8**). This is somewhat in keeping with the results observed in Chapter 2, Figure 2.9, where HABP-SPIONs, on average, bind in higher quantities to HA than OPN-SPIONs after exposure to serum. It is possible that OPN-SPIONs also exhibit binding, but more replicate experiments would need to be performed to reach

significant differences. However, based on these results, it appears that HABP-SPIONs may be more promising for applications in CAVD detection, as they are undoubtedly able to pass through the endothelial layer and bind to HA after passage.

Studies comparing HA-targeted and non-targeted binding of SPIONs to diseased and non-diseased aortic valve samples yielded exciting results. Overall, through all samples tested, it appeared that HABP-, OPN-, and PEG-SPIONs demonstrated binding to diseased samples in significant enough quantities that staining with Prussian Blue yielded visible results. Generally speaking, HABP-SPIONs demonstrated higher levels of binding than either OPN-SPIONs or PEG-SPIONs, as well as better colocalization with calcium deposits as visualized by Von Kossa staining. Additionally, PEG-SPIONs show very substantial, macroscopically-visible binding to non-diseased samples, while OPN-SPIONs showed only a low level of binding to these samples, and HABP-SPIONs showed very little, if any, visible off-target binding. Preliminary assessment of samples that did not show macroscopic disease indicated that HABP-SPIONs may additionally bind to microcalcifications, although further studies will need to be performed on additional, intact human aortic valve samples to ascertain this observation. Taken together, these results confirm what other previous studies also suggested: that HABP-SPIONs are suitably selective in binding to diseased human tissue to act as targeted contrast agents in detection of CAVD.

## Chapter 5: Conclusions and Further Studies

In this dissertation, we describe the development, optimization, and testing of a hydroxyapatite-targeted SPION that can be used for the early detection of CAVD.

In Chapter 2, we fabricated and characterized two different HA-targeted SPIONs using two distinct peptides (HABP and OPN). We evaluated the success of fabrication using DLS, zeta potential measurements, and the BCA assay to confirm peptide attachment. We characterized the *in vitro* binding properties of the SPIONs in the presence of both sodium phosphate buffer and 50% FBS. We then performed several studies to better understand the protein corona of HABP-, OPN-, and PEG-SPIONs, including studies to quantify the amount of protein in the hard vs. soft corona after various incubation times with serum. Ultimately, results demonstrated that, although all produced SPIONs immediately associated with serum proteins, the vast majority of protein interactions were both weak and non-specific. It is hypothesized that this, in addition to the charge-based nature of the peptide interaction with HA, allows for specific binding to occur to HA even in the presence of 50% FBS.

Studies to identify which specific proteins are present in the soft and hard corona of the various SPIONs were not performed as a part of this dissertation, but this could be an interesting direction to explore in the future. Techniques such as mass spectrometry and X-ray powder diffraction could readily be used to assess the makeup of the hard and soft protein coronas, which may give some insight into the

predicted behavior of various SPIONs *in vivo*. Similar experiments with SPIONs as well as other types of nanoparticles have been described in the literature,<sup>85,88,121</sup> it may be useful in the future to compare the types of proteins shown to interact with those particles with the types of proteins that interact with HABP-, OPN-, or PEG-SPIONs.

In addition, observing different components of the protein corona in different matrices or under different conditions could provide some useful insights about the nature of the protein corona in general, and the nature of the SPION protein corona in particular. Previous studies, such as those by Lundqvist et al. have examined the different protein coronas that result from exposing nanoparticles to different matrices, such as FBS, human serum, and whole blood.<sup>188</sup> These studies found that the protein corona of a given nanoparticle showed notable variation when the nanoparticles were placed in different matrices, particularly in human whole blood. Similar studies with HABP-, OPN-, and PEG-SPIONS could examine whether some of the proteins that are bound to SPIONs in whole blood are part of either the coagulation cascade or the complement system. The presence of these proteins in the corona might indicate that SPIONs may precipitate an immune reaction. Such results from these studies could provide important pre-clinical information in the further development of SPIONs as a clinical MR contrast agent.

Another aspect of the SPION protein corona that could be examined is impact of flow conditions on the formation and make-up of the protein corona of these

SPIONs. Previous studies such as those from Palchetti et al. have indicated that the proteins that comprise the protein corona may be different under flow conditions.<sup>123</sup> Since SPIONs will be under flow *in vivo*, these experiments could provide valuable insight into particle behavior, interactions, and the potential for an immune system response *in vivo*.

In addition to studies to further examine the protein corona around HABP-, OPN-, and PEG-SPIONs, it may be useful or interesting to examine other peptides and potentially other disease targets. Hydroxyapatite was chosen as a favorable target based on several criteria discussed earlier; however, other potential disease targets were considered, such as markers of endothelial disruption, lipoprotein deposition, and mast cells or macrophages. Additionally, fabricating nanoparticles that can bind to e.g. endothelial disruption or macrophages may have implications for a range of diseases beyond CAVD, such as atherosclerosis and various forms of cancer.<sup>189–191</sup> Ultimately, although targeting HA has several advantages, it may be worthwhile to evaluate SPIONs conjugated to peptides that specifically bind to these targets using a similar range of experiments to those described in Chapter 2.

In Chapter 3, we explored optimization parameters of SPIONs in terms of both binding to HA as well as MR signal. We determined that altering the number or ratio of peptides per SPION did not have a substantial impact on SPION binding to HA within a range of reasonable peptide quantities. Although this may have

implications for cost efficiency of nanoparticle production in the future, this type of modification appears to be of less importance to particle functionality.

PEGylation method, PEG chain length, and SPION core size all showed impacts on SPION MR relaxivities in solution. While the impact of PEG chain length depended on the PEGylation method, the effect of SPION core size was more consistent, showing that SPIONs with a larger core size generally have higher  $r_2$  relaxivities. This is in keeping with what has been shown by LaConte et al.<sup>192</sup> The effect of PEGylation method was perhaps the most influential factor, with NH<sub>2</sub>-PEGylation showing, overall, higher relaxivities than either PO-PEGylation or DSPE-PEGylation. It is hypothesized that this is due to the hydrophilicity of the CA-SPION core produced for NH<sub>2</sub>-PEGylation, as compared to the more hydrophobic core produced using the other two PEGylation methods. Ultimately, these studies helped to determine that the optimal particle would have a 10nm core, functionalized with either 3.4kDa or 5kDa PEG chains using the NH<sub>2</sub>-PEGylation method for optimal MR signal.

Because relatively little work has been done on MR signal optimization across physiochemically distinct SPIONs, there are many future directions that could be explored in these studies. For example, it would be interesting to observe how different media may impact the MR signals or trends therein. The motility of water around the particles may alter in serum or whole blood as compared to the sodium phosphate buffer used in these studies, which would in turn impact the MR signal.

These trends have largely not been explored in the literature, and could yield interesting results that may provide insight about particle behavior and movement in different media. Although it would be challenging if not impossible to perform similar studies looking at MR signal of particles bound to HA in different media due to the gel-like material needed to successfully suspend HA for the duration of the scan, non-binding studies may still hold useful insights, particularly about potential particle behavior in a more clinically relevant environment.

Additionally, although a relatively narrow range of PEG chain lengths were selected for the studies described in Chapter 3, future studies could examine a wider range of PEG chain lengths, such as those < 1000 kDa or > 10,000 kDa. A report by LaConte et al. indicated that the response of R2 to differences in PEG chain length for lengths <1000 kDa differed substantially from the impact for those >1000 kDa.<sup>192</sup> This is a population that was not explored in these studies, and wider variation in PEG chain length could be well worth assessing in the future. Other nanoparticle design parameters could be varied as well, such as the use of different PEG chain lengths on a single particle.

Finally, although two SPION core sizes were assessed, it was observed that neither produced significant positive (T1) contrast. However, some studies have shown that certain SPIONs can be used as T1 contrast agents, and this is an active area of research in the field.<sup>149,193,194</sup> T1 contrast agents are often preferred clinically to T2 contrast agents because the brightness of the contrast agent is

more easily detected and has better resolution.<sup>195</sup> However, much like other SPIONs, studies have not been performed to optimize the T1 signal of such ultras-small SPIONs. If smaller SPIONs such as those described by Wei et al. could be produced, it would be worthwhile to perform further studies to assess the behavior and MR signal of these SPIONs while varying PEG chain length and PEGylation method as well.

In Chapter 4, we assessed the medically-relevant properties of targeted SPIONs. First, we measured the MR signal of the fully functionalized SPIONs, before examining the MR signal of bound vs. unbound targeted SPIONs to ensure that binding was occurring. Results from these studies indicated that fully-functionalized SPIONs show relaxivities within the expected ranges, and that there is a measurable difference in signal as expected between bound and unbound SPIONs. Cytotoxicity studies confirmed that functionalized SPIONs do not demonstrate cytotoxic effects upon incubation with HUVECs, and so SPIONs are expected to be safe for medical use. The potential for some systemic effects was evaluated by examining the impact of both peptides and peptide-functionalized SPIONs on the nucleation and formation of HA crystals. Although peptides and SPIONs in buffer were both observed to have effects on HA nucleation and formation, in the presence of serum, neither peptides nor peptide-functionalized SPIONs exhibited behaviors different from a control sample. Thus, there should not be concern about the systemic impact of HA-targeted SPIONs on bone homeostasis. Studies performed using a unique, customized transwell setup

confirmed the ability of targeted SPIONs to pass through a model endothelial barrier, and HABP-SPIONs demonstrated significant binding to HA subsequently. Finally, the binding of SPIONs to excised human valve samples was evaluated. Although HABP-, OPN-, and PEG-SPIONs all showed visible binding to diseased samples, PEG-SPIONs also showed substantial binding to non-diseased samples, while OPN-SPIONs were more selective, and HABP-SPIONs showed little to no off-target binding to non-diseased samples. Taken together, these results indicate that HABP-SPIONs show great promise as potential contrast agents for the detection of calcification in human aortic valves.

There are a multitude of studies that could be performed in the further development of HABP-SPIONs as potential contrast agents in the early detection of CAVD. One potentially useful set of studies would be broader evaluation of nanoparticle cytotoxicity. Although SPIONs are not expected to be immediately cytotoxic, the long-term effects of incubation with SPIONs have not been as thoroughly assessed. A review of several studies by Singh, et. al has indicated that some SPIONs at some doses can cause cytotoxicity via a variety of pathways, including impaired mitochondrial function, generation of reactive oxygen species, and DNA damage.<sup>165</sup> These effects largely appear to be dependent on the dosage, surface modifications, and exposure time of the administered SPIONs, in addition to the cell type used in evaluation.<sup>196</sup> A more comprehensive examination of HA-targeted SPION toxicity would include assessments of mitochondrial function as well as

measurements of genotoxicity using the comet assay. It may also be beneficial to test a larger variety of incubation times with HA-SPIONs.

A crucial set of studies to perform in the future will be the assessment of HABP-SPION binding to whole, rather than sectioned, aortic valve samples. Studies in this dissertation were limited by the availability of human samples. While the studies in this dissertation suggest that SPIONs will be able to pass through the endothelial membrane coating early calcium deposits and bind to the HA underneath, this will need to be confirmed in follow-up studies. These studies could also be performed on valves from patients at varying disease stages, thus allowing us to examine whether SPION binding occurs proportionally to calcium deposition in the valves. It would also be beneficial for these studies to image the excised valves using an MR scanner. Such results would help to confirm that HA-targeted SPIONs can bind to HA in whole valve samples in sufficient quantities to generate a measurable MR signal. These studies could additionally serve to evaluate various approaches for delivery of HA-SPIONs as a contrast agent by embedding the excised aortic valve samples in a physiologic flow loop of the aorta filled with a circulating physiologic nutrient solution.

Further preclinical studies would need to examine nanoparticle safety and efficacy in an animal model. Although, as previously discussed, there is not an optimal animal model for CAVD, animal studies could provide critical information in terms of safety, dosing, and timing of the MR scan subsequent to nanoparticle

administration. Because HA deposition is a disease feature in atherosclerosis as well as aortic stenosis, it may be possible to use an animal model of atherosclerotic disease for these studies.

Finally, it is possible that the nanoparticles described in this dissertation could have uses for other applications or diseases. Hydroxyapatite formation and calcification is a feature of a wide variety of diseases, both cardiovascular and otherwise (e.g. chronic kidney disease). With respect to cardiovascular diseases, hydroxyapatite plays a role in diseases such as atherosclerosis, where calcium deposits in coronary arteries can indicate the presence of a plaque.<sup>60,197,198</sup> Hydroxyapatite is also found in calciphylaxis, which is characterized by arteriolar calcification of the media.<sup>199–201</sup> In non-cardiovascular diseases, hydroxyapatite may be found in vascular calcifications present in chronic kidney disease as well.<sup>202,203</sup> The ability to detect hydroxyapatite via MRI could potentially have benefits for these diseases as well, thus contributing to the wider potential utility of HABP-SPIONS.

## Bibliography

- (1) Team, H. L. Aortic Valve Disease: Symptoms, Causes & Treatment <https://www.healthlibrary.in/aortic-valve-disease/> (accessed Jul 24, 2018).
- (2) Aortic Valve Stenosis: Care Instructions <https://myhealth.alberta.ca:443/Health/aftercareinformation/pages/conditions.aspx?hwid=ut2752> (accessed Jul 24, 2018).
- (3) Beckmann, E.; Grau, J. B.; Sainger, R.; Poggio, P.; Ferrari, G. Insights into the Use of Biomarkers in Calcific Aortic Valve Disease. *Journal of Heart Valve Disease*. **2010**, 19 (4), 441–452.
- (4) Nishimura, R. A.; Otto, C. M.; Bonow, R. O.; Carabello, B. A.; Erwin, J. P.; Guyton, R. A.; O’Gara, P. T.; Ruiz, C. E.; Skubas, N. J.; Sorajja, P.; et al. 2014 AHA/ACC Guideline for the Management of Patients With Valvular Heart Disease. *Journal of the American College of Cardiology*. **2014**, 63 (22), e57–e185. <https://doi.org/10.1016/j.jacc.2014.02.536>.
- (5) Aikawa, E.; Schoen, F. J. Chapter 9 - Calcific and Degenerative Heart Valve Disease A2 - Stone, Monte S. WillisJonathon W. HomeisterJames R. In *Cellular and Molecular Pathobiology of Cardiovascular Disease*; Academic Press: San Diego, 2014; pp 161–180.
- (6) Otto, C. M.; Lind, B. K.; Kitzman, D. W.; Gersh, B. J.; Siscovick, D. S. Association of Aortic-Valve Sclerosis with Cardiovascular Mortality and Morbidity in the Elderly. *New England Journal of Medicine*. **1999**, 341 (3), 142–147. <https://doi.org/10.1056/NEJM199907153410302>.
- (7) Cary, T.; Pearce, J. Aortic Stenosis: Pathophysiology, Diagnosis, and Medical Management of Nonsurgical Patients. *Critical Care Nurse* **2013**, 33 (2), 58–72. <https://doi.org/10.4037/ccn2013820>.
- (8) Cardiac MRI <https://www.med-ed.virginia.edu/courses/rad/cardiacmr/Indications/Advantages.html> (accessed Mar 17, 2016).
- (9) Prakash, A.; Powell, A. J.; Geva, T. Multimodality Noninvasive Imaging for Assessment of Congenital Heart Disease. *Circulation. Cardiovascular Imaging* **2010**, 3 (1), 112–125. <https://doi.org/10.1161/CIRCIMAGING.109.875021>.

- (10) Hjortnaes, J.; New, S. E. P.; Aikawa, E. Visualizing Novel Concepts of Cardiovascular Calcification. *Trends in Cardiovascular Medicine*. **2013**, *23* (3), 71–79. <https://doi.org/10.1016/j.tcm.2012.09.003>.
- (11) Agabegi, S. S.; Agabegi, E. *Step-Up to Medicine*. Fourth ed. Wolters Kluwer Health: Philadelphia, 2016.
- (12) Bates, E. R. Treatment Options in Severe Aortic Stenosis. *Circulation* **2011**, *124* (3), 355–359. <https://doi.org/10.1161/CIRCULATIONAHA.110.974204>.
- (13) Rosenhek, R.; Klaar, U.; Schemper, M.; Scholten, C.; Heger, M.; Gabriel, H.; Binder, T.; Maurer, G.; Baumgartner, H. Mild and Moderate Aortic Stenosis. *European Heart Journal*. **2004**, *25* (3), 199–205. <https://doi.org/10.1016/j.ehj.2003.12.002>.
- (14) Predictors of Outcome in Severe, Asymptomatic Aortic Stenosis [https://www.researchgate.net/publication/12357071\\_Predictors\\_of\\_Outcome\\_in\\_Severe\\_Asymptomatic\\_Aortic\\_Stenosis](https://www.researchgate.net/publication/12357071_Predictors_of_Outcome_in_Severe_Asymptomatic_Aortic_Stenosis) (accessed Jul 24, 2018).
- (15) Aortic Valve Disease <http://www.clevelandclinicmeded.com/medicalpubs/diseasemanagement/cardiology/aortic-valve-disease/> (accessed May 9, 2018).
- (16) Chan, K. L.; Teo, K.; Dumesnil, J. G.; Ni, A.; Tam, J. Effect of Lipid Lowering With Rosuvastatin on Progression of Aortic Stenosis: Results of the Aortic Stenosis Progression Observation: Measuring Effects of Rosuvastatin (ASTRONOMER) Trial. *Circulation* **2010**, *121* (2), 306–314. <https://doi.org/10.1161/CIRCULATIONAHA.109.900027>.
- (17) Carabello, B. A. Evaluation and Management of Patients With Aortic Stenosis. *Circulation* **2002**, *105* (15), 1746–1750. <https://doi.org/10.1161/01.CIR.0000015343.76143.13>.
- (18) Leon, M. B.; Smith, C. R.; Mack, M.; Miller, D. C.; Moses, J. W.; Svensson, L. G.; Tuzcu, E. M.; Webb, J. G.; Fontana, G. P.; Makkar, R. R.; et al. Transcatheter Aortic-Valve Implantation for Aortic Stenosis in Patients Who Cannot Undergo Surgery. *New England Journal of Medicine*. **2010**, *363* (17), 1597–1607. <https://doi.org/10.1056/NEJMoa1008232>.
- (19) Miller, D. C.; Blackstone, E. H.; Mack, M. J.; Svensson, L. G.; Kodali, S. K.; Kapadia, S.; Rajeswaran, J.; Anderson, W. N.; Moses, J. W.; Tuzcu, E. M.; et al. Transcatheter (TAVR) versus Surgical (AVR) Aortic Valve Replacement: Occurrence, Hazard, Risk Factors, and Consequences of

Neurologic Events in the PARTNER Trial. *Journal of Thoracic and Cardiovascular Surgery*. **2012**, 143 (4), 832–843.e13.  
<https://doi.org/10.1016/j.jtcvs.2012.01.055>.

- (20) Clinical Trials - Mayo Clinic Research  
[https://www.mayo.edu/research/clinical-trials/search-results?status=open-unknown&poclid=PRC-20166513&\\_ga=2.90972755.896530134.1537379167-931636586.1537379167](https://www.mayo.edu/research/clinical-trials/search-results?status=open-unknown&poclid=PRC-20166513&_ga=2.90972755.896530134.1537379167-931636586.1537379167) (accessed Sep 19, 2018).
- (21) Brown, C. H.; Hasan, R. K.; Brady, M. B. Is Less Really More?: Conscious Sedation or General Anesthesia for Transcatheter Aortic Valve Replacement. *Circulation* **2017**, 136 (22), 2141–2143.  
<https://doi.org/10.1161/CIRCULATIONAHA.117.031281>.
- (22) *Vital Statistics of the United States: Births, Life Expectancy, Deaths, and Selected Health Data*; Fifth ed. Bernan Press, 2012.
- (23) Reardon, M. J. Cost-Effectiveness Analysis of TAVR. *Methodist DeBakey Cardiovascular Journal*. **2012**, 8 (2), 26–28.
- (24) Foroutan, F.; Guyatt, G. H.; O'Brien, K.; Bain, E.; Stein, M.; Bhagra, S.; Sit, D.; Kamran, R.; Chang, Y.; Devji, T.; et al. Prognosis after Surgical Replacement with a Bioprosthetic Aortic Valve in Patients with Severe Symptomatic Aortic Stenosis: Systematic Review of Observational Studies. *BMJ: British Medical Journal* **2016**, 354, i5065.  
<https://doi.org/10.1136/bmj.i5065>.
- (25) Trepels, T.; Martens, S.; Doss, M.; Fichtlscherer, S.; Schächinger, V. Thrombotic Restenosis After Minimally Invasive Implantation of Aortic Valve Stent. *Circulation* **2009**, 120 (4), e23–e24.  
<https://doi.org/10.1161/CIRCULATIONAHA.109.864892>.
- (26) Clark, M. A.; Duhay, F. G.; Thompson, A. K.; Keyes, M. J.; Svensson, L. G.; Bonow, R. O.; Stockwell, B. T.; Cohen, D. J. Clinical and Economic Outcomes after Surgical Aortic Valve Replacement in Medicare Patients. *Risk Management and Healthcare Policy* **2012**, 5, 117–126.  
<https://doi.org/10.2147/RMHP.S34587>.
- (27) Aikawa, E.; Schoen, F. J. Chapter 9 - Calcific and Degenerative Heart Valve Disease A2 - Stone, Monte S. WillisJonathon W. HomeisterJames R. In *Cellular and Molecular Pathobiology of Cardiovascular Disease*; Academic Press: San Diego, 2014; pp 161–180.

- (28) Lilly, L. S. *Pathophysiology of Heart Disease: A Collaborative Project of Medical Students and Faculty*, Fifth Edition; Lippincott, Williams & Wilkins: Baltimore, MD, 2010.
- (29) Ranganathan, N.; Sivaciyan, V.; Saksena, F. B. *The Art and Science of Cardiac Physical Examination: With Heart Sounds and Pulse Wave Forms on CD*; Springer Science & Business Media, 2007.
- (30) Bermejo, J. The Effects of Hypertension on Aortic Valve Stenosis. *Heart* **2005**, *91* (3), 280–282. <https://doi.org/10.1136/hrt.2004.041749>.
- (31) Kaden, J. J.; Haghi, D. Hypertension in Aortic Valve Stenosis—a Trojan Horse. *European Heart Journal*. **2008**, *29* (16), 1934–1935. <https://doi.org/10.1093/eurheartj/ehn306>.
- (32) Stewart, B. F.; Siscovick, D.; Lind, B. K.; Gardin, J. M.; Gottdiener, J. S.; Smith, V. E.; Kitzman, D. W.; Otto, C. M. Clinical Factors Associated With Calcific Aortic Valve Disease. This Study Was Supported in Part by Contracts NO1-HC85079 through HC-850086 from the National Heart, Lung, and Blood Institute, National Institutes of Health, Bethesda, Maryland. *Journal of the American College of Cardiology*. **1997**, *29* (3), 630–634. [https://doi.org/10.1016/S0735-1097\(96\)00563-3](https://doi.org/10.1016/S0735-1097(96)00563-3).
- (33) Thubrikar, M. J.; Aouad, J.; Nolan, S. P. Patterns of Calcific Deposits in Operatively Excised Stenotic or Purely Regurgitant Aortic Valves and Their Relation to Mechanical Stress. *American Journal of Cardiology*. **1986**, *58* (3), 304–308. [https://doi.org/10.1016/0002-9149\(86\)90067-6](https://doi.org/10.1016/0002-9149(86)90067-6).
- (34) Bertazzo, S.; Gentleman, E.; Cloyd, K. L.; Chester, A. H.; Yacoub, M. H.; Stevens, M. M. Nano-Analytical Electron Microscopy Reveals Fundamental Insights into Human Cardiovascular Tissue Calcification. *Nature Materials*. **2013**, *12* (6), 576–583. <https://doi.org/10.1038/nmat3627>.
- (35) Aikawa, E.; Nahrendorf, M.; Sosnovik, D.; Lok, V. M.; Jaffer, F. A.; Aikawa, M.; Weissleder, R. Multimodality Molecular Imaging Identifies Proteolytic and Osteogenic Activities in Early Aortic Valve Disease. *Circulation* **2007**, *115* (3), 377–386. <https://doi.org/10.1161/CIRCULATIONAHA.106.654913>.
- (36) O'Brien, K. D.; Reichenbach, D. D.; Marcovina, S. M.; Kuusisto, J.; Alpers, C. E.; Otto, C. M. Apolipoproteins B, (a), and E Accumulate in the Morphologically Early Lesion of 'Degenerative' Valvular Aortic Stenosis. *Arteriosclerosis, Thrombosis, and Vascular Biology*. **1996**, *16* (4), 523–532. <https://doi.org/10.1161/01.ATV.16.4.523>.

- (37) Rodriguez, K. J.; Piechura, L. M.; Porras, A. M.; Masters, K. S. Manipulation of Valve Composition to Elucidate the Role of Collagen in Aortic Valve Calcification. *BMC Cardiovascular Disorders*. **2014**, *14*, 29. <https://doi.org/10.1186/1471-2261-14-29>.
- (38) Jin, R.; Lin, B.; Li, D.; Ai, H. Superparamagnetic Iron Oxide Nanoparticles for MR Imaging and Therapy: Design Considerations and Clinical Applications. *Current Opinion in Pharmacology*. **2014**, *18*, 18–27. <https://doi.org/10.1016/j.coph.2014.08.002>.
- (39) Uppal, R.; Caravan, P. Targeted Probes for Cardiovascular MR Imaging. *Future Medicinal Chemistry*. **2010**, *2* (3), 451–470. <https://doi.org/10.4155/FMC.09.154>.
- (40) T1 and T2 effects <http://mriquestions.com/opposite-effects-uarrt1-uarrt2.html> (accessed May 9, 2018).
- (41) MRI Contrast Agent. *Wikipedia*; 2018.
- (42) Diagnostic Evaluation of Hepatocellular Carcinoma in a Cirrhotic Liver: Page 2 of 2 | Cancer Network <http://www.cancernetwork.com/gastrointestinal-cancer/diagnostic-evaluation-hepatocellular-carcinoma-cirrhotic-liver/page/0/1> (accessed May 9, 2018).
- (43) Caravan, P. Strategies for Increasing the Sensitivity of Gadolinium Based MRI Contrast Agents. *Chemical Society Reviews*. **2006**, *35* (6), 512. <https://doi.org/10.1039/b510982p>.
- (44) Thomsen, H. S. Gadolinium-Based Contrast Media May Be Nephrotoxic Even at Approved Doses. *European Radiology*. **2004**, *14* (9), 1654–1656. <https://doi.org/10.1007/s00330-004-2379-0>.
- (45) Chen, R.; Ling, D.; Zhao, L.; Wang, S.; Liu, Y.; Bai, R.; Baik, S.; Zhao, Y.; Chen, C.; Hyeon, T. Parallel Comparative Studies on Mouse Toxicity of Oxide Nanoparticle- and Gadolinium-Based T1 MRI Contrast Agents. *ACS Nano* **2015**, *9* (12), 12425–12435. <https://doi.org/10.1021/acsnano.5b05783>.
- (46) Wahba, I. M.; Simpson, E. L.; White, K. Gadolinium Is Not the Only Trigger for Nephrogenic Systemic Fibrosis: Insights from Two Cases and Review of the Recent Literature. *American Journal of Transplantation*. **2007**, *7* (10), 2425–2432. <https://doi.org/10.1111/j.1600-6143.2007.01941.x>.

- (47) Takahashi, M.; Tsutsui, H.; Murayama, C.; Miyazawa, T.; Fritz-Zieroth, B. Neurotoxicity of Gadolinium Contrast Agents for Magnetic Resonance Imaging in Rats with Osmotically Disrupted Blood-Brain Barrier. *Magnetic Resonance Imaging* **1996**, *14* (6), 619–623. [https://doi.org/10.1016/0730-725X\(96\)00118-X](https://doi.org/10.1016/0730-725X(96)00118-X).
- (48) Li, L.; Jiang, W.; Luo, K.; Song, H.; Lan, F.; Wu, Y.; Gu, Z. Superparamagnetic Iron Oxide Nanoparticles as MRI Contrast Agents for Non-Invasive Stem Cell Labeling and Tracking. *Theranostics* **2013**, *3* (8), 595–615. <https://doi.org/10.7150/thno.5366>.
- (49) GastroMARK New FDA Drug Approval | CenterWatch  
<http://www.centerwatch.com/drug-information/fda-approved-drugs/drug/105/gastromark> (accessed Mar 17, 2016).
- (50) Estelrich, J.; Sánchez-Martín, M. J.; Busquets, M. A. Nanoparticles in Magnetic Resonance Imaging: From Simple to Dual Contrast Agents. *International Journal of Nanomedicine* **2015**, *10*, 1727–1741. <https://doi.org/10.2147/IJN.S76501>.
- (51) Feraheme® (ferumoxytol) | Product Information | Home  
<https://www.feraheme.com/> (accessed Dec 11, 2018).
- (52) Sharifi, S.; Seyednejad, H.; Laurent, S.; Atyabi, F.; Saei, A. A.; Mahmoudi, M. Superparamagnetic Iron Oxide Nanoparticles for in Vivo Molecular and Cellular Imaging. *Contrast Media & Molecular Imaging* **2015**, *10* (5), 329–355. <https://doi.org/10.1002/cmml.1638>.
- (53) Mu, K.; Zhang, S.; Ai, T.; Jiang, J.; Yao, Y.; Jiang, L.; Zhou, Q.; Xiang, H.; Zhu, Y.; Yang, X.; et al. Monoclonal Antibody-Conjugated Superparamagnetic Iron Oxide Nanoparticles for Imaging of Epidermal Growth Factor Receptor-Targeted Cells and Gliomas. *Molecular Imaging* **2015**, *14*. [doi.org/10.2310/7290.2015.00002](https://doi.org/10.2310/7290.2015.00002)
- (54) Sardan, M.; Eren, E. D.; Ozdemir, A.; Tekinay, A. B.; Guler, M. O. Bioactive Peptide Functionalized Superparamagnetic Iron Oxide Nanoparticles (SPIONs) for Targeted Imaging with MRI. In *2015 5th International Workshop on Magnetic Particle Imaging (IWMPI)*; 2015; pp 1–1. <https://doi.org/10.1109/IWMPI.2015.7107067>.
- (55) Kohler, N.; Sun, C.; Wang, J.; Zhang, M. Methotrexate-Modified Superparamagnetic Nanoparticles and Their Intracellular Uptake into Human Cancer Cells. *Langmuir* **2005**, *21* (19), 8858–8864. <https://doi.org/10.1021/la0503451>.

- (56) Nadir, M. A.; Wei, L.; Elder, D. H. J.; Libianto, R.; Lim, T. K.; Pauriah, M.; Pringle, S. D.; Doney, A. D.; Choy, A.-M.; Struthers, A. D.; et al. Impact of Renin-Angiotensin System Blockade Therapy on Outcome in Aortic Stenosis. *Journal of the American College of Cardiology*. **2011**, *58* (6), 570–576. <https://doi.org/10.1016/j.jacc.2011.01.063>.
- (57) Rajamannan, N. M.; Evans, F. J.; Aikawa, E.; Grande-Allen, K. J.; Demer, L. L.; Heistad, D. D.; Simmons, C. A.; Masters, K. S.; Mathieu, P.; O'Brien, K. D.; et al. Calcific Aortic Valve Disease: Not Simply a Degenerative Process: A Review and Agenda for Research from the National Heart and Lung and Blood Institute Aortic Stenosis Working Group Executive Summary: Calcific Aortic Valve Disease – 2011 Update. *Circulation* **2011**, *124* (16), 1783–1791. <https://doi.org/10.1161/CIRCULATIONAHA.110.006767>.
- (58) Towler, D. A. Molecular and Cellular Aspects of Calcific Aortic Valve Disease. *Circulation Research*. **2013**, *113* (2), 198–208. <https://doi.org/10.1161/CIRCRESAHA.113.300155>.
- (59) Chin, D. D.; Chowdhuri, S.; Chung, E. J. Calcium-Binding Nanoparticles for Vascular Disease. *Regenerative Engineering and Translational Medicine*. **2018**. <https://doi.org/10.1007/s40883-018-0083-x>.
- (60) Lee, J. S.; Morrisett, J. D.; Tung, C.-H. Detection of Hydroxyapatite in Calcified Cardiovascular Tissues. *Atherosclerosis* **2012**, *224* (2), 340–347. <https://doi.org/10.1016/j.atherosclerosis.2012.07.023>.
- (61) Koos, R.; Mahnken, A. H.; Sinha, A. M.; Wildberger, J. E.; Hoffmann, R.; Kühl, H. P. Aortic Valve Calcification as a Marker for Aortic Stenosis Severity: Assessment on 16-MDCT. *American Journal of Roentgenology*. **2004**, *183* (6), 1813–1818. <https://doi.org/10.2214/ajr.183.6.01831813>.
- (62) Meisel, C. L.; Bainbridge, P.; Mitsouras, D.; Wong, J. Y. Targeted Nanoparticle Binding to Hydroxyapatite in a High Serum Environment for Early Detection of Heart Disease. *ACS Applied Nano Materials*. **2018**. <https://doi.org/10.1021/acsnm.8b01099>.
- (63) Gao, X.; Cui, Y.; Levenson, R. M.; Chung, L. W. K.; Nie, S. *In Vivo* Cancer Targeting and Imaging with Semiconductor Quantum Dots. *Nature Biotechnology*. **2004**, *22* (8), 969. <https://doi.org/10.1038/nbt994>.
- (64) Choi, C. H. J.; Alabi, C. A.; Webster, P.; Davis, M. E. Mechanism of Active Targeting in Solid Tumors with Transferrin-Containing Gold Nanoparticles. *Proceedings of the National Academy of Sciences of the United States of*

- America*. **2010**, *107* (3), 1235–1240.  
<https://doi.org/10.1073/pnas.0914140107>.
- (65) Farokhzad, O. C.; Cheng, J.; Teply, B. A.; Sherifi, I.; Jon, S.; Kantoff, P. W.; Richie, J. P.; Langer, R. Targeted Nanoparticle-Aptamer Bioconjugates for Cancer Chemotherapy in Vivo. *Proceedings of the National Academy of Sciences of the United States of America*. **2006**, *103* (16), 6315–6320. <https://doi.org/10.1073/pnas.0601755103>.
- (66) Peer, D.; Karp, J. M.; Hong, S.; Farokhzad, O. C.; Margalit, R.; Langer, R. Nanocarriers as an Emerging Platform for Cancer Therapy. *Nature Nanotechnology*. **2007**, *2* (12), 751.  
<https://doi.org/10.1038/nnano.2007.387>.
- (67) Davis, M. E.; Chen, Z. (Georgia); Shin, D. M. Nanoparticle Therapeutics: An Emerging Treatment Modality for Cancer. *Nature Reviews. Drug Discovery*. **2008**, *7* (9), 771. <https://doi.org/10.1038/nrd2614>.
- (68) Malam, Y.; Loizidou, M.; Seifalian, A. M. Liposomes and Nanoparticles: Nanosized Vehicles for Drug Delivery in Cancer. *Trends in Pharmacological Sciences*. **2009**, *30* (11), 592–599.  
<https://doi.org/10.1016/j.tips.2009.08.004>.
- (69) Dextran-Coated Iron Oxide Nanoparticles: A Versatile Platform for Targeted Molecular Imaging, Molecular Diagnostics, and Therapy  
<http://pubs.acs.org/doi/pdf/10.1021/ar200084x> (accessed Jan 11, 2018).
- (70) Georganopoulou, D. G.; Chang, L.; Nam, J.-M.; Thaxton, C. S.; Mufson, E. J.; Klein, W. L.; Mirkin, C. A. Nanoparticle-Based Detection in Cerebral Spinal Fluid of a Soluble Pathogenic Biomarker for Alzheimer's Disease. *Proceedings of the National Academy of Sciences of the United States of America*. **2005**, *102* (7), 2273–2276.  
<https://doi.org/10.1073/pnas.0409336102>.
- (71) Roy, M. D.; Stanley, S. K.; Amis, E. J.; Becker, M. L. Identification of a Highly Specific Hydroxyapatite-Binding Peptide Using Phage Display. *Advanced Materials*. **2008**, *20* (10), 1830–1836.  
<https://doi.org/10.1002/adma.200702322>.
- (72) Wang, L.; Guan, X.; Tang, R.; Hoyer, J. R.; Wierzbicki, A.; De Yoreo, J. J.; Nancollas, G. H. Phosphorylation of Osteopontin Is Required for Inhibition of Calcium Oxalate Crystallization. *Journal of Physical Chemistry. B* **2008**, *112* (30), 9151–9157. <https://doi.org/10.1021/jp804282u>.

- (73) Hunter, G. K. Role of Osteopontin in Modulation of Hydroxyapatite Formation. *Calcified Tissue International*. **2013**, *93* (4), 348–354. <https://doi.org/10.1007/s00223-013-9698-6>.
- (74) Mahon, E.; Salvati, A.; Baldelli Bombelli, F.; Lynch, I.; Dawson, K. A. Designing the Nanoparticle–Biomolecule Interface for “Targeting and Therapeutic Delivery.” *Journal of Controlled Release* **2012**, *161* (2), 164–174. <https://doi.org/10.1016/j.jconrel.2012.04.009>.
- (75) Mirshafiee, V.; Kim, R.; Park, S.; Mahmoudi, M.; Kraft, M. L. Impact of Protein Pre-Coating on the Protein Corona Composition and Nanoparticle Cellular Uptake. *Biomaterials* **2016**, *75*, 295–304. <https://doi.org/10.1016/j.biomaterials.2015.10.019>.
- (76) Bertrand, N.; Leroux, J.-C. The Journey of a Drug-Carrier in the Body: An Anatomico-Physiological Perspective. *Journal of Controlled Release*. **2012**, *161* (2), 152–163. <https://doi.org/10.1016/j.jconrel.2011.09.098>.
- (77) Lynch, I.; Dawson, K. A. Protein-Nanoparticle Interactions. *Nano Today* **2008**, *3* (1), 40–47. [https://doi.org/10.1016/S1748-0132\(08\)70014-8](https://doi.org/10.1016/S1748-0132(08)70014-8).
- (78) Mahmoudi, M.; Lynch, I.; Ejtehadi, M. R.; Monopoli, M. P.; Bombelli, F. B.; Laurent, S. Protein–Nanoparticle Interactions: Opportunities and Challenges. *Chemical Reviews*. **2011**, *111* (9), 5610–5637. <https://doi.org/10.1021/cr100440g>.
- (79) Cedervall, T.; Lynch, I.; Lindman, S.; Berggård, T.; Thulin, E.; Nilsson, H.; Dawson, K. A.; Linse, S. Understanding the Nanoparticle-Protein Corona Using Methods to Quantify Exchange Rates and Affinities of Proteins for Nanoparticles. *Proceedings of the National Academy of Sciences of the United States of America*. **2007**, *104* (7), 2050–2055. <https://doi.org/10.1073/pnas.0608582104>.
- (80) Townson, J. L.; Lin, Y.-S.; Agola, J. O.; Carnes, E. C.; Leong, H. S.; Lewis, J. D.; Haynes, C. L.; Brinker, C. J. Re-Examining the Size/Charge Paradigm: Differing in Vivo Characteristics of Size- and Charge-Matched Mesoporous Silica Nanoparticles. *Journal of the American Chemical Society*. **2013**, *135* (43), 16030–16033. <https://doi.org/10.1021/ja4082414>.
- (81) Shah, N. B.; Vercellotti, G. M.; White, J. G.; Fegan, A.; Wagner, C. R.; Bischof, J. C. Blood–Nanoparticle Interactions and in Vivo Biodistribution: Impact of Surface PEG and Ligand Properties. *Molecular Pharmacology*. **2012**, *9* (8), 2146–2155. <https://doi.org/10.1021/mp200626j>.

- (82) Monopoli, M. P.; Walczyk, D.; Campbell, A.; Elia, G.; Lynch, I.; Bombelli, F. B.; Dawson, K. A. Physical-Chemical Aspects of Protein Corona: Relevance to in Vitro and in Vivo Biological Impacts of Nanoparticles. *Journal of the American Chemical Society*. **2011**, *133* (8), 2525–2534. <https://doi.org/10.1021/ja107583h>.
- (83) Lesniak, A.; Salvati, A.; Santos-Martinez, M. J.; Radomski, M. W.; Dawson, K. A.; Åberg, C. Nanoparticle Adhesion to the Cell Membrane and Its Effect on Nanoparticle Uptake Efficiency. *Journal of the American Chemical Society*. **2013**, *135* (4), 1438–1444. <https://doi.org/10.1021/ja309812z>.
- (84) Mirshafiee, V.; Mahmoudi, M.; Lou, K.; Cheng, J.; Kraft, M. L. Protein Corona Significantly Reduces Active Targeting Yield. *Chemical Communications*. **2013**, *49* (25), 2557–2559. <https://doi.org/10.1039/C3CC37307J>.
- (85) Salvati, A.; Pitek, A. S.; Monopoli, M. P.; Prapainop, K.; Bombelli, F. B.; Hristov, D. R.; Kelly, P. M.; Åberg, C.; Mahon, E.; Dawson, K. A. Transferrin-Functionalized Nanoparticles Lose Their Targeting Capabilities When a Biomolecule Corona Adsorbs on the Surface. *Nature Nanotechnology*. **2013**, *8* (2), 137. <https://doi.org/10.1038/nnano.2012.237>.
- (86) Mahmoudi, M.; Bertrand, N.; Zope, H.; Farokhzad, O. C. Emerging Understanding of the Protein Corona at the Nano-Bio Interfaces. *Nano Today* **2016**, *11* (6), 817–832. <https://doi.org/10.1016/j.nantod.2016.10.005>.
- (87) Nguyen, V. H.; Lee, B.-J. Protein Corona: A New Approach for Nanomedicine Design. *International Journal of Nanomedicine* **2017**, *12*, 3137–3151. <https://doi.org/10.2147/IJN.S129300>.
- (88) Casals, E.; Pfaller, T.; Duschl, A.; Oostingh, G. J.; Puntès, V. Time Evolution of the Nanoparticle Protein Corona. *ACS Nano* **2010**, *4* (7), 3623–3632. <https://doi.org/10.1021/nn901372t>.
- (89) Gref, R.; Lück, M.; Quéllec, P.; Marchand, M.; Dellacherie, E.; Harnisch, S.; Blunk, T.; Müller, R. H. ‘Stealth’ Corona-Core Nanoparticles Surface Modified by Polyethylene Glycol (PEG): Influences of the Corona (PEG Chain Length and Surface Density) and of the Core Composition on Phagocytic Uptake and Plasma Protein Adsorption. *Colloids and Surfaces. B, Biointerfaces* **2000**, *18* (3), 301–313. [https://doi.org/10.1016/S0927-7765\(99\)00156-3](https://doi.org/10.1016/S0927-7765(99)00156-3).

- (90) Yu, M.; Huang, S.; Yu, K. J.; Clyne, A. M. Dextran and Polymer Polyethylene Glycol (PEG) Coating Reduce Both 5 and 30 Nm Iron Oxide Nanoparticle Cytotoxicity in 2D and 3D Cell Culture. *International Journal of Molecular Sciences*. **2012**, *13* (5), 5554–5570. <https://doi.org/10.3390/ijms13055554>.
- (91) Wang, R. L. C.; Kreuzer, H. J.; Grunze, M. Molecular Conformation and Solvation of Oligo(Ethylene Glycol)-Terminated Self-Assembled Monolayers and Their Resistance to Protein Adsorption. *Journal of Physical Chemistry. B* **1997**, *101* (47), 9767–9773. <https://doi.org/10.1021/jp9716952>.
- (92) Kim, H. R.; Andrieux, K.; Delomenie, C.; Chacun, H.; Appel, M.; Desmaële, D.; Taran, F.; Georgin, D.; Couvreur, P.; Taverna, M. Analysis of Plasma Protein Adsorption onto PEGylated Nanoparticles by Complementary Methods: 2-DE, CE and Protein Lab-on-Chip® System. *Electrophoresis* **2007**, *28* (13), 2252–2261. <https://doi.org/10.1002/elps.200600694>.
- (93) Pozzi, D.; Colapicchioni, V.; Caracciolo, G.; Piovesana, S.; Capriotti, A. L.; Palchetti, S.; De Grossi, S.; Riccioli, A.; Amenitsch, H.; Laganà, A. Effect of Polyethyleneglycol (PEG) Chain Length on the Bio-Nano-Interactions between PEGylated Lipid Nanoparticles and Biological Fluids: From Nanostructure to Uptake in Cancer Cells. *Nanoscale* **2014**, *6* (5), 2782–2792. <https://doi.org/10.1039/c3nr05559k>.
- (94) Walkey, C. D.; Olsen, J. B.; Guo, H.; Emili, A.; Chan, W. C. W. Nanoparticle Size and Surface Chemistry Determine Serum Protein Adsorption and Macrophage Uptake. *Journal of the American Chemical Society*. **2012**, *134* (4), 2139–2147. <https://doi.org/10.1021/ja2084338>.
- (95) Sun, C.; Sze, R.; Zhang, M. Folic Acid-PEG Conjugated Superparamagnetic Nanoparticles for Targeted Cellular Uptake and Detection by MRI. *Journal of Biomedical Materials Research. Part A* **2006**, *78A* (3), 550–557. <https://doi.org/10.1002/jbm.a.30781>.
- (96) Giljohann, D. A.; Seferos, D. S.; Patel, P. C.; Millstone, J. E.; Rosi, N. L.; Mirkin, C. A. Oligonucleotide Loading Determines Cellular Uptake of DNA-Modified Gold Nanoparticles. *Nano Letters*. **2007**, *7* (12), 3818–3821. <https://doi.org/10.1021/nl072471q>.
- (97) Park, Y.; Whitaker, R. D.; Nap, R. J.; Paulsen, J. L.; Mathiyazhagan, V.; Doerrer, L. H.; Song, Y.-Q.; Hürlimann, M. D.; Szleifer, I.; Wong, J. Y. Stability of Superparamagnetic Iron Oxide Nanoparticles at Different PH

Values: Experimental and Theoretical Analysis. *Langmuir* **2012**, *28* (15), 6246–6255. <https://doi.org/10.1021/la204628c>.

- (98) Park, Y. C.; Smith, J. B.; Pham, T.; Whitaker, R. D.; Sucato, C. A.; Hamilton, J. A.; Bartolak-Suki, E.; Wong, J. Y. Effect of PEG Molecular Weight on Stability, T2 Contrast, Cytotoxicity, and Cellular Uptake of Superparamagnetic Iron Oxide Nanoparticles (SPIONs). *Colloids and Surfaces. B, Biointerfaces* **2014**, *119*, 106–114. <https://doi.org/10.1016/j.colsurfb.2014.04.027>.
- (99) Szydłowski, J.; Van Hook, W. A. Concentration and Temperature Dependence of Dynamic Light Scattering for Some Polystyrene Solutions in Toluene, Cyclohexane, Methylcyclohexane and Deuteromethylcyclohexane. *Macromolecules* **1998**, *31* (10), 3266–3274. <https://doi.org/10.1021/ma971777o>.
- (100) de Bruyn, J. R.; Goiko, M.; Mozaffari, M.; Bator, D.; Dauphinee, R. L.; Liao, Y.; Flemming, R. L.; Bramble, M. S.; Hunter, G. K.; Goldberg, H. A. Dynamic Light Scattering Study of Inhibition of Nucleation and Growth of Hydroxyapatite Crystals by Osteopontin. *PLoS ONE* **2013**, *8* (2). <https://doi.org/10.1371/journal.pone.0056764>.
- (101) Abbas, S.; Kumar, S.; Aswal, V. K.; Kohlbrecher, J. Aggregation in Charged Nanoparticles Solutions Induced by Different Interactions. *AIP Conference Proceedings*. **2016**, *1731* (1), 040011. <https://doi.org/10.1063/1.4947647>.
- (102) Peptide Property Calculator <https://www.genscript.com/tools/peptide-property-calculator> (accessed Jul 26, 2018).
- (103) Kim, K. M.; Trump, B. F. Amorphous Calcium Precipitations in Human Aortic Valve. *Calcified Tissue Research*. **1975**, *18* (1), 155–160. <https://doi.org/10.1007/BF02546237>.
- (104) Towler, D. A. Molecular and Cellular Aspects of Calcific Aortic Valve Disease. *Circulation Research*. **2013**, *113* (2), 198–208. <https://doi.org/10.1161/CIRCRESAHA.113.300155>.
- (105) Weiger, M. C.; Park, J. J.; Roy, M. D.; Stafford, C. M.; Karim, A.; Becker, M. L. Quantification of the Binding Affinity of a Specific Hydroxyapatite Binding Peptide. *Biomaterials* **2010**, *31* (11), 2955–2963. <https://doi.org/10.1016/j.biomaterials.2010.01.012>.
- (106) Naghavi, M.; John, R.; Naguib, S.; Siadaty, M. S.; Grasu, R.; Kurian, K. C.; van Winkle, W. B.; Soller, B.; Litovsky, S.; Madjid, M.; et al. PH

- Heterogeneity of Human and Rabbit Atherosclerotic Plaques; a New Insight into Detection of Vulnerable Plaque. *Atherosclerosis* **2002**, *164* (1), 27–35.
- (107) Brix, G.; Semmler, W.; Port, R.; Schad, L. R.; Layer, G.; Lorenz, W. J. Pharmacokinetic Parameters in CNS Gd-DTPA Enhanced MR Imaging. *Journal of Computer Assisted Tomography*. **1991**, *15* (4), 621–628.
- (108) Essig, M.; Shiroishi, M. S.; Nguyen, T. B.; Saake, M.; Provenzale, J. M.; Enterline, D.; Anzalone, N.; Dörfler, A.; Rovira, À.; Wintermark, M.; et al. Perfusion MRI: The Five Most Frequently Asked Technical Questions. *AJR American Journal of Roentgenology*. **2013**, *200* (1), 24–34. <https://doi.org/10.2214/AJR.12.9543>.
- (109) Israelachvili, J. The Different Faces of Poly(Ethylene Glycol). *Proceedings of the National Academy of Sciences of the United States of America*. **1997**, *94* (16), 8378–8379.
- (110) Elmoazzen, H. Y.; Elliott, J. A. W.; McGann, L. E. Osmotic Transport across Cell Membranes in Nondilute Solutions: A New Nondilute Solute Transport Equation. *Biophysical Journal*. **2009**, *96* (7), 2559–2571. <https://doi.org/10.1016/j.bpj.2008.12.3929>.
- (111) Isaacks, R. E.; Bender, A. S.; Kim, C. Y.; Prieto, N. M.; Norenberg, M. D. Osmotic Regulation Of *myo*-Inositol Uptake in Primary Astrocyte Cultures. *Neurochemical Research*. **1994**, *19* (3), 331–338. <https://doi.org/10.1007/BF00971582>.
- (112) Wahajuddin; Arora, S. Superparamagnetic Iron Oxide Nanoparticles: Magnetic Nanoplatforms as Drug Carriers. *International Journal of Nanomedicine* **2012**, *7*, 3445–3471. <https://doi.org/10.2147/IJN.S30320>.
- (113) Di Marco, M.; Sadun, C.; Port, M.; Guilbert, I.; Couvreur, P.; Dubernet, C. Physicochemical Characterization of Ultrasmall Superparamagnetic Iron Oxide Particles (USPIO) for Biomedical Application as MRI Contrast Agents. *International Journal of Nanomedicine* **2007**, *2* (4), 609–622.
- (114) Corot, C.; Robert, P.; Idée, J.-M.; Port, M. Recent Advances in Iron Oxide Nanocrystal Technology for Medical Imaging. *Advanced Drug Delivery Reviews*. **2006**, *58* (14), 1471–1504. <https://doi.org/10.1016/j.addr.2006.09.013>.
- (115) Gupta, A. K.; Wells, S. Surface-Modified Superparamagnetic Nanoparticles for Drug Delivery: Preparation, Characterization, and

- Cytotoxicity Studies. *IEEE Transactions on NanoBioscience* **2004**, 3 (1), 66–73. <https://doi.org/10.1109/TNB.2003.820277>.
- (116) Klibanov, A. L.; Maruyama, K.; Torchilin, V. P.; Huang, L. Amphipathic Polyethyleneglycols Effectively Prolong the Circulation Time of Liposomes. *FEBS Letters*. **1990**, 268 (1), 235–237. [https://doi.org/10.1016/0014-5793\(90\)81016-H](https://doi.org/10.1016/0014-5793(90)81016-H).
- (117) Estephan, E.; Dao, J.; Saab, M.-B.; Panayotov, I.; Martin, M.; Larroque, C.; Gergely, C.; Cuisinier, F. J. G.; Levaillois, B. SVSVGMKPSRP: A Broad Range Adhesion Peptide. *Biomedizinische Technik. (Berlin)* **2012**, 57 (6), 481–489. <https://doi.org/10.1515/bmt-2011-0109>.
- (118) Sodek, J.; Ganss, B.; McKee, M. D. Osteopontin. *Critical Reviews in Oral Biology and Medicine*. **2000**, 11 (3), 279–303.
- (119) Choi, S. T.; Kim, J. H.; Kang, E.-J.; Lee, S.-W.; Park, M.-C.; Park, Y.-B.; Lee, S.-K. Osteopontin Might Be Involved in Bone Remodelling Rather than in Inflammation in Ankylosing Spondylitis. *Rheumatology*. **2008**, 47 (12), 1775–1779. <https://doi.org/10.1093/rheumatology/ken385>.
- (120) Wang, K. X.; Denhardt, D. T. Osteopontin: Role in Immune Regulation and Stress Responses. *Cytokine & Growth Factor Reviews*. **2008**, 19 (5–6), 333–345. <https://doi.org/10.1016/j.cytogfr.2008.08.001>.
- (121) Sakulkhu, U.; Mahmoudi, M.; Maurizi, L.; Salaklang, J.; Hofmann, H. Protein Corona Composition of Superparamagnetic Iron Oxide Nanoparticles with Various Physico-Chemical Properties and Coatings. *Scientific Reports*. **2014**, 4. <https://doi.org/10.1038/srep05020>.
- (122) Vogt, C.; Pernemalm, M.; Kohonen, P.; Laurent, S.; Hultenby, K.; Vahter, M.; Lehtiö, J.; Toprak, M. S.; Fadeel, B. Proteomics Analysis Reveals Distinct Corona Composition on Magnetic Nanoparticles with Different Surface Coatings: Implications for Interactions with Primary Human Macrophages. *PLoS ONE* **2015**, 10 (10). <https://doi.org/10.1371/journal.pone.0129008>.
- (123) Palchetti, S.; Colapicchioni, V.; Digiaco, L.; Caracciolo, G.; Pozzi, D.; Capriotti, A. L.; La Barbera, G.; Laganà, A. The Protein Corona of Circulating PEGylated Liposomes. *Biochimica et Biophysica Acta BBA - Biomembranes*. **2016**, 1858 (2), 189–196. <https://doi.org/10.1016/j.bbamem.2015.11.012>.
- (124) Li, H.; El-Dakdouki, M. H.; Zhu, D. C.; Abela, G. S.; Huang, X. Synthesis of  $\beta$ -Cyclodextrin Conjugated Superparamagnetic Iron Oxide

Nanoparticles for Selective Binding and Detection of Cholesterol Crystals. *Chemical Communications*. **2012**, *48* (28), 3385–3387.  
<https://doi.org/10.1039/C2CC17852D>.

- (125) Varan, G.; Öncül, S.; Ercan, A.; Benito, J. M.; Ortiz Mellet, C.; Bilensoy, E. Cholesterol-Targeted Anticancer and Apoptotic Effects of Anionic and Polycationic Amphiphilic Cyclodextrin Nanoparticles. *Journal of Pharmaceutical Sciences*. **2016**, *105* (10), 3172–3182.  
<https://doi.org/10.1016/j.xphs.2016.06.021>.
- (126) Yoffe, S.; Leshuk, T.; Everett, P.; Gu, F. Superparamagnetic Iron Oxide Nanoparticles (SPIONs): Synthesis and Surface Modification Techniques for Use with MRI and Other Biomedical Applications. *Current Pharmaceutical Design*. **2013**, *19* (3), 493–509.
- (127) Wang, Y.-X. J. Superparamagnetic Iron Oxide Based MRI Contrast Agents: Current Status of Clinical Application. *Quantitative Imaging in Medicine and Surgery*. **2011**, *1* (1), 35–40.  
<https://doi.org/10.3978/j.issn.2223-4292.2011.08.03>.
- (128) Wang, Y.-X. J.; Hussain, S. M.; Krestin, G. P. Superparamagnetic Iron Oxide Contrast Agents: Physicochemical Characteristics and Applications in MR Imaging. *European Radiology*. **2001**, *11* (11), 2319–2331.  
<https://doi.org/10.1007/s003300100908>.
- (129) Gossuin, Y.; Gillis, P.; Hocq, A.; Vuong, Q. L.; Roch, A. Magnetic Resonance Relaxation Properties of Superparamagnetic Particles. *Wiley Interdisciplinary Reviews. Nanomedicine and Nanobiotechnology*. **2009**, *1* (3), 299–310. <https://doi.org/10.1002/wnan.36>.
- (130) Stephen, Z. R.; Kievit, F. M.; Zhang, M. Magnetite Nanoparticles for Medical MR Imaging. *Materials Today (Kidlington England)*. **2011**, *14* (7–8), 330–338. [https://doi.org/10.1016/S1369-7021\(11\)70163-8](https://doi.org/10.1016/S1369-7021(11)70163-8).
- (131) Jun, Y.-W.; Huh, Y.-M.; Choi, J.-S.; Lee, J.-H.; Song, H.-T.; Kim, S.; Yoon, S.; Kim, K.-S.; Shin, J.-S.; Suh, J.-S.; et al. Nanoscale Size Effect of Magnetic Nanocrystals and Their Utilization for Cancer Diagnosis via Magnetic Resonance Imaging. *Journal of the American Chemical Society*. **2005**, *127* (16), 5732–5733. <https://doi.org/10.1021/ja0422155>.
- (132) Jun, Y.-W.; Seo, J.-W.; Cheon, J. Nanoscaling Laws of Magnetic Nanoparticles and Their Applicabilities in Biomedical Sciences. *Accounts of Chemical Research*. **2008**, *41* (2), 179–189.  
<https://doi.org/10.1021/ar700121f>.

- (133) Lee, J.-H.; Huh, Y.-M.; Jun, Y.; Seo, J.; Jang, J.; Song, H.-T.; Kim, S.; Cho, E.-J.; Yoon, H.-G.; Suh, J.-S.; et al. Artificially Engineered Magnetic Nanoparticles for Ultra-Sensitive Molecular Imaging. *Nature Medicine*. **2007**, *13* (1), 95–99. <https://doi.org/10.1038/nm1467>.
- (134) Tromsdorf, U. I.; Bigall, N. C.; Kaul, M. G.; Bruns, O. T.; Nikolic, M. S.; Mollwitz, B.; Sperling, R. A.; Reimer, R.; Hohenberg, H.; Parak, W. J.; et al. Size and Surface Effects on the MRI Relaxivity of Manganese Ferrite Nanoparticle Contrast Agents. *Nano Letters*. **2007**, *7* (8), 2422–2427. <https://doi.org/10.1021/nl071099b>.
- (135) Tong, S.; Hou, S.; Zheng, Z.; Zhou, J.; Bao, G. Coating Optimization of Superparamagnetic Iron Oxide Nanoparticles for High T2 Relaxivity. *Nano Letters*. **2010**, *10* (11), 4607–4613. <https://doi.org/10.1021/nl102623x>.
- (136) Reynolds, F.; O'loughlin, T.; Weissleder, R.; Josephson, L. Method of Determining Nanoparticle Core Weight. *Analytical Chemistry*. **2005**, *77* (3), 814–817. <https://doi.org/10.1021/ac049307x>.
- (137) Kim, B. H.; Lee, N.; Kim, H.; An, K.; Park, Y. I.; Choi, Y.; Shin, K.; Lee, Y.; Kwon, S. G.; Na, H. B.; et al. Large-Scale Synthesis of Uniform and Extremely Small-Sized Iron Oxide Nanoparticles for High-Resolution T1 Magnetic Resonance Imaging Contrast Agents. *Journal of the American Chemical Society*. **2011**, *133* (32), 12624–12631. <https://doi.org/10.1021/ja203340u>.
- (138) Szydowski, J.; Van Hook, W. A. Concentration and Temperature Dependence of Dynamic Light Scattering for Some Polystyrene Solutions in Toluene, Cyclohexane, Methylcyclohexane and Deuteromethylcyclohexane. *Macromolecules* **1998**, *31* (10), 3266–3274. <https://doi.org/10.1021/ma971777o>.
- (139) Mitsouras, D.; Mulkern, R. V.; Maier, S. E. Multi-Component T2 Relaxation Studies of the Avian Egg. *Magnetic Resonance in Medicine*. **2016**, *75* (5), 2156–2164. <https://doi.org/10.1002/mrm.25762>.
- (140) Mitsouras, D.; Vemula, P. K.; Yu, P.; Tao, M.; Nguyen, B. T.; Campagna, C. M.; Karp, J. M.; Mulkern, R. V.; Ozaki, C. K.; Rybicki, F. J. Immobilized Contrast Enhanced (ICE) MRI: Gadolinium-Based Long-Term MR Contrast Enhancement of the Vein Graft Vessel Wall. *Magnetic Resonance in Medicine*. **2011**, *65* (1), 176–183. <https://doi.org/10.1002/mrm.22606>.
- (141) Mitsouras, D.; Mulkern, R. V.; Rybicki, F. J. Strategies for Inner Volume 3D Fast Spin Echo Magnetic Resonance Imaging Using Nonselective

- Refocusing Radio Frequency Pulses). *Medical Physics*. **2006**, 33 (1), 173–186. <https://doi.org/10.1118/1.2148331>.
- (142) Mitsouras, D.; Lee, T. C.; Liacouras, P.; Ionita, C. N.; Pietilla, T.; Maier, S. E.; Mulkern, R. V. Three-Dimensional Printing of MRI-Visible Phantoms and MR Image-Guided Therapy Simulation., 3D Printing of MRI-Visible Phantoms and MR Image-Guided Therapy Simulation. *Magnetic Resonance in Medicine*. **2017**, 77, 77 (2, 2), 613, 613–622. <https://doi.org/10.1002/mrm.26136>, [10.1002/mrm.26136](https://doi.org/10.1002/mrm.26136).
- (143) Mulkern, R.; Haker, S.; Mamata, H.; Lee, E.; Mitsouras, D.; Oshio, K.; Balasubramanian, M.; Hatabu, H. Lung Parenchymal Signal Intensity in MRI: A Technical Review with Educational Aspirations Regarding Reversible Versus Irreversible Transverse Relaxation Effects in Common Pulse Sequences. *Concepts in Magnetic Resonance. Part A, Bridging Education and Research*. **2014**, 43A (2), 29–53. <https://doi.org/10.1002/cmr.a.21297>.
- (144) Poon, C. S.; Henkelman, R. M. Practical T2 Quantitation for Clinical Applications. *Journal of Magnetic Resonance Imaging*. **1992**, 2 (5), 541–553. <https://doi.org/10.1002/jmri.1880020512>.
- (145) Wahajuddin; Arora, S. Superparamagnetic Iron Oxide Nanoparticles: Magnetic Nanoplatfoms as Drug Carriers. *International Journal of Nanomedicine* **2012**, 7, 3445–3471. <https://doi.org/10.2147/IJN.S30320>.
- (146) Nap, R. J.; Park, S. H.; Szleifer, I. On the Stability of Nanoparticles Coated with Polyelectrolytes in High Salinity Solutions. *Journal of Polymer Science. Part B, Polymer Physics*. **52** (24), 1689–1699. <https://doi.org/10.1002/polb.23613>.
- (147) Bhattacharjee, S. DLS and Zeta Potential – What They Are and What They Are Not? *Journal of Controlled Release* **2016**, 235, 337–351. <https://doi.org/10.1016/j.jconrel.2016.06.017>.
- (148) Kouchakzadeh, H.; Shojaosadati, S. A.; Maghsoudi, A.; Farahani, E. V. Optimization of PEGylation Conditions for BSA Nanoparticles Using Response Surface Methodology. *AAPS PharmSciTech* **2010**, 11 (3), 1206–1211. <https://doi.org/10.1208/s12249-010-9487-8>.
- (149) Wei, H.; Bruns, O. T.; Kaul, M. G.; Hansen, E. C.; Barch, M.; Wiśniowska, A.; Chen, O.; Chen, Y.; Li, N.; Okada, S.; et al. Exceedingly Small Iron Oxide Nanoparticles as Positive MRI Contrast Agents. *Proceedings of the National Academy of Sciences of the United States of America*. **2017**, 201620145. <https://doi.org/10.1073/pnas.1620145114>.

- (150) Bates, D.; Abraham, S.; Campbell, M.; Zehbe, I.; Curiel, L. Development and Characterization of an Antibody-Labeled Super-Paramagnetic Iron Oxide Contrast Agent Targeting Prostate Cancer Cells for Magnetic Resonance Imaging. *PLoS ONE* **2014**, *9* (5), e97220. <https://doi.org/10.1371/journal.pone.0097220>.
- (151) Al Faraj, A.; Shaik, A. S.; Afzal, S.; Al-Muhsen, S.; Halwani, R. Specific Targeting and Noninvasive Magnetic Resonance Imaging of an Asthma Biomarker in the Lung Using Polyethylene Glycol Functionalized Magnetic Nanocarriers. *Contrast Media & Molecular Imaging* **2016**, *11* (3), 172–183. <https://doi.org/10.1002/cmml.1678>.
- (152) Al Faraj, A.; Shaik, A. S.; Afzal, S.; Al Sayed, B.; Halwani, R. MR Imaging and Targeting of a Specific Alveolar Macrophage Subpopulation in LPS-Induced COPD Animal Model Using Antibody-Conjugated Magnetic Nanoparticles. *International Journal of Nanomedicine* **2014**, *9*, 1491–1503. <https://doi.org/10.2147/IJN.S59394>.
- (153) Sillerud, L. O.; Solberg, N. O.; Chamberlain, R.; Orlando, R. A.; Heidrich, J. E.; Brown, D. C.; Brady, C. I.; Vander Jagt, T. A.; Garwood, M.; Vander Jagt, D. L. SPION-Enhanced Magnetic Resonance Imaging of Alzheimer's Disease Plaques in A $\beta$ PP/PS-1 Transgenic Mouse Brain. *Journal of Alzheimer's Disease: JAD* **2013**, *34* (2), 349–365. <https://doi.org/10.3233/JAD-121171>.
- (154) Ozdemir, A.; Ekiz, M. S.; Dilli, A.; Guler, M. O.; Tekinay, A. B. Amphiphilic Peptide Coated Superparamagnetic Iron Oxide Nanoparticles for in Vivo MR Tumor Imaging. *RSC Advances*. **2016**, *6* (51), 45135–45146. <https://doi.org/10.1039/C6RA07380H>.
- (155) Sawant, R. M.; Sawant, R. R.; Gultepe, E.; Nagesha, D.; Papahadjopoulos-Sternberg, B.; Sridhar, S.; Torchilin, V. P. Nanosized Cancer Cell-Targeted Polymeric Immunomicelles Loaded with Superparamagnetic Iron Oxide Nanoparticles. *Journal of Nanoparticle Research*. **2009**, *11* (7), 1777. <https://doi.org/10.1007/s11051-009-9611-4>.
- (156) Zhong, Y.; Dai, F.; Deng, H.; Du, M.; Zhang, X.; Liu, Q.; Zhang, X. A Rheumatoid Arthritis Magnetic Resonance Imaging Contrast Agent Based on Folic Acid Conjugated PEG- b -PAA@SPION. *Journal of Materials Chemistry. B* **2014**, *2* (19), 2938–2946. <https://doi.org/10.1039/C4TB00085D>.
- (157) Hussain, S. M.; Hess, K. L.; Gearhart, J. M.; Geiss, K. T.; Schlager, J. J. In Vitro Toxicity of Nanoparticles in BRL 3A Rat Liver Cells. *Toxicology In Vitro* **2005**, *19* (7), 975–983. <https://doi.org/10.1016/j.tiv.2005.06.034>.

- (158) Kim, J. S.; Yoon, T.-J.; Yu, K. N.; Kim, B. G.; Park, S. J.; Kim, H. W.; Lee, K. H.; Park, S. B.; Lee, J.-K.; Cho, M. H. Toxicity and Tissue Distribution of Magnetic Nanoparticles in Mice. *Toxicological Sciences*. **2006**, *89* (1), 338–347. <https://doi.org/10.1093/toxsci/kfj027>.
- (159) Karlsson, H. L.; Gustafsson, J.; Cronholm, P.; Möller, L. Size-Dependent Toxicity of Metal Oxide Particles—A Comparison between Nano- and Micrometer Size. *Toxicology Letters*. **2009**, *188* (2), 112–118. <https://doi.org/10.1016/j.toxlet.2009.03.014>.
- (160) Landmark, K. J. Dendrimer-Coated Iron Oxide Nanoparticles as Targeted MRI Contrast Agents. Unpublished doctoral dissertation – University of Michigan 2008. [https://deepblue.lib.umich.edu/bitstream/handle/2027.42/60801/landmark\\_1.pdf](https://deepblue.lib.umich.edu/bitstream/handle/2027.42/60801/landmark_1.pdf)
- (161) Anzai, Y.; Piccoli, C. W.; Outwater, E. K.; Stanford, W.; Bluemke, D. A.; Nurenberg, P.; Saini, S.; Maravilla, K. R.; Feldman, D. E.; Schmiedl, U. P.; et al. Evaluation of Neck and Body Metastases to Nodes with Ferumoxtran 10—Enhanced MR Imaging: Phase III Safety and Efficacy Study. *Radiology* **2003**, *228* (3), 777–788. <https://doi.org/10.1148/radiol.2283020872>.
- (162) Thoeny, H. C.; Triantafyllou, M.; Birkhaeuser, F. D.; Froehlich, J. M.; Tshering, D. W.; Binser, T.; Fleischmann, A.; Vermathen, P.; Studer, U. E. Combined Ultrasmall Superparamagnetic Particles of Iron Oxide—Enhanced and Diffusion-Weighted Magnetic Resonance Imaging Reliably Detect Pelvic Lymph Node Metastases in Normal-Sized Nodes of Bladder and Prostate Cancer Patients. *European Urology*. **2009**, *55* (4), 761–769. <https://doi.org/10.1016/j.eururo.2008.12.034>.
- (163) Varna, M.; Ratajczak, P.; Ferreira, I.; Leboeuf, C.; Bousquet, G.; Janin, A. *In Vivo* Distribution of Inorganic Nanoparticles in Preclinical Models. *Journal of Biomaterials and Nanobiotechnology*. **2012**, *3* (2A), 269–279. <https://doi.org/10.4236/jbnnb.2012.322033>.
- (164) Lind, K.; Kresse, M.; Debus, N. P.; Müller, R. H. A Novel Formulation for Superparamagnetic Iron Oxide (SPIO) Particles Enhancing MR Lymphography: Comparison of Physicochemical Properties and The *In Vivo* Behaviour. *Journal of Drug Targeting*. **2002**, *10* (3), 221–230. <https://doi.org/10.1080/10611860290022651>.
- (165) Singh, N.; Jenkins, G. J. S.; Asadi, R.; Doak, S. H. Potential Toxicity of Superparamagnetic Iron Oxide Nanoparticles (SPION). *Nano Reviews*. **2010**, *1* (1), 5358. <https://doi.org/10.3402/nano.v1i0.5358>.

- (166) Caetano-Lopes, J.; Canhão, H.; Fonseca, J. E. Osteoblasts and Bone Formation. *Acta Reumatológica Portuguesa*. **2007**, 32 (2), 103–110.
- (167) Izquierdo-Gómez, M. M.; Hernández-Betancor, I.; García-Niebla, J.; Marí-López, B.; Laynez-Cerdeña, I.; Lacalzada-Almeida, J. Valve Calcification in Aortic Stenosis: Etiology and Diagnostic Imaging Techniques. *BioMed Research International*. **2017**, 2017, 5178631. <https://www.hindawi.com/journals/bmri/2017/5178631/> (accessed Jul 27, 2018). <https://doi.org/10.1155/2017/5178631>.
- (168) Kim, Y.; Lobatto, M. E.; Kawahara, T.; Chung, B. L.; Mieszawska, A. J.; Sanchez-Gaytan, B. L.; Fay, F.; Senders, M. L.; Calcagno, C.; Becraft, J.; et al. Probing Nanoparticle Translocation across the Permeable Endothelium in Experimental Atherosclerosis. *Proceedings of the National Academy of Sciences of the United States of America*. **2014**, 111 (3), 1078–1083. <https://doi.org/10.1073/pnas.1322725111>.
- (169) Hinton, R. B.; Alfieri, C. M.; Witt, S. A.; Glascock, B. J.; Khoury, P. R.; Benson, D. W.; Yutzey, K. E. Mouse Heart Valve Structure and Function: Echocardiographic and Morphometric Analyses from the Fetus through the Aged Adult. *American Journal of Physiology. Heart and Circulatory Physiology*. **2008**, 294 (6), H2480–H2488. <https://doi.org/10.1152/ajpheart.91431.2007>.
- (170) Sider, K. L.; Blaser, M. C.; Simmons, C. A. Animal Models of Calcific Aortic Valve Disease. *International Journal of Inflammation*. **2011**, 2011, 364310. <https://www.hindawi.com/journals/iji/2011/364310/> (accessed Oct 6, 2017). <https://doi.org/10.4061/2011/364310>.
- (171) Drolet, M.-C.; Arsenault, M.; Couet, J. Experimental Aortic Valve Stenosis in Rabbits. *Journal of the American College of Cardiology*. **2003**, 41 (7), 1211–1217.
- (172) Naghavi, M.; John, R.; Naguib, S.; Siadaty, M. S.; Grasu, R.; Kurian, K. C.; van Winkle, W. B.; Soller, B.; Litovsky, S.; Madjid, M.; et al. PH Heterogeneity of Human and Rabbit Atherosclerotic Plaques; a New Insight into Detection of Vulnerable Plaque. *Atherosclerosis* **2002**, 164 (1), 27–35.
- (173) Rajamannan, N. M.; Subramaniam, M.; Springett, M.; Sebo, T. C.; Niekrasz, M.; McConnell, J. P.; Singh, R. J.; Stone, N. J.; Bonow, R. O.; Spelsberg, T. C. Atorvastatin Inhibits Hypercholesterolemia-Induced Cellular Proliferation and Bone Matrix Production in the Rabbit Aortic Valve. *Circulation* **2002**, 105 (22), 2660–2665.

- (174) Turk, J. R.; Laughlin, M. H. Physical Activity and Atherosclerosis: Which Animal Model? *Canadian Journal of Applied Physiology / Revue Canadienne de Physiologie Appliquée*. **2004**, *29* (5), 657–683.
- (175) Brousseau, M. E.; Hoeg, J. M. Transgenic Rabbits as Models for Atherosclerosis Research. *Journal of Lipid Research*. **1999**, *40* (3), 365–375.
- (176) Reid, R. Von Kossa's Method - Calcium. 4.
- (177) Deparaffinization protocol  
<http://www.histosearch.com/histonet/Mar99/Deparaffinizationprotocol.html>  
 (accessed Sep 19, 2018).
- (178) Caravan, P.; Farrar, C. T.; Frullano, L.; Uppal, R. Influence of Molecular Parameters and Increasing Magnetic Field Strength on Relaxivity of Gadolinium- and Manganese-Based T1 Contrast Agents. *Contrast Media & Molecular Imaging* **2009**, *4* (2), 89–100.  
<https://doi.org/10.1002/cmml.267>.
- (179) Francia, V.; Aliyandi, A.; Salvati, A. Effect of the Development of a Cell Barrier on Nanoparticle Uptake in Endothelial Cells. *Nanoscale* **2018**, *10* (35), 16645–16656. <https://doi.org/10.1039/C8NR03171A>.
- (180) Patkar, C.; Giaya, K.; Libraty, D. H. Dengue Virus Type 2 Modulates Endothelial Barrier Function through CD73. *American Journal of Tropical Medicine and Hygiene*. **2013**, *88* (1), 89–94.  
<https://doi.org/10.4269/ajtmh.2012.12-0474>.
- (181) Minami, H.; Tashiro, K.; Okada, A.; Hirata, N.; Yamaguchi, T.; Takayama, K.; Mizuguchi, H.; Kawabata, K. Generation of Brain Microvascular Endothelial-Like Cells from Human Induced Pluripotent Stem Cells by Co-Culture with C6 Glioma Cells. *PLoS One* **2015**, *10* (6), e0128890.  
<https://doi.org/10.1371/journal.pone.0128890>.
- (182) Gupta, A. K.; Gupta, M. Cytotoxicity Suppression and Cellular Uptake Enhancement of Surface Modified Magnetic Nanoparticles. *Biomaterials* **2005**, *26* (13), 1565–1573.  
<https://doi.org/10.1016/j.biomaterials.2004.05.022>.
- (183) Karwad, M. A.; Couch, D. G.; Theophilidou, E.; Sarmad, S.; Barrett, D. A.; Larvin, M.; Wright, K. L.; Lund, J. N.; O'Sullivan, S. E. The Role of CB1 in Intestinal Permeability and Inflammation. *FASEB Journal*. **2017**, *31* (8), 3267–3277. <https://doi.org/10.1096/fj.201601346R>.

- (184) Maherally, Z.; Fillmore, H. L.; Tan, S. L.; Tan, S. F.; Jassam, S. A.; Quack, F. I.; Hatherell, K. E.; Pilkington, G. J. Real-Time Acquisition of Transendothelial Electrical Resistance in an All-Human, in Vitro, 3-Dimensional, Blood-Brain Barrier Model Exemplifies Tight-Junction Integrity. *FASEB Journal*. **2018**, *32* (1), 168–182. <https://doi.org/10.1096/fj.201700162R>.
- (185) Cantril, C. A.; Skinner, R. A.; Rothwell, N. J.; Penny, J. I. An immortalised astrocyte cell line maintains the in vivo phenotype of a primary porcine in vitro blood–brain barrier model. *Brain Research*. **2012**, *1479*, 17–30.
- (186) Sedgwick, J. B.; Menon, I.; Gern, J. E.; Busse, W. W. Effects of Inflammatory Cytokines on the Permeability of Human Lung Microvascular Endothelial Cell Monolayers and Differential Eosinophil Transmigration. *Journal of Allergy and Clinical Immunology*. **2002**, *110* (5), 752–756.
- (187) Inflammation • MatTek Corporation  
<https://www.mattek.com/application/inflammation-2/> (accessed Feb 18, 2019).
- (188) Lundqvist, M.; Augustsson, C.; Lilja, M.; Lundkvist, K.; Dahlbäck, B.; Linse, S.; Cedervall, T. The Nanoparticle Protein Corona Formed in Human Blood or Human Blood Fractions. *PLoS ONE* **2017**, *12* (4), e0175871. <https://doi.org/10.1371/journal.pone.0175871>.
- (189) Weis, S.; Cui, J.; Barnes, L.; Cheresh, D. Endothelial Barrier Disruption by VEGF-Mediated Src Activity Potentiates Tumor Cell Extravasation and Metastasis. *Journal of Cell Biology*. **2004**, *167* (2), 223–229. <https://doi.org/10.1083/jcb.200408130>.
- (190) Bernhard, D.; Pfister, G.; Huck, C. W.; Kind, M.; Salvenmoser, W.; Bonn, G. K.; Wick, G. Disruption of Vascular Endothelial Homeostasis by Tobacco Smoke: Impact on Atherosclerosis. *FASEB Journal*. **2003**, *17* (15), 2302–2304. <https://doi.org/10.1096/fj.03-0312fje>.
- (191) Cunningham, K. S.; Gotlieb, A. I. The Role of Shear Stress in the Pathogenesis of Atherosclerosis. *Laboratory Investigation*. **2005**, *85* (1), 9–23. <https://doi.org/10.1038/labinvest.3700215>.
- (192) LaConte, L. E. W.; Nitin, N.; Zurkiya, O.; Caruntu, D.; O'Connor, C. J.; Hu, X.; Bao, G. Coating Thickness of Magnetic Iron Oxide Nanoparticles Affects R2 Relaxivity. *Journal of Magnetic Resonance Imaging* **2007**, *26* (6), 1634–1641. <https://doi.org/10.1002/jmri.21194>.

- (193) Hu, F.; Jia, Q.; Li, Y.; Gao, M. Facile Synthesis of Ultrasmall PEGylated Iron Oxide Nanoparticles for Dual-Contrast T<sub>1</sub> - and T<sub>2</sub> -Weighted Magnetic Resonance Imaging. *Nanotechnology* **2011**, *22* (24), 245604. <https://doi.org/10.1088/0957-4484/22/24/245604>.
- (194) Gharagouzloo, C. A.; et al. Quantitative vascular neuroimaging of the rat brain using superparamagnetic nanoparticles: New insights on vascular organization and brain function. *NeuroImage*. **2017**, *163*, 24–33.
- (195) Bao, Y.; Sherwood, J. A.; Sun, Z. Magnetic Iron Oxide Nanoparticles as T<sub>1</sub> Contrast Agents for Magnetic Resonance Imaging. *Journal of Materials Chemistry. C* **2018**, *6* (6), 1280–1290. <https://doi.org/10.1039/C7TC05854C>.
- (196) Patil, R. M.; Thorat, N. D.; Shete, P. B.; Bedge, P. A.; Gavde, S.; Joshi, M. G.; Tofail, S. A. M.; Bohara, R. A. Comprehensive Cytotoxicity Studies of Superparamagnetic Iron Oxide Nanoparticles. *Biochemistry and Biophysics Reports*. **2018**, *13*, 63–72. <https://doi.org/10.1016/j.bbrep.2017.12.002>.
- (197) Doherty, T. M.; Asotra, K.; Fitzpatrick, L. A.; Qiao, J.-H.; Wilkin, D. J.; Detrano, R. C.; Dunstan, C. R.; Shah, P. K.; Rajavashisth, T. B. Calcification in Atherosclerosis: Bone Biology and Chronic Inflammation at the Arterial Crossroads. *Proceedings of the National Academy of Sciences of the United States of America*. **2003**, *100* (20), 11201–11206. <https://doi.org/10.1073/pnas.1932554100>.
- (198) Demer, L. L.; Watson, K. E.; Boström, K. Mechanism of Calcification in Atherosclerosis. *Trends in Cardiovascular Medicine*. **1994**, *4* (1), 45–49. [https://doi.org/10.1016/1050-1738\(94\)90025-6](https://doi.org/10.1016/1050-1738(94)90025-6).
- (199) Cucchiari, D.; Torregrosa, J.-V. Calciphylaxis in Patients with Chronic Kidney Disease: A Disease Which Is Still Bewildering and Potentially Fatal. *Nefrologia*. **2018**, *38* (6), 579–586. <https://doi.org/10.1016/j.nefro.2018.09.001>.
- (200) Jeong, H. S.; Dominguez, A. R. Calciphylaxis: Controversies in Pathogenesis, Diagnosis and Treatment. *American Journal of Medical Sciences*. **2016**, *351* (2), 217–227. <https://doi.org/10.1016/j.amjms.2015.11.015>.
- (201) Nigwekar, S. U.; Kroshinsky, D.; Nazarian, R. M.; Goverman, J.; Malhotra, R.; Jackson, V. A.; Kamdar, M. M.; Steele, D. J. R.; Thadhani, R. I. Calciphylaxis: Risk Factors, Diagnosis, and Treatment. *American Journal*

*of Kidney Diseases*. **2015**, 66 (1), 133–146.  
<https://doi.org/10.1053/j.ajkd.2015.01.034>.

(202) Alfrey, A. C. The Role of Abnormal Phosphorus Metabolism in the Progression of Chronic Kidney Disease and Metastatic Calcification. *Kidney International. Supplement*. **2004**, No. 90, S13-17.  
<https://doi.org/10.1111/j.1523-1755.2004.09003.x>.

(203) Paloian, N. J.; Giachelli, C. M. A Current Understanding of Vascular Calcification in CKD. *American Journal of Physiology. Renal Physiology*. **2014**, 307 (8), F891–F900. <https://doi.org/10.1152/ajprenal.00163.2014>.

## CURRICULUM VITAE

